SPARSE SIGNAL REPRESENTATION BASED ALGORITHMS WITH APPLICATION TO ULTRASONIC ARRAY IMAGING

by

Shahrokh Hamidi

A THESIS SUBMITTED IN PARTIAL FULFILLMENT OF THE
REQUIREMENT FOR THE DEGREE OF
DOCTOR OF PHILOSOPHY
in
ELECTRICAL AND COMPUTER ENGINEERING
FACULTY OF ENGINEERING AND APPLIED SCIENCE
UNIVERSITY OF ONTARIO INSTITUTE OF TECHNOLOGY
OSHAWA, ONTARIO, CANADA
JUNE 2016

Contents

List of Figures

List of Tables

Acronyms

DAS	delay and sum
MAP	maximum a posteriori
RVI	remote visual inspection
SNR	signal to noise ratio
RMS	root mean square
OCB	over complete matrix
ROI	region of interest
NDT	nondestructive testing
SAFT	synthetic aperture focusing technique
SAA	synthetic aperture array
TFM	total focusing method
SOS	second order statistics
FMC	full matrix capture
RMSE	root mean square error
MCMC	Markov chain Monte Carlo
HMC	Hybrid Markov chain
DOA	direction of arrival
MRA	mode relative amplitude

DL	diagonal loading
RIP	restricted isometry property
OGA	orthogonal greedy algorithm
MP	matching pursuit
LASSO	least absolute shrinkage and selection operator
FOCUSS	focal underdetermined system solver

Abstract

We address one- and two-layer ultrasonic array imaging. We use an array of transducers to inspect the internal structure of a given specimen. In the case of one-layer imaging we also address the problem of mode conversion. We propose a sparse signal representation based method for imaging solid materials in the presence of mode conversion phenomenon.

In the case of two-layer imaging we model the signal propagation effect using Huygens principle and Rayleigh-Sommerfeld diffraction formula. We then use this model to develop a sparse signal representation based imaging technique for a test sample immersed in water.

Moreover, we develop a new sparse Bayesian technique. In the model that we develop, the reflectivity coefficients of the desired reflectors are nonnegative real numbers and sparse in nature. Therefore, we use Weibull distribution function with two hyperparameters, namely the shape parameter and the scaling parameter, to model the prior distribution function of the reflectivity coefficients of the reflectors. As we show, the Weibull distribution, whose scale parameter obeys the inverse Gamma distribution, will enforce sparsity. We then propose a method for estimating the shape parameter of the Weibull distribution using Mellin transform.

Acknowledgements

I would like to express my sincere gratitude to my supervisor Prof. Shahram Shahbazpanahi for his help and his support of my PhD study. He introduced me to the topics of array imaging and enforcing sparsity. He also helped me to make my thesis and paper readable and provided me with full financial support during my PhD program. A special thanks to the members of the examining committee for their advises and their valuable comments.

I would also like to express my special appreciation and thanks to my family for their constant support during my life.

Chapter 1

Introduction

1.1 Overview

Non-destructive testing (NDT) refers to the techniques that are used to inspect the internal structures of a test sample without causing any damage. Common NDT methods include ultrasonic, magnetic-particle, liquid penetrant, radiographic, remote visual inspection (RVI), eddy-current testing, and low coherence interferometry. NDT is commonly used in forensic engineering, mechanical engineering, petroleum engineering, electrical engineering, civil engineering, systems engineering, aeronautical engineering, medicine, and art [2].

A widely used NDT technique is ultrasonic array imaging, where an array of transducers is used to obtain an image of the material under test.

At the beginning of the fifties the technician only knew radiography (x-ray or radioactive isotopes) to detect internal flaws as well as the methods for nondestructive testing of material surfaces, e.g. the dye penetrant and magnetic particle method. Further development of the ultrasonic techniques happened after the Second World War by Sokolovin 1935 and applied by Firestonein 1940. Consequently, instruments were available for ultrasonic testing of materials. Solid materials are good conductors

of sound waves and waves are reflected not only at the interfaces but also by internal defects and this is the main principle of ultrasonic imaging [3].

One of the main advantage of ultrasonic testing over other material analysis methods is that it can often be performed on-line. Through the use of a water bath or water stream as a coupling medium we can transmit high frequency sound waves into and out of moving materials without direct contact. Since sound waves penetrate through the test specimen, material properties are measured in bulk rather than just on the surface, which means that we can inspect the internal structure of the material. It is sometimes even possible, through the use of selective gating, to analyze just one layer of a multi-layer, multi-material fabrication [4].

In ultrasonic imaging an ultrasound is generated inside the test sample using an array of transducers that act both as transmitters and receivers. As soon as the wave faces a discontinuity such as a hole or a crack inside the test sample, due to impedance mismatch a fraction of the wave energy reflects back toward the array and is received by the transducers. Hence by measuring the round trip delay of the wave, one can measure the distance of the discontinuity from the array.

The frequencies used in ultrasonic imaging range from 20 KHz to 100 MHZ. However, the most common frequency range is 0.5 MHz to 20 MHz [4]. The sensitivity is defined as the ability of the ultrasound to detect a discontinuity. In order for a discontinuity to be detected the size of the discontinuity should be greater than the wavelength of the ultrasound. Therefore, higher sensitivity is achievable at higher frequencies. At higher frequencies, however, the penetration depth of the ultrasound reduces. Thus, there is a compromise between sensitivity and the penetration depth.

Ultrasonic arrays are increasingly being utilized in NDT as a means to inspect solid structures in different industries. These arrays offer more flexibility and superior performance compared to conventional monolithic probes [5]. Traditionally, ultrasonic arrays are used to emulate a monolithic transducer by deploying parallel transmis-

sion circuits which are designed to fire multiple transducers with programmable time delays. Choosing different delay laws, the array output can be focused on different regions of the test specimen and different types of image, such as plane or focused B-scans, can be obtained [6]. Typically, in NDT applications, the defect to be imaged, is time-invariant over the period of the test and it is logical to perform data analysis off-line. To this end, several post-processing techniques have been proposed in the literature which use the data (A-scans) from all combinations of transmit and receive transducers in the array. This approach, often referred to as full matrix capture (FMC), provides the largest possible set of independent data that can be obtained from the array to image target objects [7, 8].

During post-processing, the data in the FMC approach is used by an array imaging algorithm that assumes a linear acoustic model within the specimen. This means that a given beam is never physically generated in the test piece but synthesized by applying a DAS technique [9] to the full data set or a subset of it. For example, in the synthetic aperture focusing technique (SAFT) [10], the pulse-echo data from every array element is used and an image is generated based on the DAS approach. In the DAS approach, different time-of-flights from each transducer element to each point in the region of interest (ROI) are compensated and then a summation is performed on all the aligned observations to form the image at that point. The total focusing method (TFM) presented in [7, 11] follows the same principle as SAFT except that the TFM technique uses the data from every transmitter and receiver combination in the imaging process.

There are two different types of ultrasonic imaging approaches, namely contact test and immersion test. In a contact test, the array is in contact with test sample. In situations where the surface of the test sample is not smooth, contact test may not be possible. In such situations, one can conduct an immersion test, where the test sample and the transducer array are immersed in a liquid such as water.

In immersion test, the gap between the transducer array and the test sample is filled with water. The challenge in immersion test is the different velocities that wave experiences while it passes through different layers. Moreover, when the wave hits the surface of the test sample diffraction happens. Therefore, finding the array spatial signature is a challenging task.

Another issue that we address in this dissertation is the mode conversion phenomenon. In solids different types of ultrasonic waves can be generated. The longitudinal and transverse ultrasonic waves are commonly used in ultrasonic imaging. In longitudinal waves particle vibrations are in the direction of the propagation. In transverse waves, particle vibrations are perpendicular to the direction of the propagation. We can either use one of these waves or combine them to generate new waves. Surface waves for example can be generated as a result of combination of both longitudinal and transverse waves. Another example is plate waves that are produced in materials with a few wavelength thickness. The most well known plate waves, with both industrial and medical applications, is Lamb wave. Two common modes of Lamb waves are symmetrical and asymmetrical. Surface waves and Lamb waves, however, have their own limitations. Surface waves can penetrate one wavelength into the solid and in the case of Lamb waves the thickness of the solid should be only a few wavelength [12–14].

1.2 Motivation

In regards of mode conversion phenomenon we have been motivated by the following.

The common modes used in ultrasonic imaging are longitudinal and shear (transverse) modes, as well as surface (Rayleigh) waves and plate (Lamb) waves [4]. Surface waves can penetrate one wavelength into the solid and in the case of Lamb waves the thickness of the solid should be only a few wavelength. Therefore, for applications

that the purpose is to inspect the internal structure of a test sample with thickness more than a few wavelength, surface waves and Lamb waves can not be used. Instead we can use only one of the longitudinal or transverse modes.

Although using only one of longitudinal or transverse waves can solve the aforementioned problem, mode conversion can generate another unused mode. The mode conversion is a common phenomenon in ultrasound. In fact when ultrasonic wave hits an interface or a reflector, waves with different propagation speeds are produced. Due to the difference in their propagation speeds, these modes are received by the transducers with different delays. If these modes are not taken into account during the imaging process, they can degrade the quality of the final image considerably. As reported in [1], ignoring mode conversion phenomenon will result in artifacts in the resulting image that could result in false interpretation.

As we mentioned before one of the widely used algorithms for ultrasonic imaging is the traditional DAS beam-forming method [15]. The DAS beamformer is based on the time of flight of the wave reflected from each hypothetical reflector. Therefore, in the presence of mode conversion, the DAS beamformer yields spurious targets. The reason goes back to the difference in the propagation speed for different modes. Whenever the velocity of a specific mode is used, the DAS beamformer results in the correct location of the target based on that mode. However, spurious reflectors will appear in the image due to the presence of other modes [1]. The DAS beamformer is not capable of taking the effect of all different modes into account. In [16], the well-known Capon and MUSIC techniques have been modified such that they can be used in multi-modal propagation environments. Referred to as MC-Capon and MC-MUSIC techniques, these methods yield a higher resolution and lower sidelobe level[1] as compared to the DAS beamformer.

[1]The difference between the amplitude of the mainlobe and the first sidelobe which has the maximum amplitude among all the sidelobes, is called the sidelobe level and is typically expressed

The MC-MUSIC and MC-Capon methods are capable of taking the effect of all different modes into account, and therefore, find the locations of the reflectors with a high precision. These two techniques, however, suffer from all the shortcomings that the MUSIC technique [17–19] and the Capon filter bank approach [19,20] suffer from. These two approaches need high SNR to yield an acceptable result and fail in the case of correlated targets. Also, the MUSIC method and the Capon technique require the covariance matrix of the received data to be estimated and in order to estimate the array data covariance matrix, several different snapshots are needed. Also, the MUSIC approach is a signal subspace based technique and needs the knowledge of the dimension of the signal subspace which is the number of the reflectors [21]. The knowledge of this dimension may not be available or the subspace can occupy the whole observation space. To overcome these issues, we propose a sparse signal representation based technique which not only is able to take the effect of all modes into account but also does not suffer from the aforementioned shortcomings. Our method can be implemented for the case in which one transducer is used to illuminate the region of interest. Its sensitivity to SNR is less than that of the MC-MUSIC and MC-Capon approaches. Furthermore, unlike the MC-MUSIC method, there is no need to know the number of reflectors. We further develop a sparse signal representation based approach for the case in which all the transducers are used to illuminate the region of interest. To the best of our knowledge, sparse signal recovery based technique has not been utilized for ultrasonic array imaging in the presence of mode conversion.

In ultrasonic array imaging, the knowledge of the array spatial signature for every point inside the region of interest (i.e., the vector of array response to a hypothetical source located at that point) is essential to the imaging process. This spatial signature depends on the geometry of the test setup and on properties of the environment

in dB.

through which the wave travels. In a homogenous medium, where the wave velocity is constant, modeling the array signature is rather straightforward. In non-homogenous media, where the wave velocity changes along the wave travel path, modeling the array spatial signature is not straightforward. One example of such non-homogenous media is immersion test. Indeed, the main challenge in immersion test is the different velocities that wave experiences while passing through different layers (here water and the specimen). Due to this difference in the wave velocities in the two layers, the wave does not follow a straight line, when entering from one medium to another one. In fact, when crossing the interface between two layers, the wave is subject to refraction, which hinders the task of modeling the array spatial signature.

One approach to account for the effect of different wave velocities is to use the so-called root mean square (RMS) velocity method which was first introduced and utilized in seismology [22]. This method was applied to multi-layer ultrasonic imaging in [15]. The idea of the RMS velocity technique relies on a ray theory based approximation of the length of the path traveled by the wave, in the presence of refraction, when it leaves from a hypothetical reflector and arrives at a transducer. This approximation however does not take into account that wave refraction occurs at infinitely many points on the interface between the two layers and not at one particular point on this interface. To overcome this issue, we herein use the Huygens principle to model the array spatial signature [23].

This model for the array spatial signature can then be used in any imaging technique such as DAS beam-forming method, MUSIC technique and Capon method. However, as we mentioned before all these techniques have their own disadvantages. Motivated by the aforementioned shortcomings we exploit the sparse property of our imaging problem and propose a sparse signal recovery based technique. We further address the superiority of this technique based on the result that we obtain from the experimental data.

In regards of using Bayesian inference to enforce sparsity we have been motivated by the following.

Sparse signal representation based techniques are either using an optimization problem, in which they minimize the ℓ_p-norm of the desired signal, or they rely on a Bayesian approach, where sparsity is enforced via introducing a prior function for the desired signal. In the former techniques the objective function is the ℓ_p-norm of the desired sparse signal. For $p = 1$, the ℓ_p-norm of the desired sparse signal becomes a convex function and hence we can use any software packages dedicated to solving convex optimization problem such as CVX software package [24] to solve the ℓ_p-norm minimization problem. The CVX software package casts the ℓ_1-norm minimization problem, as a linear programming problem for which solutions are available even for large scale problems [25]. However, the solution of the ℓ_1-norm minimization problem may not be the sparsest solution. In other words, when $p = 1$ we can easily find the global minimum for the ℓ_1-norm minimization problem, since it is a convex optimization problem. However, there is no guarantee that such a solution is also the sparsest one. Significant attention has been given to imposing conditions under which the global minimum for the ℓ_1-norm minimization problem yields the sparsest solution as well. However, these conditions are extremely restrictive and hard to impose in practical situations [26–30].

For $p < 1$ the ℓ_p-norm of the desired sparse signal becomes a non-convex function and the ℓ_p-norm minimization problem becomes combinatorial in nature and will be NP hard. Many approximations have been advised including greedy based techniques. Greedy based algorithms offer locally optimal solutions to ℓ_0-norm minimization problem [28]. The orthogonal greedy algorithm (OGA) is a heuristic approach to find the sparsest solution for ℓ_0-norm minimization problem [27, 31]. Known as forward stepwise regression, the OGA has been widely used in the setting of statistical modeling since 1960's [32]. In signal processing, the OGA is known as matching pur-

suit (MP) [33]. However, conditions under which the OGA yields the exact recovery are extremely restrictive [34].

Another way to overcome the difficulty with ℓ_p-norm for $0 \leq p < 1$, is to utilize the idea of sparse signal representation in the Bayesian framework. In the Bayesian approach, the troublesome ℓ_0-norm function is replaced with a distribution function [28]. In other words the sparsity of the signal is modeled using an appropriate distribution function which uses prior information about the desired sparse signal [28, 35–40].

Bayesian approaches can be divided into two categories: 1) maximum a posteriori (MAP) estimator using a fixed and computationally tractable prior and, 2) empirical Bayesian approaches that uses a flexible and parameterized prior that is learned from the data [28].

Among the first category we can mention Laplacian distribution where the MAP estimation problem using this prior is known as basis pursuit (BP) denoising [41] or least absolute shrinkage and selection operator (LASSO) [42]. The global minimum can be conveniently obtained, however, it sometimes fails to be the sparsest solution [26–30]. Another choice is Jeffreys distribution. The problem with Jeffreys prior is that Jeffreys-based cost function suffers from numerous local minima [28, 43]. Finally we can mention the generalized Gaussian prior for which the corresponding MAP optimization problem is called focal underdetermined system solver (FOCUSS) algorithm [28, 44]. The FOCUSS algorithm contains the Laplace and the Jeffreys prior as special cases [28].

There are serious problems with Bayesian estimation using the first category. In the case of Laplacian prior the optimization problem is a convex optimization problem which can easily be solved, however, the result may not be the sparsest solution. In the case of Jeffreys prior we are hindered by numerous local minima. The FOCUSS algorithm includes both Laplacian and Jeffreys prior as special cases. Therefore, we have the same problems with the FOCUSS algorithm as well.

Up to now, all the sparse signal recovery based techniques that we have mentioned rely on ℓ_p-norm, for $0 \leq p \leq 1$, of the desired signal to enforce sparsity. In the case of ℓ_1-norm the optimization problem is convex and the convergence to the global minima is guaranteed, however, conditions under which the global minimum for the ℓ_1-norm minimization problem to yield the sparsest solution are extremely restrictive and hard to impose in practical situations [26–30].

In regard with the Bayesian approaches based on the first category, as we discuss in the body of the paper, we should say that these techniques are also based on ℓ_p-norm of the desired signal. The MAP estimator for the Laplacian prior would reduce to the ℓ_1-norm minimization based approach. In the case of the FOCUSS algorithm for $0 \leq p < 1$ the problem is not convex and the convergence is not guaranteed. Therefore, we resort to the Bayesian methods based on the second category which from now on we address them by the sparse Bayesian learning based approaches. The sparse Bayesian learning based approaches do not rely on ℓ_p-norm of the desired signal to enforce sparsity. Instead in the sparse Bayesian learning the sparsity is enforced by assigning a parameterized prior, with unknown hyperparameters, to the desired signal. The unknown hyperparameters are estimated from the data [28, 37, 45].

1.3 Objective and Methodology

Part of our goal in this dissertation is to utilize the sparse signal representation based approach for ultrasonic imaging, in the presence of mode conversion phenomenon. We are assuming a contact ultrasonic test using an array of transducers which can transmit and receive ultrasonic waves. The aim is to obtain an image for a given material under test using the array measurements collected by all transducers corresponding to different transducers illuminating the region of interest. The transducers are fired in a round-robin fashion one after the other.

We first present a multi-modal model for the single snapshot case. Then we cast our problem of finding the reflectivity coefficients of the reflectors in the presence of mode conversion, as a sparse signal representation problem. We further extend the approach to the multiple snapshot case. As a result, the output of the algorithm will be more accurate, simply because by using all the measurement vectors we obtain higher SNR.

Furthermore, we apply block sparsity methodology to the multi-modal problem for the multiple snapshot case. This algorithm exploits block sparsity in the image by considering a range of possible modes for the wave.

We further manage to address the problem of multi-layer imaging. Based on Huygens principle we present a linear model for the array spatial signature. Assuming that the wave velocity in the ROI is perfectly known, we cast our imaging problem as a sparse signal recovery problem. To do so, we first consider the single snapshot case. We then address multi-layer imaging for the multiple snapshot case. Since sparse signal representation in the multiple snapshot case utilizes all the measurements, compared to the single snapshot case, a better performance is expected in the sense that the sidelobe level is lower and the accuracy in the estimation of the target location is significantly enhanced.

We then propose a sparse Bayesian learning based approach. We develop a high resolution method for imaging a test sample immersed in water. We use an array of ultrasonic transducers to detect any flaws or cracks inside a test object. Our goal is to find a maximum a posteriori (MAP) estimate of the reflectivity coefficients of the flaws inside the test sample.

In the model that we develop in this dissertation, the reflectivity coefficients of the desired reflectors are nonnegative real numbers and sparse in nature. Therefore, we use Weibull distribution [46] with two hyperparameters, namely the shape parameter and the scaling parameter, to model the prior distribution function of the reflectivity

coefficients of the reflectors. As we show, the Weibull distribution, whose scale parameter obeys the inverse Gamma distribution, will enforce sparsity. To the best of our knowledge this is the first time that Weibull distribution function is used to build a sparse model. By assigning inverse gamma distribution to the scaling parameter, we will convert Weibull distribution to a prior that enforces sparsity. We then propose a method for estimating the shape parameter of the Weibull distribution using Mellin transform [47].

The conditional posterior function, of the reflectivity coefficients of the reflectors inside the test sample, that we derive, is not among the well known distribution functions and finding its maximum (which represents the MAP estimator for the reflectivity coefficients of the reflectors) analytically is a hard task. To overcome this difficulty we manage to draw samples from this conditional posterior function and then calculate the mean of these samples. To accomplish this goal, we can use the well known sampling techniques in statistics such as Markov chain Monte Carlo (MCMC) and Gibbs sampler [48,49]. However, due to the curse of dimensionality the MCMC and Gibbs sampler are not appropriate choices for our work [48,49]. Instead, we use hybrid Markov chain (HMC). The HMC technique is a combination of the Hamiltonian Monte Carlo and the Metropolis-Hastings random walk [48–50]. After drawing samples from the conditional posterior function of the reflectivity coefficients of the reflectors inside the test sample we can find the maximum of this conditional posterior function which will be the MAP estimate of the reflectivity coefficients of the reflectors.

At the end we compare the performance of the proposed sparse Bayesian learning based approach with the well known sparse signal representation based techniques in the literature.

1.4 Summery of Contributions

Our contribution can be summarized as follows

1 - We address the problem of ultrasonic imaging of a test sample based on sparse signal representation techniques for both single and multiple snapshot scenarios while the effect of multi-mode is taken into account.

2 - We manage to apply sparse signal representation based techniques along with Huygens principle for imaging a two-layer material. We present the sparse signal recovery problem based on Bayesian inference and apply the proposed technique to the experimental data. We show that Bayesian inference based technique provides better performance compared to the sparse signal representation based techniques in the literature.

1.5 List of Publications

- S. Hamidi, and S. Shahbazpanahi, "Sparse Signal Recovery based Imaging in the Presence of Mode Conversion with Application to Non-Destructive Testing", *IEEE Transactions on Signal Processing*, vol. 64, no. 5, pp. 1352-1364, March 2016.

1.6 Outline of Dissertation

Focusing on the sparse signal representation based techniques we will inspect the internal structure of a test sample using an array of transducers. We address both the contact and immersed imaging. In the contact imaging we consider the imaging problem in the presence of mode conversion phenomenon. We further consider multi-layer imaging using sparse Bayesian learning based technique. Therefore, this study has been organized as follows.

Chapter 2 is a review of the works that have addressed ultrasonic imaging in the presence of mode conversion. We further review the works on ultrasonic imaging for multi-layer case. We also give a literature review related to the sparse signal representation based techniques.

In Chapter 3, we describe our model for ultrasonic imaging of a test sample in the presence of mode conversion. We then write the SOS based algorithms [16] based on our model. We develop a technique based on sparse signal representation to handle the problem of ultrasonic imaging in the presence of mode conversion for a contact setup. We describe the proposed algorithm for both the single and multiple snapshot scenarios. Finally we apply all the methods to the experimental data from a test solid illuminated by an array of transducers (contact setup) in the presence of mode conversion.

In Chapter 4, we develop a sparse signal representation based model for the two-layer imaging. We then mention previous algorithms used in the field of array imaging. Afterwards, we present our proposed algorithm which is based on Bayesian learning. At the end we apply all the techniques to the experimental data gathered from a test sample immersed in water and discuss the results.

Finally, we have dedicated Chapter 5 to conclusions and future work.

Chapter 2

Background and Literature Review

2.1 Ultrasonic Array Imaging

Previous results in array-based NDT mostly focus on applying the traditional DAS beamformer for imaging. However, the DAS-based approach is independent of the statistical properties of the data. This means that they are robust and their performance is predictable as it is data independent. However, they provide lower resolution and have inferior interference suppression capabilities, as compared to the high-resolution techniques such as the well-celebrated MUSIC technique [17] and the well-investigated Capon algorithm [51], [52]. Indeed, MUSIC and Capon techniques exploit the second order statistics (SOS) of the data. It is worth mentioning that the FMC approach has been used to estimate the sample covariance matrix in several earlier works including [52].

Recently [23] has successfully applied MUSIC and Capon based methods along with the traditional DAS beamformer to two-layer structure using the Huygens principle to model the array spatial signature. It has been shown in [23] that MUSIC and Capon based techniques outperform the DAS beamformer in lower sidelobe levels and higher resolution. In fact these techniques have been applied to the experimental

ultrasonic data gathered from a test specimen immersed in water.

In the case of sparse signals, sparse signal representation based techniques can be utilized. Sparse signal representation based techniques have found their applications in different fields, such as synthetic aperture radar imaging [53], image reconstruction and restoration [54], sparse antenna array design [55], and array processing application [56], to mention a few.

[21,57] are among the early sources that have addressed the better performance of sparse signal representation based techniques. In [21,57] the authors develop a sparse signal representation based technique for direction of arrival (DOA) estimation and compare the performance of the proposed algorithm to that of the MUSIC and Capon based methods as well as the traditional DAS beamformer. They have shown that sparse signal representation based techniques do not suffer from Rayleigh resolution limit, their sensitivity to SNR and correlated targets are lower than that of the Capon and MUSIC based methods, they can also be applied to nonlinear arrays, even with non-Gaussian measurement noises.

Another work, which has been done in the field of ultrasonic imaging, is [58]. The authors of [58] exploit sparsity for imaging human tissues. The variation of the wave propagation velocity in such a biomedical application, is not significant. Indeed, the authors of [58] use an average velocity for the wave, thereby treating the ROI, essentially, as a homogenous medium.

One of the important features of sparse signal representation based approaches is that they can generate a very reliable image even in the MIMO case. MUSIC and Capon based techniques use the covariance matrix of the received data. Therefore, they both need multiple snapshots to estimate the sample covariance matrix. Hence, compared to the MUSIC and the Capon methods, sparse signal representation based approaches provide a unique opportunity to obtain the image in applications where getting access to multiple measurements are either impossible or very hard. However,

in applications that multiple measurements are available, enormous works have been dedicated to exploit the information of the whole data set [21, 57, 59–62].

Sparse signal representation problem can also be describe using Bayesian inference. Among different studies conducted in this area, we can mention [63]. In [63], a technique based on Bayesian inference has been used for medical image restoration. One of the features that distinguishes our work from [63], is the fact that the problem studied in [63], is not target localization. It is the speckle noise that the investigation in [63] wants to remove. To put it differently, what [63] does, is image processing not signal processing which is our concern in this work.

In [64], a Bayesian method has been used in a homogeneous environment. A Bernoulli-Gaussian prior has been assigned to the Fourier transform of the ultrasound image to enforce sparsity. Then, by multiplying the received data by a random matrix, the authors of [64], reduce the dimension of the image, and consequently, compress the ultrasound image. Our work, however, is different from that of [64], as we deal with a non-homogeneous environment. Also, instead of Bernoulli-Gaussian model for the desired reflectivity coefficients, we use a Weibull model. Moreover, as we mentioned before, since we are dealing with high dimensional problem therefore, the Gibbs sampler is inefficient and instead we use the HMC technique.

2.2 Ultrasonic Array Imaging in the Presence of Mode Conversion

In regards of mode conversion, [1] is the first paper that develops an algorithm based on traditional DAS beamformer to tackle this issue. The authors in [1] clearly show the adverse effect of mode conversion. In fact they reveals that this phenomenon will create spurious reflectors in the final image.

In [16], they apply the MUSIC technique and the Capon method to NDT applica-

tions. These approaches have been successfully utilized in radar, sonar, and medical ultrasound applications, resulting in higher resolution and better sidelobe suppression capabilities, as compared to the standard DAS method. However, in NDT, there are a number of competing factors that need to be carefully balanced based on the challenges specific to this application. First, the standard MUSIC and Capon methods fail in highly correlated signals and this is one of the main reasons hindering the widespread use of these techniques in active array applications such as NDT. In [16], they interpret the full data matrix differently by using each column of this matrix as an independent snapshot for obtaining the sample estimate of the data covariance matrix required for the MUSIC and the Capon approaches. Using this approach, the rank of the covariance matrix is increased and the MUSIC method as well as the Capon approach can be applied for NDT applications.

Second, in addition to the desired signal reflections from the defect, array inspections result in a range of imaging artifacts due to combined effects of multiple reverberations, mode conversions, and noise which interfere with the signal of interest [65]. Considering the aforementioned challenges, only a handful approaches in NDT have applied adaptive beam-forming for the imaging algorithms. For example, the authors of [66] applied the minimum variance distortionless response (MVDR) principle to image plate structures using Lamb waves. To the best of our knowledge, [16] and [1] are the only works that have addressed the mode conversion phenomenon and multi-modal propagation effects.

In [16], They take a different approach and address the question of what can be gained if the SOS-based techniques, such as the MUSIC and the Capon methods, exploit the additional information existing in all modes to their advantage- a problem not previously addressed in the context of NDT applications. [16] exploits the dominant acoustic modes in the received data and propose two multi-modal methods based on the MUSIC and the Capon techniques (hereafter referred to as

MC-MUSIC and MC-Capon techniques) thereby taking mode conversion effects into account. [16] considers the scenario whereby waves transmitted by the array elements are assumed uni-modal but can act as multi-modal receivers. Although this scenario is non-physical, since such array elements would violate reciprocity, it is used for illustrative purposes to demonstrate the underlying principle. In the proposed imaging algorithms, the array steering vector depends not only on the location of a hypothetical reflector but also on the *mode relative amplitude* (MRA) coefficients of that reflector in the ROI.

In [16], the authors define these coefficients as mode-dependent parameters representing the ultrasonic reflectivity or the scattering strength at locations of the defects in all modes. Using the normalized mode-dependent steering vectors, [16] then uses the MUSIC and the Capon techniques to first estimate the MRA coefficients for each point in the ROI, and then, to obtain the signal scattering strength of different points in the ROI. The MUSIC algorithm relies on the notions of signal and noise subspaces. The signal subspace is defined as the subspace spanned by the principal eigenvectors of the data covariance matrix and the noise subspace is the complement of the signal subspace. The MUSIC approach requires the proper choice of the dimension of the signal subspace, and hence, in their MUSIC-based imaging techniques, this dimension is considered as a design parameter.

Capon-based imaging method is closely related to adaptive beam-forming: for any point in the ROI, this method aims to find the maximum power of the output of an adaptive beamformer while considering other points as interferers whose reflected signals should be attenuated at the output of the beamformer as much as possible. The Capon method is very sensitive to errors in the presumed (search) steering vector. In fact, even a slight mismatch between the search and the true steering vectors may cause an underestimation of the amplitude of the desired signal [67–71]. In practical implementation, some kind of regularization is needed and the most common method

is the so-called diagonal loading (DL) method [72]. Hence in [16], they apply the DL technique to the data covariance matrix to correct the effect of the mismatch between the true and the search steering vectors. Through numerical simulations, they show that the SOS-based approaches, such as MUSIC and Capon methods, outperform the DAS-based approaches in terms of RMSE and they also provide higher resolution and better sidelobe suppression capabilities. In addition, the modified MUSIC- and Capon-based imaging algorithms provide higher resolution images as compared to their standard mode-neglecting counterparts.

2.2.1 MC-MUSIC and MC-Capon

Suppose that we have an array of M elements which receives a narrow band signal at frequency ω_0 from L reflectors. The vector of array signal, $\mathbf{y}_{mc} \in \mathbb{C}^{M\times 1}$, received at the location of the M receivers can then be described as

$$\mathbf{y}_{mc} = \mathbf{A}_{mc}\boldsymbol{\rho} + \mathbf{w}_{mc} \tag{2.1}$$

where the vector $\boldsymbol{\rho} \in \mathbb{R}^{L\times 1}$ is the reflectivity coefficients of the reflectors, the vector $\mathbf{w}_{mc} \in \mathbb{C}^{M\times 1}$ is the noise vector and the l^{th} column of the matrix $\mathbf{A}_{mc} \in \mathbb{C}^{M\times L}$ is given as

$$\mathbf{a} = [e^{-jkd_{1l}}\ e^{-jkd_{2l}}\ \cdots\ e^{-jkd_{Ml}}]^T. \tag{2.2}$$

In (2.2), $k \triangleq \frac{\omega_0}{c}$ and c are the wavenumber and the propagation speed for the wave, respectively, d_{nl} is the Euclidean distance between the l^{th} reflector, and the n^{th} receiver.

The basic building block for both MUSIC and Capon approach is the covariance matrix of the array measurements. By collecting N different snapshots, the array covariance matrix can be estimated by its sample covariance matrix, which is defined

as

$$\hat{\mathbf{R}} \triangleq \frac{1}{N}\sum_{p=1}^{N}\mathbf{y}_{mc}\mathbf{y}_{mc}^{H} \tag{2.3}$$

where H stands for complex conjugate transpose and $\mathbf{y}_{mc}$ is given in (2.1). To present the final result for the MC-MUSIC and MC-Capon techniques, we first introduce the $M \times R$ matrix $\tilde{\mathbf{A}}(\mathbf{r})$ as

$$\tilde{\mathbf{A}}(\mathbf{r}) \triangleq [\mathbf{a}^{(1)}(\mathbf{r}) \;\; \mathbf{a}^{(2)}(\mathbf{r}) \;\; \cdots \;\; \mathbf{a}^{(R)}(\mathbf{r})] \tag{2.4}$$

where the r^{th} column, $\mathbf{a}^{(r)}(\mathbf{r})$, is the steering vector (or the response) of the array to a hypothetical reflector located at point $\mathbf{r}$ and mode r and is given as

$$\mathbf{a}^{(r)} = [e^{-jk_r d_{1l}} \; e^{-jk_r d_{2l}} \; \cdots \; e^{-jk_r d_{Ml}}]^T. \tag{2.5}$$

In (2.5), $k_r \triangleq \frac{\omega_0}{c_r}$ and c_r are the wavenumber and the propagation speed for the mode r, respectively. We now present the result of MC-MUSIC method as [16]

$$\mathcal{I}_{\text{MC-MUSIC}}(\mathbf{r}) = \lambda_{\max}\left\{\left(\tilde{\mathbf{A}}^H(\mathbf{r})\mathbf{E}_n\mathbf{E}_n^H\tilde{\mathbf{A}}(\mathbf{r})\right)^{-1}\tilde{\mathbf{A}}^H(\mathbf{r})\tilde{\mathbf{A}}(\mathbf{r})\right\} \tag{2.6}$$

where $\mathbf{E}_n$ is an $M \times (M - L_{\text{s}})$ matrix whose columns are the eigenvectors of the matrix $\hat{\mathbf{R}}$ corresponding to the smallest $M - L_{\text{s}}$ eigenvalues, with L_{s} being the dimension of the signal subspace and $\lambda_{\max}(\mathbf{B})$ stands for the largest eigenvalue of matrix $\mathbf{B}$. The locations of the scatterers can be estimated as those values of $\mathbf{r}$ for which $\mathcal{I}_{\text{MC-MUSIC}}(\mathbf{r})$ has its L highest peaks.

The result of MC-Capon is also described as

$$\mathcal{I}_{\text{MC-Capon}}(\mathbf{r}) = \lambda_{\max}\left\{\left(\bar{\mathbf{A}}^H(\mathbf{r})\mathbf{R}_{\text{DL}}^{-1}\bar{\mathbf{A}}(\mathbf{r})\right)^{-1}\tilde{\mathbf{A}}^H(\mathbf{r})\tilde{\mathbf{A}}(\mathbf{r})\right\} \tag{2.7}$$

where

$$\mathbf{R}_{\text{DL}} \triangleq \hat{\mathbf{R}} + \kappa\mathbf{I}, \tag{2.8}$$

is the so-called diagonally loaded sample covariance matrix and κ is the so-called diagonal loading factor and it is a tunable parameter to calibrate the resulting Capon image. Despite the good performance in the presence of mode conversion, the MC-MUSIC and MC-Capon methods, have their own shortcomings. Since they are based on MUSIC and Capon approaches, they suffer from the same shortcomings which hinder the MUSIC and Capon methods. They both need high SNR and fail in the case of correlated targets. To estimate the covariance matrix, both methods require a sufficient number of snapshots. However, in certain practical situations, it may not be possible or affordable to collect enough snapshots. To form the noise subspace used in the MUSIC method, the dimension of signal subspace, i.e., the number of scatterers should be known in advance. In NDT, signal enumeration is still an open problem. With respect to the Capon method, the sidelobe level is limited to σ^2/M, where σ^2 is the power of the noise.

2.3 Sparse Signal Representation Based Techniques

The application of sparsity and the techniques that can recover the desired information from a sparse signal goes back to 1990's, [41, 73, 74]. The existence of a mathematical basis for over-complete representation have been considered in [27, 75, 76]. In fact the basic idea comes from the following algebraic problem

$$\mathbf{y} = \mathbf{A}\mathbf{x} \tag{2.9}$$

where $\mathbf{y} \in \mathbb{C}^{n\times 1}$ and for $m > n$, the matrix $\mathbf{A} \in \mathbb{C}^{n\times m}$ is the over-complete matrix. The problem described in (2.9) is obviously an ill-posed problem. However, if we know that the vector $\mathbf{x} \in \mathbb{C}^{m\times 1}$ is sparse, a unique solution is achievable. More specifically, we can enforce sparsity via ℓ_0-norm of $\mathbf{x}$. The notation ℓ_0-norm was first used by D. Donoho, and is described as the number of nonzero elements of vector $\mathbf{x}$

which is also equal to the cardinality of $\mathbf{x}$. Hence the following optimization problem is offered to recover $\mathbf{x}$-norm from the ill-posed eqnarray given in (2.9):

$$\begin{aligned} \min_{\mathbf{x}} \quad & \|\mathbf{x}\|_0 \\ \text{subject to} \quad & \mathbf{y} = \mathbf{A}\mathbf{x}. \end{aligned} \tag{2.10}$$

2.3.1 Basis Pursuit

The difficulty with (2.10) is that the ℓ_0-norm is not a convex function and the optimization problem given in (2.10) is combinatorial in nature. To overcome this difficulty, it was proposed to replace ℓ_0-norm with ℓ_1-norm [77, 78]. Since ℓ_1-norm is a convex function, (2.10) can be easily solved. Hence the optimization problem given in (2.11) is modified as

$$\begin{aligned} \min_{\mathbf{x}} \quad & \|\mathbf{x}\|_1 \\ \text{subject to} \quad & \mathbf{y} = \mathbf{A}\mathbf{x}. \end{aligned} \tag{2.11}$$

The question that remains is whether the result of minimizing ℓ_1-norm is the sparsest solution for (2.9) or not. In general the answer is no. However under some restrictions on the nonzero elements of the desired signal and the structure of the matrix $\mathbf{A}$ the minimization of ℓ_1-norm will provide us with the sparsest solution [77,78]. In Fig. 2.1-(a)-(b) we have shown how (2.10) finds the sparsest solution when the ℓ_1-norm is used as an objective function. In Fig. 2.1-(a) the intersection point between $\mathbf{y} = \mathbf{A}\mathbf{x}$ and the x_1 axis is higher than c. Therefore, by increasing the ℓ_1-norm of the vector $\mathbf{x}$, both of the $\mathbf{y} = \mathbf{A}\mathbf{x}$ and $\|\mathbf{x}\|_1$ cross the x_1 axis at c'.

In fact for $p < 1$ the ℓ_p-norm is a better candidate for the objective function in (2.10), however, for $p < 1$ the ℓ_p-norm is a concave function. Fig. 2.1-(c) shows different values for p. As can be seen when $p = 2$ the outward curvature of the ℓ_p-norm hits the constraint function, i.e., $\mathbf{y} = \mathbf{A}\mathbf{x}$, at a point which is not the sparsest solution. Therefore, the best choice is the ℓ_1-norm.

In order for the result of (2.10) to be unique the matrix $\mathbf{A}$ should have a submatrix of rank greater than $2k$ where $\|\mathbf{x}\|_0 = k$ [79]. However, in practice the model given in (2.9) is modified as

$$\mathbf{y} = \mathbf{A}\mathbf{x} + \mathbf{w} \tag{2.12}$$

where $\mathbf{w} \in \mathbb{C}^{n\times 1}$ represents the noise of the model. For the model given in (2.12) the optimization problem presented in (2.11) is modified as

$$\begin{aligned} \min_{\mathbf{x}} \quad & \|\mathbf{x}\|_1 \\ \text{subject to} \quad & \|\mathbf{y} - \mathbf{A}\mathbf{x}\|_2 < \beta \end{aligned} \tag{2.13}$$

where β is the regularization parameter and is chosen such that the probability of the norm of the noise vector being larger than β is small [21,57]. The CVX software package casts (2.13), as a linear programming problem for which solutions are available even for large scale problems and the computational complexity is $O(m^3)$ [25].

The optimization problem given in (2.13) is called basis pursuit (BP) denoising [41].

For the optimization problem given in (2.13) not only the uniqueness of the result should be considered but we should also find the conditions under which the stability of the result is guaranteed as well. The stability of (2.13) is guaranteed, in a sense that the error is bounded in ℓ_1 or ℓ_2 norm, if $n = O(k \log m)$ [79].

To show that the sparse signal representation based methods yield the better resolution and lower sidelobe level compared to those of the DAS beamformer, the MUSIC method and the Capon technique, we have simulated a DOA estimation problem. An array with 64 elements and element pitch equal to half of the wavelength has been considered. The SNR is equal to 15 dB and 64 different snapshots have been generated. For the DAS beamformer, the MUSIC method, the Capon technique all the 64 snapshots have been used. For the ℓ_1-norm minimization based method,

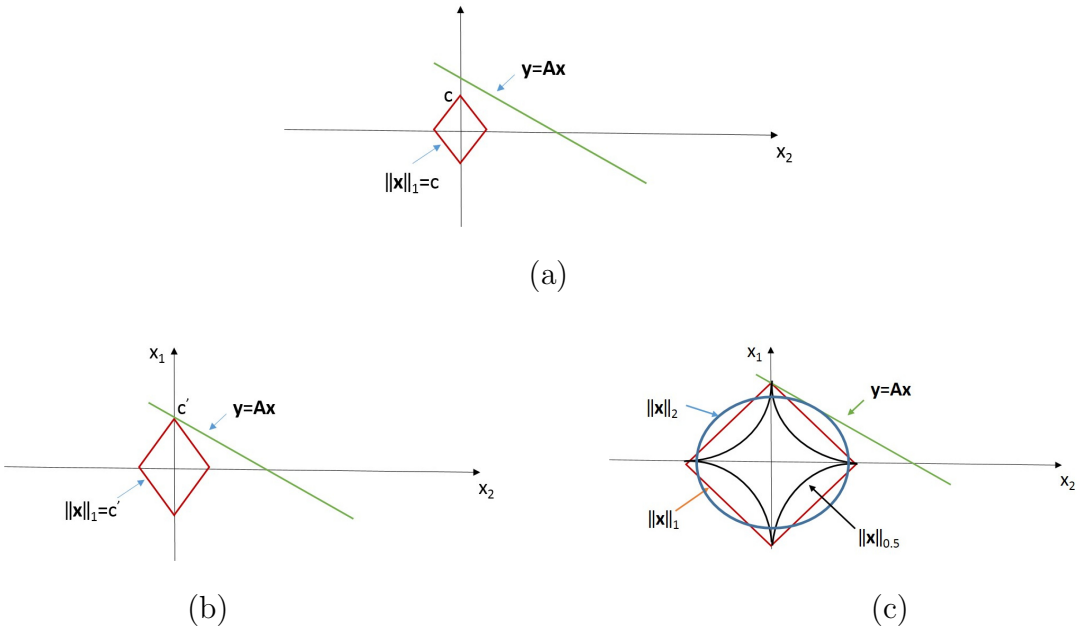

Figure 2.1: a) and b) show how (2.10) is solved when the objective function is chosen to be the ℓ_1-norm of the desired signal, c) shows the optimization problm given in (2.10) for different objective functions.

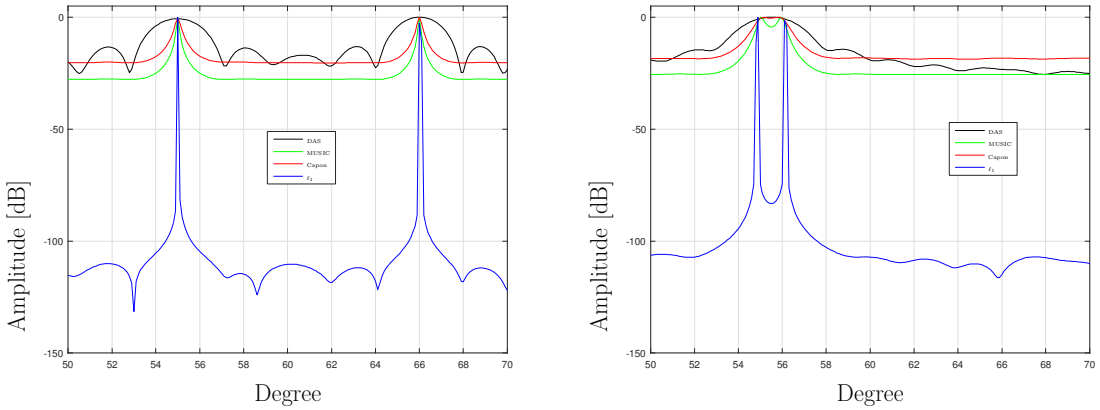

Figure 2.2: DOA estimation for two targets at a) 55 and 66 degree, b) 55 and 56 degree.

however, only one snapshot has been used. Fig. 2.2-(a) shows the result for two uncorrelated targets located at 55 and 66 degree. From Fig. 2.2-(a) we see the lower sidelobe levels of the ℓ_1-norm minimization based approach. Fig. 2.2-(b) shows the result for two uncorrelated targets located at 55 and 56 degree. From Fig. 2.2-(b) we see that the ℓ_1-norm minimization based approach also has much finer resolution than the DAS beamformer, the MUSIC method and the Capon technique.

2.3.2 Orthogonal Greedy Algorithm

The OGA is a heuristic approach to find the sparsest vector $\mathbf{x}$. In the OGA one solves the following optimization problem [27, 32]

$$i_k = \arg \max_{1 \leq i \leq N} | < \mathbf{r}^{(k-1)}, A^{(i)} > | \tag{2.14}$$

where $< \cdot, \cdot >$ stands for the inner product in Euclidean space and $A^{(i)}$ is the i^{th} column of the matrix $\mathbf{A}$. Moreover $\mathbf{r}^{(k)} = \mathbf{y} - \hat{\mathbf{y}}^{(k)}$ where $\hat{\mathbf{y}}^{(k)} = \sum_{i=1}^{k} \chi_{il}^{k} A_{il}$ in which the coefficients χ_{il}^{k} are fitted by least squares to minimize $\|\mathbf{y} - \hat{\mathbf{y}}^{(k)}\|_2$. The algorithm

stops when the ℓ_2-norm of error term falls below a predetermined threshold ξ_g, i.e., $\|\mathbf{y} - \hat{\mathbf{y}}^{(k)}\|_2 \leq \xi_g$. Known as forward stepwise regression, the OGA has been widely used in the setting of statistical modeling since 1960's [31]. In signal processing, the OGA is known as MP [33]. The algorithm (2.14) is in fact called orthogonal matching pursuit (OMP) [80, 81]. The computational complexity of OMP, given in (2.14), is $O(kmn)$ and the number of measurements should satisfy $n = O(k \log m)$ [80, 82, 83].

The mutual incoherence is defined as

$$\mu = \max_{\mathrm{i} \neq \mathrm{j}} \frac{| < \mathrm{A}^{(\mathrm{i})}, \mathrm{A}^{(\mathrm{j})} > |}{\|\mathrm{A}^{(\mathrm{i})}\|_2 \|\mathrm{A}^{(\mathrm{j})}\|_2}. \tag{2.15}$$

Suppose that $\|\mathbf{w}\|_2 \leq b_2$ and $\xi_g \leq b_2$ for a scalar b_2. Theorem 1 in [34] then guarantees that if $\mu < \frac{1}{2k-1}$ and if all the nonzero coefficients x_i satisfy $|x_i| \geq \frac{2b_2}{1-(2k-1)\mu}$, the OMP algorithm recovers exactly all the true reflectors.

2.3.3 Maximum A Posteriori Estimator

In this subsection, we review the methods for sparse signal recovery techniques based on MAP estimator that uses a fixed and computationally tractable prior.

Laplacian Prior In this method, a Laplacian distribution is assigned to the vector $\mathbf{x}$ which is described as [84]

$$p(\mathbf{x}) \propto e^{\left(-\sum_{i=1}^{N} |x_i| \right)}. \tag{2.16}$$

Based on this prior for $\mathbf{x}$, the MAP estimator problem for $\mathbf{x}$ using the model given in (4.14) reduces to the BP method given in (2.13) [28, 35].

Jeffreys Prior In this technique we assign the Jeffreys prior to the vector $\mathbf{x}$ that is expressed as [43, 85]

$$p(\mathbf{x}) \propto \prod_{i=1}^{N} \left(\frac{1}{|x_i|} \right). \tag{2.17}$$

The MAP estimator problem for $\mathbf{x}$ based on this prior distribution is then described as

$$\begin{aligned} \min_{\mathbf{x}} \quad & \sum_{i=1}^{N} \log(|x_i|) \\ \text{subject to} \quad & \|\mathbf{y} - \mathbf{A}\mathbf{x}\|_2 \leq \beta_j. \end{aligned} \tag{2.18}$$

The problem with (2.18) is that it suffers from numerous local minima [28, 86].

The FOCUSS Method In the FOCUSS method, a generalized Gaussian distribution is assigned to the vector $\mathbf{x}$ as a prior which is described as [87]

$$p(\mathbf{x}) \propto e^{\left(-\sum_{i=1}^{N} |x_i|^p \right)}. \tag{2.19}$$

Consequently, the MAP estimator problem for $\mathbf{x}$ is given as

$$\begin{aligned} \min_{\mathbf{x}} \quad & \sum_{i=1}^{N} |x_i|^p \\ \text{subject to} \quad & \|\mathbf{y} - \mathbf{A}\mathbf{x}\|_2 \leq \beta_f. \end{aligned} \tag{2.20}$$

As can be seen from (2.20), for $p = 1$ the MAP estimator problem reduces to BP and the optimization problem can be solved using CVX software package for example. However, for $0 \leq p < 1$ the optimization problem given in (2.20) is non-convex and to find the MAP estimator for $\mathbf{x}$ we follow [28] and present the result which is based on the expectation maximization (EM) algorithm. However, before expressing the result we should set the stage. We first rewrite (2.20) as

$$\min_{\mathbf{x}} \quad \left\{ \|\mathbf{y} - \mathbf{A}\mathbf{x}\|_2 + \lambda_f \sum_{i=1}^{N} |x_i|^p \right\} \tag{2.21}$$

in which λ_f is a parameter to be tuned. Each generalized Gaussian prior is then expressed as a set of latent variables $\boldsymbol{\gamma} = [\gamma_1, \gamma_2, \cdots, \gamma_N]^T$ which are treated as hidden data. We have given the pseudo-code for the implementation of the FOCUSS method using EM in Algorithm 1 where $\boldsymbol{\Gamma} = \text{diag}(\boldsymbol{\gamma})$. The stopping criterion is based on $\frac{\|\boldsymbol{\gamma}-\boldsymbol{\gamma}_{old}\|_2}{\|\boldsymbol{\gamma}\|_2}$, where $\boldsymbol{\gamma}_{old}$ is the value for $\boldsymbol{\gamma}$ in the last iteration. The algorithm stops when $\frac{\|\boldsymbol{\gamma}-\boldsymbol{\gamma}_{old}\|_2}{\|\boldsymbol{\gamma}\|_2} < \xi_f$.

Algorithm 1 Implementation of the FOCUSS method using EM

*Initialization

Set $\boldsymbol{\gamma} = \mathbf{1}_{N\times 1}$

Set $\boldsymbol{\gamma}_{old} = \mathbf{0}_{N\times 1}$

while $\frac{\|\boldsymbol{\gamma}-\boldsymbol{\gamma}_{old}\|_2}{\|\boldsymbol{\gamma}\|_2} < \xi_f$ **do**

$\boldsymbol{\gamma}_{old} = \boldsymbol{\gamma}$

$\gamma_i = |\hat{x}_i|^{2-p}, \quad i \in \{1, 2, \cdots, N\}.$

$\hat{\mathbf{x}} = \boldsymbol{\Gamma}\mathbf{A}^\dagger \left(\lambda_f \mathbf{I} + \mathbf{A}\boldsymbol{\Gamma}\mathbf{A}^\dagger\right)^{-1} \mathbf{y},$

end while

Chapter 3

Sparse Signal Recovery based Imaging in the Presence of Mode Conversion with Application to Non-Destructive Testing

In this chapter we develop a sparse signal representation based algorithm for one layer ultrasonic imaging which takes the effect of mode conversion into account. We use an array of transducers to inspect a given test sample in the presence of mode conversion phenomenon. We first develop a model for one layer ultrasonic array imaging for single mode scenario. We further extend this model to the multi-modal scenario. We then cast our problem as a sparse signal representation problem. At the end we apply the proposed algorithm along with the existing algorithms in the literature to both simulated and experimental data and show the superiority of the proposed technique.

The organization of this chapter is as follows. In Section 3.1, we describe our data

model and formulate the mode conversion phenomenon. Also, a presentation of MC-MUSIC and MC-Capon methods, based on the model that we develop in this section, is given. In Section 3.2, we cast our problem as a sparse signal representation problem without considering the effect of mode conversion. Then, we extend the sparse signal representation model to handle the effect of multi-mode for both single- and multi-snapshot scenarios. In Section 3.3, we show the superiority of our proposed algorithm using simulated data as well as experimental measurements. Finally the conclusion is given in Section 3.4.

3.1 Preliminary

3.1.1 Data Model

Using an array of M transducers, let us assume that we aim to locate L scatterers in a medium. We simplify the problem of interest by assuming that the length of the transducers is much larger than the thikness of the sample [88, 89]. Indeed, the basic idea in 2-dimensional imaging using a 1-dimensional linear array relies on the assumption that in a 2-dimensional model, all quantities are invariant in the third dimension. Our results can be extended in a straightforward manner to a 3-dimensional setup, when a 2-dimensional array is utilized for 3-dimensional volumetric imaging. We present our model in frequency domain. Fig. 4.1 illustrates the geometry of the array and the reflectors. Any hypothetical reflector has the potential to convert the incident wave into multiple modes. The wave corresponding to each mode propagates with a velocity which is different from those of the other modes. We first describe the model for the array received signals in one mode. To do so, in the presence of white noise, the vector of array signals due to backscattering from all L scatterers,

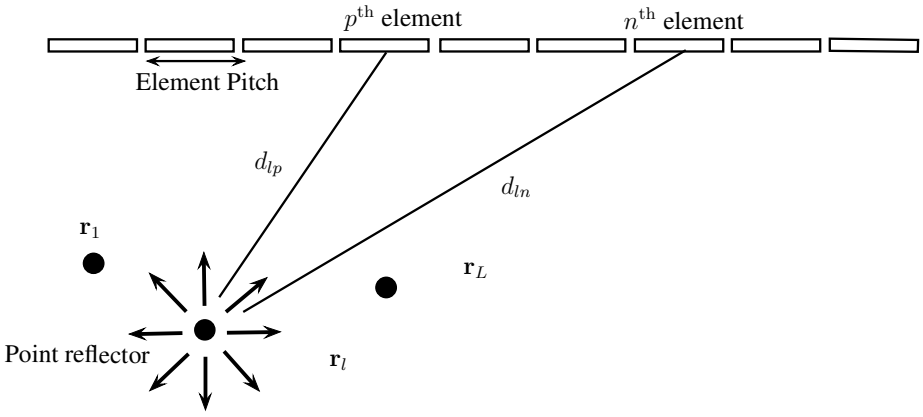

Figure 3.1: Array geometry.

when the p^{th} transducer transmits, can be written as

$$\mathbf{y}_p(\omega) = \mathbf{A}(\omega)\tilde{\mathbf{s}}_p(\omega) + \mathbf{w}_p(\omega) \tag{3.1}$$

where $\mathbf{y}_p(\omega) = [y_{1p}(\omega)\ y_{2p}(\omega)\ ...\ y_{Mp}(\omega)]^T$ is the $M \times 1$ vector of the array received signals, $y_{ip}(\omega)$ is the signal received by the i^{th} transducer when the p^{th} transducer is transmitting, and $\mathbf{A}(\omega)$ is an $M \times L$ matrix whose l^{th} column, denoted as $\mathbf{a}(\mathbf{r}_l, \omega)$, is the $M \times 1$ array steering vector (or the array spatial signature) of the l^{th} scatterer located at $\mathbf{r}_l$ and is given by

$$\mathbf{a}(\mathbf{r}_l, \omega) \triangleq [\frac{1}{\sqrt{d_{1l}}} e^{-jk_1(\omega)d_{1l}}\ \ \frac{1}{\sqrt{d_{2l}}} e^{-jk_1(\omega)d_{2l}}\ \ ...\ \ \frac{1}{\sqrt{d_{Ml}}} e^{-jk_1(\omega)d_{Ml}}]^T. \tag{3.2}$$

In (4.8), $k_1(\omega) \triangleq \frac{\omega}{c_1}$ and c_1 are the wavenumber and the propagation speed for Mode 1, respectively, $\frac{1}{\sqrt{d_{nl}}}$ and $e^{-jk_1(\omega)d_{nl}}$ are the attenuation and phase shift for the signal scattered by the l^{th} reflector and received by the n^{th} transducer, d_{nl} is the Euclidean distance between the l^{th} reflector, located at $\mathbf{r}_l$, and the n^{th} transducer. The $L \times 1$ vector $\tilde{\mathbf{s}}_p(\omega)$ is expressed as

$$\tilde{\mathbf{s}}_p(\omega) = [\tilde{s}_{p1}(\omega)\ \ \tilde{s}_{p2}(\omega)\ \ ...\ \tilde{s}_{pL}(\omega)]^T \tag{3.3}$$

where

$$\tilde{s}_{pl}(\omega) = \frac{1}{\sqrt{d_{pl}}} s_l e^{-jk_1(\omega)d_{pl}}, \qquad \text{for} \quad l \in \{1, 2, \ \cdots \ , L\}. \tag{3.4}$$

In (3.4), the real positive scalar s_l is the reflectivity coefficient of the l^{th} scatterer, while $\frac{1}{\sqrt{d_{pl}}}$ and $e^{-jk_1(\omega)d_{pl}}$ are, respectively, the attenuation and the phase shift that the signal transmitted by the p^{th} transducer goes through after it arrives at the l^{th} reflector. Finally, the $M \times 1$ noise vector is described as

$$\mathbf{w}_p(\omega) \triangleq [w_{p1}(\omega) \ w_{p2}(\omega) \ ... \ w_{pM}(\omega)]^T \tag{3.5}$$

where $w_{pi}(\omega)$ is the noise received by the i^{th} transducer, when the p^{th} transducer is transmitting. When multi-mode phenomenon occurs, each scatterer disperses the wave into multiple modes. Each mode has its own propagation speed with a distinct wavenumber, given as $k_r(\omega) = \frac{\omega}{c_r}$, where c_r is the propagation speed for the r^{th} mode. Therefore, the steering vector for the r^{th} mode and for the hypothetical reflector at location $\mathbf{r}_l$ is described as

$$\mathbf{a}^{(r)}(\mathbf{r}_l, \omega) \triangleq [\frac{1}{\sqrt{d_{1l}}} e^{-jk_r(\omega)d_{1l}} \ \frac{1}{\sqrt{d_{2l}}} e^{-jk_r(\omega)d_{2l}} \ ... \ \frac{1}{\sqrt{d_{lM}}} e^{-jk_r(\omega)d_{Ml}}]^T \tag{3.6}$$

where the superscript $^{(r)}$ stands for the r^{th} mode. We assume that each reflector has a reflection coefficient for each mode which is different from that of the other modes. Therefore, in the presence of multiple modes, we modify (3.4) as

$$\tilde{s}_{pl}^{(r)}(\omega) \triangleq \frac{1}{\sqrt{d_{pl}}} s_l^{(r)} e^{-jk_r(\omega)d_{pl}}, \qquad \text{for} \quad l \in \{1, 2, \ \cdots \ , L\} \tag{3.7}$$

where $s_l^{(r)}$ is the reflectivity coefficient of the l^{th} hypothetical reflector corresponding to the r^{th} mode. For a specific reflector located at $\mathbf{r}_l$, the energy conservation implies that

$$\sum_{r=1}^{R} \left(s_l^{(r)} \right)^2 = 1, \qquad \text{for} \quad l \in \{1, 2, \ \cdots \ , L\}. \tag{3.8}$$

Subsequently, we modify (3.3) for the r^{th} mode as

$$\tilde{\mathbf{s}}_p^{(r)}(\omega) \triangleq [\tilde{s}_{p1}^{(r)}(\omega) \;\; \tilde{s}_{p2}^{(r)}(\omega) \;\; ... \;\; \tilde{s}_{pL}^{(r)}(\omega)]^T \tag{3.9}$$

where we have introduced the superscript $^{(r)}$ to signify the r^{th} mode. Therefore, to accommodate the effect of all modes, the proposed model in (3.1) is modified as

$$\mathbf{y}_p(\omega) = \sum_{r=1}^{R} \mathbf{A}^{(r)}(\omega)\tilde{\mathbf{s}}_p^{(r)}(\omega) \;\; + \mathbf{w}_p(\omega). \tag{3.10}$$

In (3.10), $\mathbf{A}^{(r)}(\omega)$ is an $M \times L$ matrix whose l^{th} column is the steering vector, $\mathbf{a}^{(r)}(\mathbf{r}_l, \omega)$ given in (3.6), and summation is over R modes.

3.1.2 Previous work

In this section we present the work done in the literature, namely the MC-MUSIC and the MC-Capon methods [16], based on the model we have developed in (3.10).

Since we have M different snapshots, therefore, the sample covariance matrix can be calculated as

$$\hat{\mathbf{R}}(\omega) \triangleq \frac{1}{M} \sum_{p=1}^{M} \mathbf{y}_p(\omega)\mathbf{y}_p^H(\omega) \tag{3.11}$$

with $\mathbf{y}_p(\omega)$ given in (3.10). To present the final result for the MC-MUSIC and MC-Capon techniques, we first introduce the $M \times R$ matrix $\bar{\mathbf{A}}(\mathbf{r}, \omega)$ as

$$\bar{\mathbf{A}}(\mathbf{r}, \omega) \;\; \triangleq \;\; [\mathbf{a}^{(1)}(\mathbf{r}, \omega) \;\; \mathbf{a}^{(2)}(\mathbf{r}, \omega) \;\; \cdots \;\; \mathbf{a}^{(R)}(\mathbf{r}, \omega)] \tag{3.12}$$

where the r^{th} column, $\mathbf{a}^{(r)}(\mathbf{r}, \omega)$, is the steering vector (or the response) of the array to a hypothetical reflector located at point $\mathbf{r}$ at frequency ω and mode r. We now introduce the MC-MUSIC image as [16]

$$\mathcal{I}_{\text{MC-MUSIC}}(\mathbf{r}) \;\; = \;\; \sum_{\omega \in \Omega} \lambda_{\max} \left\{ \left(\bar{\mathbf{A}}^H(\mathbf{r}, \omega)\mathbf{E}_n(\omega)\mathbf{E}_n^H(\omega)\bar{\mathbf{A}}(\mathbf{r}, \omega) \right)^{-1} \bar{\mathbf{A}}^H(\mathbf{r}, \omega)\bar{\mathbf{A}}(\mathbf{r}, \omega) \right\} \tag{3.13}$$

where Ω is the set of all frequencies within the bandwidth of the probing signal. The locations of the scatterers can be estimated as those values of $\mathbf{r}$ for which the MC-MUSIC-based image $\mathcal{I}_{\mathrm{MC-MUSIC}}(\mathbf{r})$ has its L highest peaks.

The MC-Capon based image is also described as

$$\mathcal{I}_{\mathrm{MC-Capon}}(\mathbf{r}) = \sum_{\omega\in\Omega} \lambda_{\max}\left\{\left(\bar{\mathbf{A}}^H(\mathbf{r},\omega)\mathbf{R}_{\mathrm{DL}}^{-1}(\omega)\bar{\mathbf{A}}(\mathbf{r},\omega)\right)^{-1}\bar{\mathbf{A}}^H(\mathbf{r},\omega)\bar{\mathbf{A}}(\mathbf{r},\omega)\right\} \quad (3.14)$$

The locations of the scatterers can be estimated as those values of $\mathbf{r}$ for which the MC-Capon-based image $\mathcal{I}_{\mathrm{MC-Capon}}(\mathbf{r})$ has its L highest peaks.

3.2 Sparse Signal Recovery Based Algorithms

3.2.1 Single-mode

In this section, we present a method based on sparse signal recovery to image a material under test. We first formulate our problem as a sparse signal representation for a single-mode propagation environment, and then, extend that for a multi-modal propagation environment. In fact, since the goal in ultrasonic imaging is to image a limited number of reflectors inside materials, the problem can be easily viewed as a sparse signal recovery. To cast our data as a sparse signal representation, we need to replace $\mathbf{A}(\omega)$ with a new matrix which contains the steering vector for all hypothetical scatterers. In fact, $\mathbf{A}(\omega)$ contains the steering vectors of L true scatterers whose locations are not known, therefore $\mathbf{A}(\omega)$ itself is unknown. Now, we define an over complete basis (OCB) matrix which contains the steering vectors of all potential scatterers. To do so, we consider a sufficiently fine grid in the ROI in two dimensions where each pixel represents a potential scatterer. Fig. 3.2 shows this grid, with n_x pixels in the horizontal direction and n_z pixels in the vertical direction, resulting in a total number of pixels equal to $n_x \times n_z = N$.

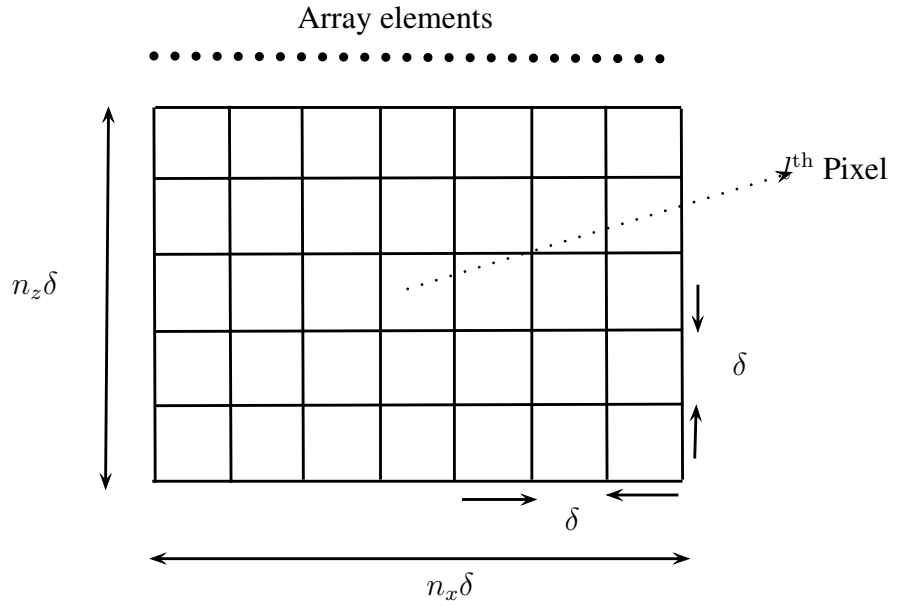

Figure 3.2: 2-dimensional grid covering the ROI

The steering vectors of these N potential scatterers will form the columns of the OCB matrix. This matrix should be over complete, meaning that N should be much greater than the number of transducers. Thus, the $M \times N$ OCB matrix $\tilde{\mathbf{A}}(\omega)$ is defined as

$$\tilde{\mathbf{A}}(\omega) \triangleq [\mathbf{a}(\tilde{\mathbf{r}}_1, \omega) \;\; \mathbf{a}(\tilde{\mathbf{r}}_2, \omega) \;\; \cdots \;\; \mathbf{a}(\tilde{\mathbf{r}}_N, \omega)]. \tag{3.15}$$

Here, $\mathbf{a}(\tilde{\mathbf{r}}_l, \omega)$ is the steering vector given in (4.8), when $\mathbf{r}_l$ is replaced with $\tilde{\mathbf{r}}_l$, for a potential scatterer located at $(i,j)^{\text{th}}$ pixel in the ROI, where $i = \lfloor \frac{l-1}{n_x} \rfloor + 1$ and $j = l - (i-1)n_x$ with coordinate vector $\tilde{\mathbf{r}}_l = ((i-1)\delta, (j-1)\delta)$ and δ is the width of each pixel in x and y directions. Therefore, a sparse representation of our model in (3.1) is given as

$$\mathbf{y}_p(\omega) = \tilde{\mathbf{A}}(\omega)\mathbf{x}_p + \mathbf{w}_p(\omega) \tag{3.16}$$

where $\mathbf{x}_p$ is an $N \times 1$ complex vector whose l^{th} element is nonzero if there is a scatterer located at the $(i,j)^{\text{th}}$ pixel where $i = \lfloor \frac{l-1}{n_x} \rfloor + 1$ and $j = l - (i-1)n_x$ and it

is zero, otherwise. Each nonzero element of $\mathbf{x}_p$ is one of the entries of $\tilde{\mathbf{s}}_p(\omega)$, given in (3.3). Now, to recover the sparse vector $\mathbf{x}_p$, we can use the basis pursuit de-noising method [41, 42], i.e., we can solve the following optimization problem:

$$\begin{aligned} \min_{\mathbf{x}_\mathrm{p}} \quad & \|\mathbf{x}_p\|_1 \\ \text{subject to} \quad & \|\mathbf{y}_p(\omega) - \tilde{\mathbf{A}}(\omega)\mathbf{x}_p\|_2 \leq \beta \end{aligned} \tag{3.17}$$

where β is the regularization parameter and is chosen such that the probability of the norm of the noise vector being larger than β is small. After obtaining $\mathbf{x}_p$, we reshape it into an $n_z \times n_x$ matrix which represents the final image. Therefore, in light of (3.3) and (3.4), s_l can be estimated as $|\sqrt{d_{pl}}x_{pl}|$ for the $(i,j)^{\text{th}}$ pixel in the ROI, where $i = \lfloor \frac{l-1}{n_x} \rfloor + 1$ and $j = l - (i-1)n_x$ and x_{pl} is the l^{th} entry of $\mathbf{x}_p$. Note however that the optimization problem (3.17) cannot be used when mode conversion exists. Note that in (3.17), any of the transducers can be chosen to fire the sound wave with the same OCB matrix $\tilde{\mathbf{A}}(\omega)$.

3.2.2 Multi-modal imaging using one snapshot

So far, we have formulated a single-mode imaging problem using sparse signal representation. We now take the effect of all modes into account. In the presence of mode conversion, the reflected signals received by the transducers from a specific scatterer is the superposition of all modes. To formulate the imaging problem in the presence of mode conversion using a sparse signal recovery problem, we need a new OCB matrix which contains the steering vectors for all the potential scatterers in all different modes. The OCB matrix in (3.15) was defined only for Mode 1. Using the same idea used in the previous section, the OCB matrix for the r^{th} mode is defined as

$$\tilde{\mathbf{A}}^{(r)}(\omega) \triangleq [\mathbf{a}^{(r)}(\tilde{\mathbf{r}}_1, \omega) \;\; \mathbf{a}^{(r)}(\tilde{\mathbf{r}}_2, \omega) \;\; \cdots \;\; \mathbf{a}^{(r)}(\tilde{\mathbf{r}}_N, \omega)] \tag{3.18}$$

where $\mathbf{a}^{(r)}(\tilde{\mathbf{r}}_l, \omega)$ is the steering vector for the r^{th} mode and for the potential scatterer located at $(i,j)^{\text{th}}$ pixel in the ROI, where $i = \lfloor \frac{l-1}{n_x} \rfloor + 1$ and $j = l - (i-1)n_x$, when

we replace $\mathbf{r}_l$ with $\tilde{\mathbf{r}}_l$ in (3.6). Therefore, we define a new $M \times NR$ OCB matrix as

$$\check{\mathbf{A}}(\omega) \triangleq [\tilde{\mathbf{A}}^{(1)}(\omega) \;\; \tilde{\mathbf{A}}^{(2)}(\omega) \;\; \cdots \;\; \tilde{\mathbf{A}}^{(R)}(\omega)] \tag{3.19}$$

where R is the number of modes. Based on (3.19), our model in (3.10) can be equivalently written as

$$\mathbf{y}_p(\omega) = \check{\mathbf{A}}(\omega)\check{\mathbf{x}}_p + \mathbf{w}_p(\omega) \tag{3.20}$$

where the $NR \times 1$ complex vector $\check{\mathbf{x}}_p$ is given as

$$\check{\mathbf{x}}_p = \begin{bmatrix} \mathbf{x}_p^{(1)} \\ \mathbf{x}_p^{(2)} \\ \vdots \\ \mathbf{x}_p^{(R)} \end{bmatrix}. \tag{3.21}$$

where $\mathbf{x}_p^{(r)}$, for $r \in \{1, 2, \cdots, R\}$, is a $N \times 1$ vector whose l^{th} element is nonzero if there is a scatterer located at the $(i,j)^{\text{th}}$ pixel where $i = \lfloor \frac{l-1}{n_x} \rfloor + 1$ and $j = l - (i-1)n_x$ and it is zero otherwise. Indeed, each nonzero element of $\mathbf{x}_p^{(r)}$ is one of the entries of $\tilde{\mathbf{s}}_p^{(r)}(\omega)$, given in (3.9). Based on (3.7) and (3.8), we assume energy conversion holds implying that

$$\sum_{r=1}^{R} \left| \sqrt{d_{pl}} x_{pl}^{(r)} e^{jk_r(\omega)d_{pl}} \right|^2 = \sum_{r=1}^{R} \left| \sqrt{d_{pl}} x_{pl}^{(r)} \right|^2 = 1, \qquad \text{for} \quad l \in \{1, 2, \cdots, L\} \tag{3.22}$$

where $x_{pl}^{(r)}$ is the l^{th} entry of $\mathbf{x}_p^{(r)}$ corresponding to the l^{th} pixel in the ROI. However, since the locations of the reflectors are unknown, we cannot use (3.22) in our ℓ_1 minimization problem. As such, we modify (3.22) and relax it as

$$\sum_{r=1}^{R} \left| \sqrt{d_{pl}} x_{pl}^{(r)} \right|^2 \leq 1, \qquad \text{for} \quad l \in \{1, 2, \ldots, N\}. \tag{3.23}$$

Note that (3.23) is a relaxation of (3.22) which holds not only for the non-zero entries of $\{\mathbf{x}_p^{(r)}\}_{r=1}^R$ but also for the zero entries. Another advantage of using (3.23) instead of (3.22) is that unlike (3.22), the restriction in (3.23) is a convex constraint. Then, to take the effect of all modes into account, we use (3.23) and modify the ℓ_1-norm minimization in (3.17) as

$$\begin{aligned} \min_{\check{\mathbf{x}}_\mathrm{p}} \quad & \|\check{\mathbf{x}}_p\|_1 \\ \text{subject to} \quad & \|\mathbf{y}_p(\omega) - \check{\mathbf{A}}(\omega)\check{\mathbf{x}}_p\|_2 \leq \beta \\ & \sum_{r=1}^{R} |\sqrt{d_{pl}} x_{pl}^{(r)}|^2 \leq 1, \qquad \text{for} \quad l \in \{1, 2, \cdots, N\}. \end{aligned} \tag{3.24}$$

The optimization problem in (3.24) is convex and it can be efficiently solved using any convex problem solver. Note that the patterns of sparsity for all $\{\mathbf{x}_p^{(r)}\}_{r=1}^R$ are the same, because all of them are describing the location of the same scatterers but in different modes. We hence introduce the final estimated vector $\mathbf{u} \triangleq [u_1, u_2, \cdots, u_N]$, where the l^{th} entry is given as $u_l = \sum_{r=1}^R |x_{pl}^{(r)}|, (\text{for, } l \in \{1, 2, \cdots, N\})$. Then, we reshape $\mathbf{u}$ into an $n_z \times n_x$ matrix to represent the final image.

3.2.3 Multi-mode imaging using multiple snapshots

In the previous section, we used only the data corresponding to one snapshot, i.e., when one transducer is illuminating the ROI. Using only one snapshot is one of the advantages for the sparse representation based approach presented in the previous subsection. However, when different snapshots are available, it makes sense to incorporate them into the imaging algorithm. Each snapshot of the data corresponds to one vector of the data measured by all transducers when one of the transducers emits an ultrasonic wave. In order to incorporate all snapshots (i.e., all measurement vectors corresponding to different transducers emitting ultrasonic waves one after the other) we stack the snapshots on top of each other. As such, we need to reformulate

our data model to allow different snapshots to be incorporated in the sparse signal recovery problem. To be able to use all snapshots, we need a new version of the OCB matrix. To introduce this new OCB matrix, we need to take a closer look at the geometry of our model. When a signal is transmitted by the p^{th} transmitter and received at the location of the l^{th} scatterer, it first undergoes a phase shift equal to $e^{-jk_1(\omega)d_{pl}}$ which is due to the distance between the transmitter and the scatterer. Another phase shift is experienced by the signal when it bounces off the scatterer and is received by the n^{th} receiver and this phase shift is equal to $e^{-jk_m(\omega)d_{nl}}$. In (3.4), the effect of the former phase shift has been given to the reflectivity coefficients of the scatterers. However, we can also bring this part of the phase shift into the steering vectors. Another factor that should be included in the steering vector is the attenuation for the signal transmitted by the p^{th} transducer and received at the l^{th} reflector which is equal to $\frac{1}{\sqrt{d_{pl}}}$. Therefore, when the p^{th} transducer transmits and the l^{th} hypothetical scatterer (located at $\tilde{\mathbf{r}}_l = ((i-1)\delta, (j-1)\delta)$, where $i = \lfloor \frac{l-1}{n_x} \rfloor + 1$ and $j = l-(i-1)n_x$) reflects the signal back toward the receivers, the $M \times 1$ steering vector for the r^{th} mode (which takes the effect of these new phase shifts into account) is described as

$$\mathbf{a}_p^{(r)}(\mathbf{r}_l, \omega) = \left[\frac{1}{\sqrt{d_{1l}d_{pl}}} e^{-j(k_1(\omega)d_{1l}+k_r(\omega)d_{pl})} \quad \frac{1}{\sqrt{d_{2l}d_{pl}}} e^{-j(k_1(\omega)d_{2l}+k_r(\omega)d_{pl})} \quad \ldots \right.$$
$$\left. \frac{1}{\sqrt{d_{Ml}d_{pl}}} e^{-j(k_1(\omega)d_{Ml}+k_r(\omega)d_{pl})} \right]^T . \quad (3.25)$$

We now modify our data model in (3.10) for the multiple snapshot case as

$$\mathbf{y}(\omega) = \sum_{r=1}^{R} \underline{\mathbf{A}}^{(r)}(\omega)\underline{\mathbf{s}}^{(r)} + \mathbf{w}(\omega). \quad (3.26)$$

Here, $\mathbf{y}(\omega)$ is an $M^2 \times 1$ vector which is described as

$$\mathbf{y}(\omega) \triangleq \begin{bmatrix} \mathbf{y}_1(\omega) \\ \mathbf{y}_2(\omega) \\ \vdots \\ \mathbf{y}_M(\omega) \end{bmatrix} \tag{3.27}$$

and the $M^2 \times L$ matrix $\underline{\mathbf{A}}^{(r)}(\omega)$ is defined as

$$\underline{\mathbf{A}}^{(r)}(\omega) \triangleq \begin{bmatrix} \underline{\mathbf{A}}_1^{(r)}(\omega) \\ \underline{\mathbf{A}}_2^{(r)}(\omega) \\ \vdots \\ \underline{\mathbf{A}}_M^{(r)}(\omega) \end{bmatrix} \tag{3.28}$$

where, for $r \in \{1, 2, \cdots, R\}$, $\underline{\mathbf{A}}_p^{(r)}(\omega)$ is an $M \times L$ matrix whose l^{th} column is the $M \times 1$ array steering vector $\mathbf{a}_p^{(r)}(\mathbf{r}_l, \omega)$, given in (3.25). Also, the $L \times 1$ vector $\underline{\mathbf{s}}^{(r)}$ is defined as[1]

$$\underline{\mathbf{s}}^{(r)} = [s_1^{(r)} \;\; s_2^{(r)} \;\; \cdots \;\; s_L^{(r)}]^T. \tag{3.29}$$

Finally, the $M^2 \times 1$ noise matrix $\mathbf{w}(\omega)$ is described as

$$\mathbf{w}(\omega) \triangleq \begin{bmatrix} \mathbf{w}_1(\omega) \\ \mathbf{w}_2(\omega) \\ \vdots \\ \mathbf{w}_M(\omega) \end{bmatrix} \tag{3.30}$$

where $\mathbf{w}_p(\omega)$ is the $M \times 1$ vector of the noise received by the array when the p^{th} transducer transmits. Then, based on the steering vector given in (3.25) a new OCB

[1]Defining the signal vector $\tilde{\mathbf{s}}_p^{(r)}(\omega)$ as in (3.9) allows us to use the same OCB matrix $\mathbf{A}^{(r)}(\omega)$ in (3.10) for all values of p. Doing so will allow us to save on the amount of the memory used for storing this OCB matrix. Such a definition cannot be used for $\underline{\mathbf{s}}^{(r)}$ when all transducers data is used.

matrix, for the r^{th} mode and for the case when the p^{th} transducer transmits, is defined as

$$\tilde{\bar{\mathbf{A}}}_p^{(r)}(\omega) \triangleq [\mathbf{a}_p^{(r)}(\tilde{\mathbf{r}}_1,\omega) \;\; \mathbf{a}_p^{(r)}(\tilde{\mathbf{r}}_2,\omega) \;\; \cdots \;\; \mathbf{a}_p^{(r)}(\tilde{\mathbf{r}}_N,\omega)]. \tag{3.31}$$

Finally, we can define our augmented $M \times NR$ OCB matrix, composed of all R modes when the p^{th} transducer transmits, as

$$\bar{\bar{\mathbf{A}}}_p(\omega) \triangleq [\tilde{\bar{\mathbf{A}}}_p^{(1)}(\omega) \;\; \tilde{\bar{\mathbf{A}}}_p^{(2)}(\omega) \;\; \cdots \;\; \tilde{\bar{\mathbf{A}}}_p^{(R)}(\omega)]. \tag{3.32}$$

A sparse representation of our model given in (3.25), is described as

$$\mathbf{y}(\omega) = \breve{\mathbf{A}}(\omega)\breve{\mathbf{x}} + \mathbf{w}(\omega) \tag{3.33}$$

where $\breve{\mathbf{A}}(\omega)$ is an $M^2 \times NR$ OCB matrix defined as

$$\breve{\mathbf{A}}(\omega) \triangleq \begin{bmatrix} \bar{\bar{\mathbf{A}}}_1(\omega) \\ \bar{\bar{\mathbf{A}}}_2(\omega) \\ \vdots \\ \bar{\bar{\mathbf{A}}}_M(\omega) \end{bmatrix}. \tag{3.34}$$

and $NR \times 1$ vector $\breve{\mathbf{x}}$ is expressed as

$$\breve{\mathbf{x}} = \begin{bmatrix} \bar{\mathbf{x}}^{(1)} \\ \bar{\mathbf{x}}^{(2)} \\ \vdots \\ \bar{\mathbf{x}}^{(R)} \end{bmatrix} \tag{3.35}$$

Each nonzero element of $\bar{\mathbf{x}}^{(r)}$ is one of the real- and positive-valued entries of $\underline{\mathbf{s}}^{(r)}$, given in (3.29). Consequently, the energy conservation assumption for the wave amplitude given in (3.7) is described as

$$\sum_{r=1}^{R} |\bar{x}_l^{(r)}|^2 = 1, \qquad \text{for} \quad l \in \{1, 2, \cdots, L\} \tag{3.36}$$

where $\bar{x}_l^{(r)}$ is the l^{th} entry of $\bar{\mathbf{x}}_r^{(r)}$ corresponding to the l^{th} pixel in the ROI. However, since the locations of the reflectors are unknown, we cannot use (3.36) in our ℓ_1 minimization problem. Therefore, we modify (3.36) and relax it as

$$\sum_{r=1}^{R} |\bar{x}_l^{(r)}|^2 \leq 1, \qquad \text{for} \quad l \in \{1, 2, \cdots, N\} \tag{3.37}$$

It should be noted that (3.37) is a relaxation of (3.36) which holds not only for the non-zero entries of $\{\bar{\mathbf{x}}^{(r)}\}_{r=1}^{R}$ but also for the zero entries. Based on (3.33) and (3.37), our new ℓ_1 optimization problem is written as

$$\begin{aligned} \min_{\breve{\mathbf{x}}} \quad & \|\breve{\mathbf{x}}\|_1 \\ \text{subject to} \quad & \|\mathbf{y}(\omega) - \breve{\mathbf{A}}(\omega)\breve{\mathbf{x}}\|_2 \leq \beta \\ & \sum_{r=1}^{R} |\bar{x}_l^{(r)}|^2 \leq 1, \qquad \text{for} \quad l \in \{1, 2, \cdots, N\} \\ & \bar{\mathbf{x}}^{(r)} \succeq \mathbf{0}, \qquad \text{for} \quad r \in \{1, 2, \cdots, R\}. \end{aligned} \tag{3.38}$$

The fact that each nonzero element of $\bar{\mathbf{x}}^{(r)}$ is one of the real- and positive-valued entries of $\underline{\mathbf{s}}^{(r)}$, given in (3.29), has inspired us to introduce the last set of constraints in (3.38). When it comes to implementation, (3.38) seems to be computationally prohibitive as the size of the problem is very large. Instead of solving (3.38) directly, we use the basic idea behind compressive sensing which is used for size reduction [30]. The idea is based on reducing the size of the problem by using a transformation which is given by matrix $\mathbf{\Phi}$. The only constraint on $\mathbf{\Phi}$ is that it should be an isometry which simply means that it should be distance preserving. It has been proved that a random Gaussian matrix with a sufficient number of rows satisfies the so-called restricted isometry property (RIP) condition [90]. In general, the computational complexity of verifying the RIP is combinatorial for a given measurement matrix. A surprising result in compressing sensing is that for K-sparse signals a random matrix $\mathbf{\Phi}$ with Gaussian entries and with $\tilde{L} \geq \mathcal{O}(K \log(N/K))$ rows satisfies the RIP with

overwhelming probability, see [91] and [92] for the detail of this analysis. Based on this idea, we can multiply our data model in (3.26) by an $\tilde{L} \times M^2$ random matrix $\mathbf{\Phi}$. By choosing a small $\tilde{L}$, the size of the problem can be reduced drastically from M^2 to $\tilde{L}$. Consequently the new data model is expressed as

$$\breve{\mathbf{y}}(\omega) = \mathbf{B}(\omega)\breve{\mathbf{x}} + \breve{\mathbf{w}}(\omega) \tag{3.39}$$

where the $\tilde{L} \times 1$ vector $\breve{\mathbf{y}}(\omega)$ is defined $\breve{\mathbf{y}}(\omega) \triangleq \mathbf{\Phi}\mathbf{y}(\omega)$ and the $\tilde{L} \times NR$ matrix $\mathbf{B}(\omega)$ is defined as $\mathbf{B}(\omega) \triangleq \mathbf{\Phi}\breve{\mathbf{A}}(\omega)$ and finally the $\tilde{L} \times 1$ noise vector $\breve{\mathbf{w}}(\omega)$ is defined as $\breve{\mathbf{w}}(\omega) \triangleq \mathbf{\Phi}\mathbf{w}(\omega)$. Therefore, we modify (3.38) as

$$\begin{aligned} \min_{\breve{\mathbf{x}}} \quad & \|\breve{\mathbf{x}}\|_1 \\ \text{subject to} \quad & \|\breve{\mathbf{y}}(\omega) - \ \mathbf{B}(\omega)\breve{\mathbf{x}}\|_2 \leq \beta \\ & \sum_{r=1}^{R} |\bar{x}_l^{(r)}|^2 \leq 1, \qquad \text{for} \quad l \in \{1, 2, \cdots, N\} \\ & \bar{\mathbf{x}}^{(r)} \succeq \mathbf{0}, \qquad \text{for} \quad r \in \{1, 2, \cdots, R\}. \end{aligned} \tag{3.40}$$

Once $\breve{\mathbf{x}}$ is obtained, we can obtain the vectorized version of the image of the ROI as $\bar{\mathbf{u}} = \sum_{r=1}^{R} \bar{\mathbf{x}}^{(r)}$. Reshaping $\mathbf{u}$ into an $n_z \times n_x$ matrix, we obtain the final image.

3.2.4 Block Sparsity

Note that the ℓ_1 norm minimization problem in (3.40) ignores the fact that the vectors $\{\bar{\mathbf{x}}^{(r)}\}_{r=1}^{R}$ have the same sparsity pattern. In order to exploit such a block sparsity structure in $\breve{\mathbf{x}}$, we can use the so-called mixed ℓ_2/ℓ_1 minimization approach which

solves the following minimization problem [93]:

$$\begin{aligned}
\min_{\breve{\mathbf{x}}} \quad & \sum_{l=1}^{N} \sqrt{\sum_{r=1}^{R} |\bar{x}_l^{(r)}|^2} \\
\text{subject to} \quad & \|\breve{\mathbf{y}}(\omega) - \mathbf{B}(\omega)\breve{\mathbf{x}}\|_2 \leq \beta \\
& \sum_{r=1}^{R} |\bar{x}_l^{(r)}|^2 \leq 1, \qquad \text{for} \quad l \in \{1, 2, \cdots, N\} \\
& \bar{\mathbf{x}}^{(r)} \succeq \mathbf{0}, \qquad \text{for} \quad r \in \{1, 2, \cdots, R\}.
\end{aligned} \tag{3.41}$$

The optimization problem (3.41) can be turned into a second order convex cone (SOC) programming described as

$$\begin{aligned}
\min_{\breve{\mathbf{x}},\zeta,\mathbf{q}} \quad & \zeta \\
\text{subject to;} \quad & \mathbf{1}^T\mathbf{q} \leq \zeta \\
& \sqrt{\sum_{r=1}^{R} (\bar{x}_l^{(r)})^2} \leq q_i, \quad \text{for} \quad i \in \{1, 2, \cdots, N\} \\
& \|\breve{\mathbf{y}}(\omega) - \mathbf{B}(\omega)\breve{\mathbf{x}}\|_2 \leq \beta \\
& \sum_{r=1}^{R} (\bar{x}_l^{(r)})^2 \leq 1, \qquad \text{for} \quad l \in \{1, 2, \cdots, N\} \\
& \bar{\mathbf{x}}^{(r)} \succeq \mathbf{0}, \qquad \text{for} \quad r \in \{1, 2, \cdots, R\}.
\end{aligned} \tag{3.42}$$

Once $\breve{\mathbf{x}}$ is obtained, we can obtain the vectorized version of the image of the ROI as $\bar{\mathbf{u}} = \sum_{r=1}^{R} \bar{\mathbf{x}}^{(r)}$. Reshaping $\mathbf{u}$ into an $n_z \times n_x$ matrix, we obtain the final image.

Remark: In Sections III.A and III.B, we incorporated the phase of the forward path into the unknown sparse image in order to ensure that the OCB matrix is the same regardless of the index of the transducer which is chosen to fire the ultrasonic wave, thereby saving storage required for saving this matrix when different transducers are used to illuminate the ROI. In Section III.C, this phase was incorporated into the spatial signatures of different points in the image. This is the only way that we can formulate the problem with multiple snapshots (i.e., with data measurements

Table 3.1: Simulated array parameters.

Array parameters	Value
Element type	rectangular
Number of elements	64
SNR	15 dB
Element Pitch	1.25 mm
Center Frequency	1 MHz
Sampling Frequency	10 MHz
X-position of the reflectors	-15 mm and 10 mm
Y-position of the reflectors	20 mm and 40 mm

corresponding to different emitting transducers) as a sparse signal recovery problem.

3.3 Numerical and Experimental Results

3.3.1 Numerical Results

In this subsection, we use numerical examples to show the superiority of the proposed algorithms compared to the MC-MUSIC and MC-Capon techniques. We consider a linear array of transducers which are illuminating an ROI containing two point reflectors. The specifications of the linear array have been summarized in Table 3.1. The acoustic wave generated by each transducer is a one-sided Gaussian modulated signal with a center frequency of 1 MHz. Fig. 3.3 shows the transmitted signal in both time- and frequency-domains. The pulse shape we use is a typical signal that a transducer produces, see for example [1]. The sampling frequency is 10 MHz.

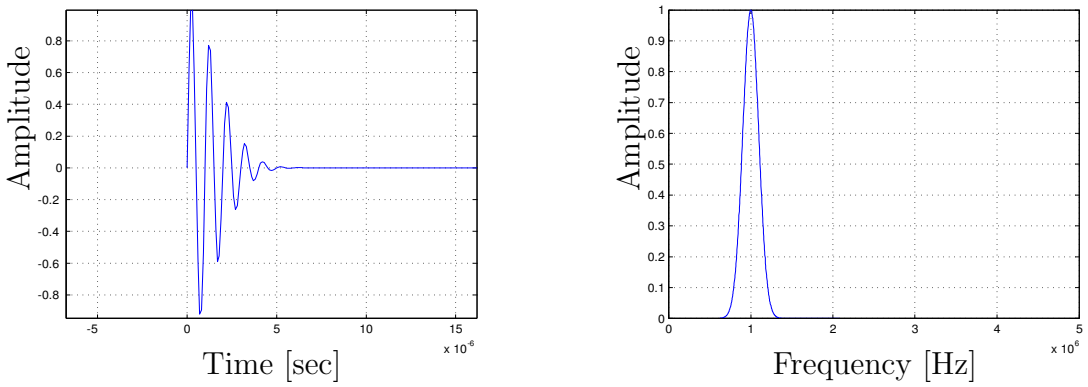

Figure 3.3: a) time domain signal. b) The spectrum of the signal in frequency domain.

The incident wave is assumed to be in longitudinal mode while the reflected wave is both longitudinal and shear wave. The velocities of longitudinal and shear waves are assumed to be 5010 and 2270 m/s, respectively.

The two-dimensional ROI stretch, horizontally (in x direction) from -50 mm to 50 mm and vertically (in y direction) from 0.0 to 100 mm, respectively. Two point reflectors are assumed to be located at $(-15, 20)$ mm and $(10, 40)$ mm. The SNR is 15 dB. We define the received SNR as

$$\text{SNR} = \frac{\sum_{\omega\in\Omega}\sum_{p=1}^{N} \|\mathbf{y}_p(\omega) - \mathbf{w}_p(\omega)\|^2}{\sum_{\omega\in\Omega}\sum_{p=1}^{N} \|\mathbf{w}_p(\omega)\|^2}$$

We use all 64 snapshots to estimate the sample covariance matrix based on (3.11). The true locations of the reflectors along with the images obtained by the MC-MUSIC and MC-Capon methods based on (3.13) and (3.14), are shown in Figs. 3.4 (a), (b), and (c), respectively. In these figures, for both reflectors, the reflectivity coefficients of longitudinal and shear waves are assumed to be equal to $\sqrt{2}/2$ and $\sqrt{2}/2$, respectively,

implying an equal power split between the two modes. A total of 20 frequency bins is used in the MC-MUSIC and MC-Capon methods while the sparse signal recovery based imaging techniques (3.24), (3.40), and (3.42) rely only on the data from the central frequency bin. The dimension of the signal subspace for the MC-MUSIC technique has been set to 2. The size of the image in all methods is chosen to be 100×100. Fig. 3.4-(d) shows the result for the technique in (3.24), where only one transducer (transducer number 32) is fired. Fig. 3.4-(e) shows the result of the ℓ_1 norm minimization problem (3.40), which uses the data corresponding to the case when all transducers are fired. Fig. 3.4-(f) illustrates the result of the ℓ_2/ℓ_1 norm minimization problem (3.42), which also uses the data corresponding to the case when all the transducers are fired. For the last two figures, the size of $\breve{\mathbf{y}}(\omega)$ is 4096×1 and matrix $\mathbf{\Phi}$ has been generated based on a Gaussian distribution. The size of $\mathbf{\Phi}$ has been selected as 200×4096. As can be seen from Fig. 3.4, for the sparse representation based techniques, the difference between the peak and the sidelobe levels is more than 110 dB, but this value for MC-MUSIC is less than 30 dB and that for MC-Capon is less than 25 dB. The RMSE of the location estimates versus SNR has been given in Fig. 3.5 for all the aforementioned techniques. As can be seen from this figure, the error for sparse representation methods based on (3.40) and (3.42) is lower than those of the MC-MUSIC and MC-Capon based techniques. It can also be seen from this figure that the method of (3.24) provides a satisfactory RMSE if the SNR is sufficiently high. Note that compared to the other four algorithms, the technique of (3.24) requires a significantly lower amount of data, thus having a higher RMSE. As can be seen from this figure, the method of (3.42) offers the lowest RMSE value for low values of SNR. This observation can be explained based on the fact that the method of (3.42) exploits the block sparsity in the sparse vector $\breve{\mathbf{x}}$.

Fig. 3.6 shows the probability of reflector detection for all five aforementioned methods. A reflector is said to have been detected if its location estimate is within

1 mm from its true location. This figure also shows the superior performance of the methods (3.40) and (3.42) compared to the other three methods.

Figs. 3.7 and 3.8 illustrate the RMSE curves for different methods for non-equal power split between the two modes. In Fig. 3.7, the reflectivity coefficients corresponding to longitudinal and shear waves are 0.6 and 0.8, respectively, while in Fig. 3.8, these coefficients are 1 and 0 (i.e., no mode conversion has occurred). As can be seen from these figures, in both scenarios, similar to the equal power split scenario shown in Fig. 3.5, the error for sparse signal representation methods based on (3.40) and (3.42) is lower than those of MC-MUSIC and MC-Capon based techniques. Therefore, from Figs. 3.5, 3.7 and 3.8 we conclude that regardless of how much contribution we have from the converted mode, our proposed methods outperform both MC-MUSIC and MC-Capon techniques by a large margin.

Fig. 3.9 illustrates the RMSE curves versus SNR for the ℓ_2/ℓ_1 mixed norm minimization approach with and without energy preserving constraints. As can be seen from this figure, eliminating these constraints has little to no effect for modest to high values of SNR.

Assuming that the velocity of the shear wave is known with error, Fig. 3.10 shows the RMSE curves versus the percentage of error in the knowledge of shear wave velocity. As can be seen from this figure, the proposed sparse signal recovery based methods are less sensitive to this type of error.

In Fig. 3.11, we show the performance for the ℓ_1 norm minimization method (3.40) for different values of $\tilde{L}$. As can be seen from this figure, for the scenario we consider, choosing $\tilde{L} = 200$ results in a very low value for RMSE even for low and moderate values of SNR.

In Fig. 3.12, we illustrate the RMSE curves versus SNR for the ℓ_1 norm minimization method (3.40) for different number of transducers when $\tilde{L} = 100$. As can be seen from this figure, by increasing the number of transducers, the performance

can be improved over a larger value of SNR.

3.3.2 Experimental Results

To show the performance of our sparse signal representation based methods, we use the same array measurements used in [1]. The real measurements have been taken with an ultrasonic phased array system. The array probe consists of 64 transducers with a pitch of 0.85 mm and gaps of 0.15 mm separating the transducers. The center frequency of the probe is 4 MHz with a 2 MHz bandwidth. The test setup is shown in Fig. 3.13. The measurements have been taken over a 20 mm thick carbon steel plate where the velocities of longitudinal and shear waves equal to 5900 and 3250 m/s, respectively and a 1.5 mm diameter bore hole drilled in the center, as shown in Fig. 3.13.

Figs. 3.14(a) and (b) show the images, as 3-dimensional plots, obtained by using the MC-MUSIC and MC-Capon methods based on (3.13) and (3.14), respectively. Fig. 3.14(c), (d) and (e) show the images, as 3-dimensional plots, for the sparse signal recovery based imaging techniques (3.24), (3.40), and (3.42), respectively. A total of 20 frequency bins are used in the MC-MUSIC and MC-Capon methods while the sparse signal recovery based imaging techniques (3.24), (3.40), and (3.42) rely only on the data from one frequency bin corresponding to the probe center frequency at 4 MHz. The dimension of the signal subspace for the MC-MUSIC technique has been set to 5. The value of the diagonal loading factor κ is chosen to be equal to 5000. Fig. 3.15 shows the same images in 2 dimensions. Note that the background noises in the images shown in Fig. 3.15 for our sparse signal representation based methods have very low amplitudes in the range -100 dB to -120 dB. As can be seen from Figs. 3.14 and 3.15, the proposed sparse signal representation based methods proposed in this paper are superior to the MC-Capon and MC-MUSIC methods.

3.4 Conclusions

Mode conversion is a common phenomenon in ultrasonic imaging. In this paper, we used sparse signal representation based approach to develop several imaging techniques which take mode conversion into account. The proposed methods have higher resolution and lower sidelobe levels in comparison with the state-of-the-art techniques, such as MUSIC and Capon based methods. Our sparse signal representation based techniques are robust to correlated targets. We have shown the performance superiority of our sparse signal representation based methods over existing methods using both simulated and experimental data.

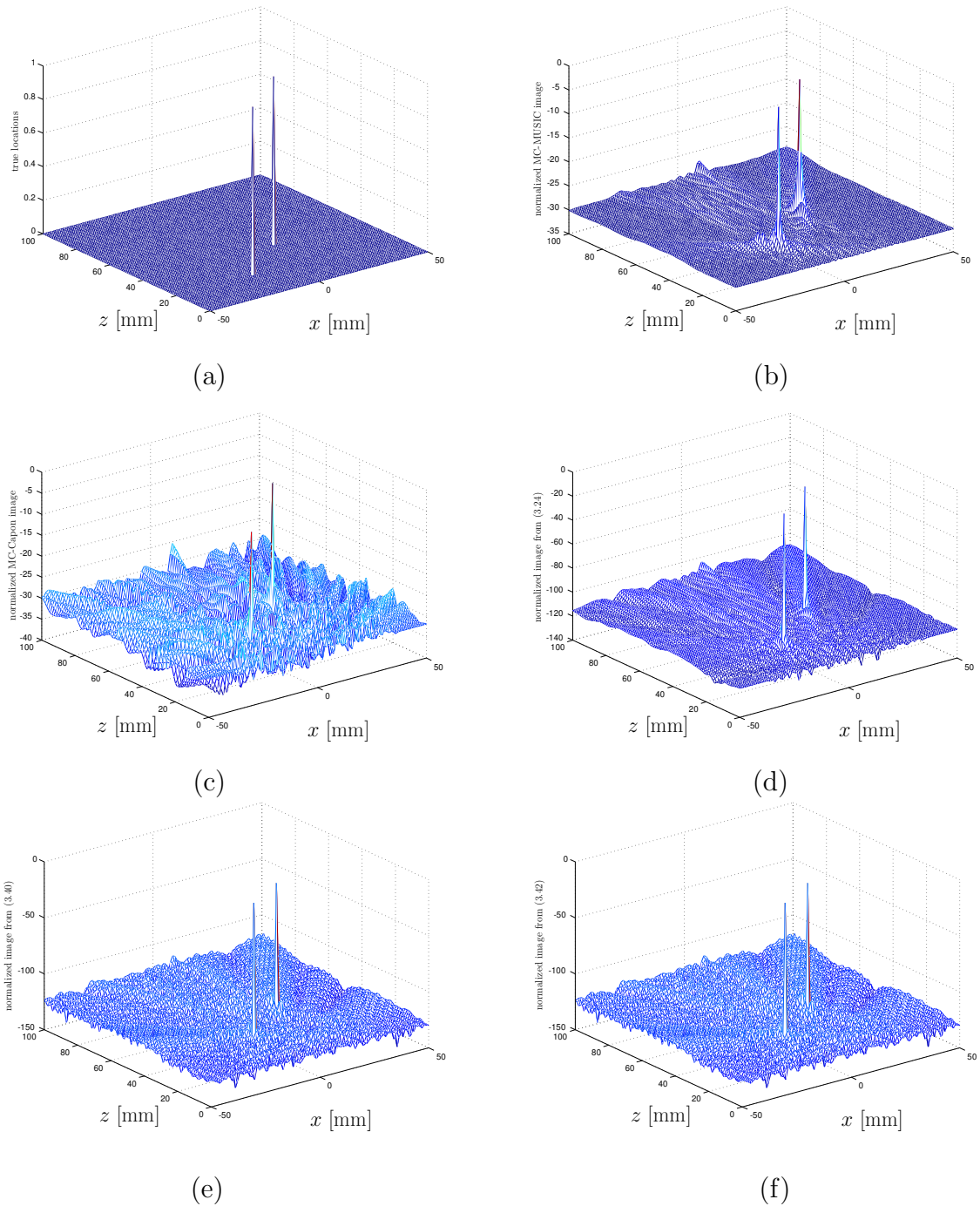

Figure 3.4: The normalized images for a) the true reflectors' locations, b) the MC-MUSIC based technique given in (3.13), c) the MC-Capon based method given in (3.14), d) the proposed technique in (3.24), e) the proposed technique in (3.40), and f) the proposed technique in (3.42).

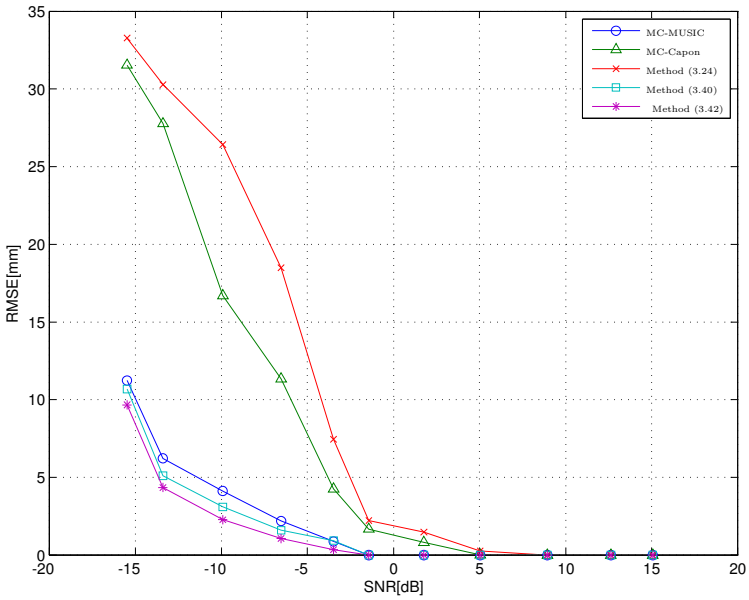

Figure 3.5: The RMSE of location estimates versus SNR, using the ℓ_1 norm minimization methods (3.24) and (3.40), the ℓ_2/ℓ_1 mixed norm minimization method (3.42) , MC-MUSIC and MC-Capon based approaches for equal power spilt between the two modes.

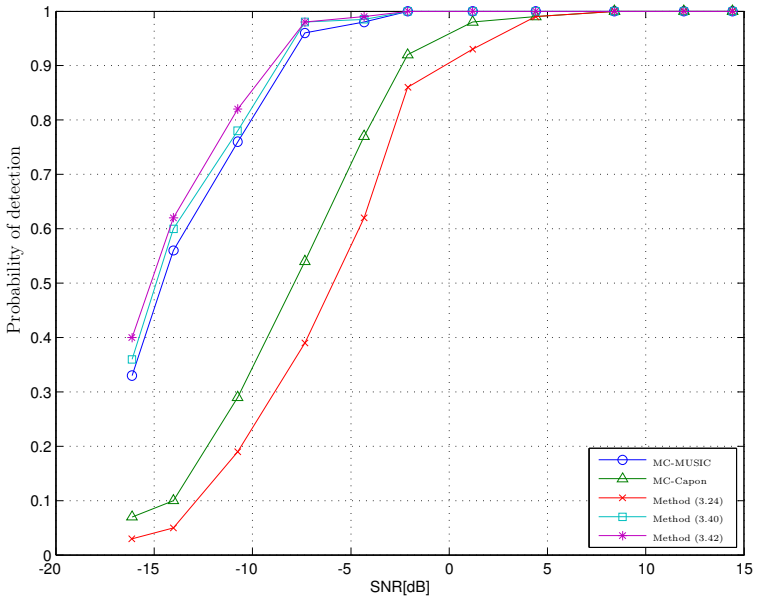

Figure 3.6: The probability of reflector detection versus SNR, using the ℓ_1 norm minimization methods (3.24) and (3.40) and ℓ_2/ℓ_1 mixed norm minimization method (3.42), MC-MUSIC and MC-Capon based approaches for equal power spilt between the two modes..

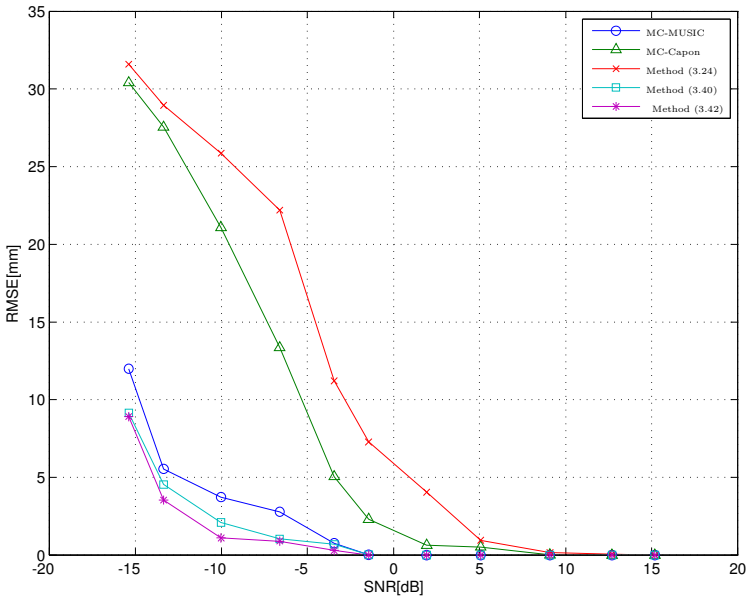

Figure 3.7: The RMSE of location estimates versus SNR, using the ℓ_1 norm minimization methods (3.24) and (3.40), the ℓ_2/ℓ_1 mixed norm minimization method (3.42), the MC-MUSIC and MC-Capon based approaches for reflectivity coefficients of longitudinal and shear waves equal to 0.6 and 0.8, respectively.

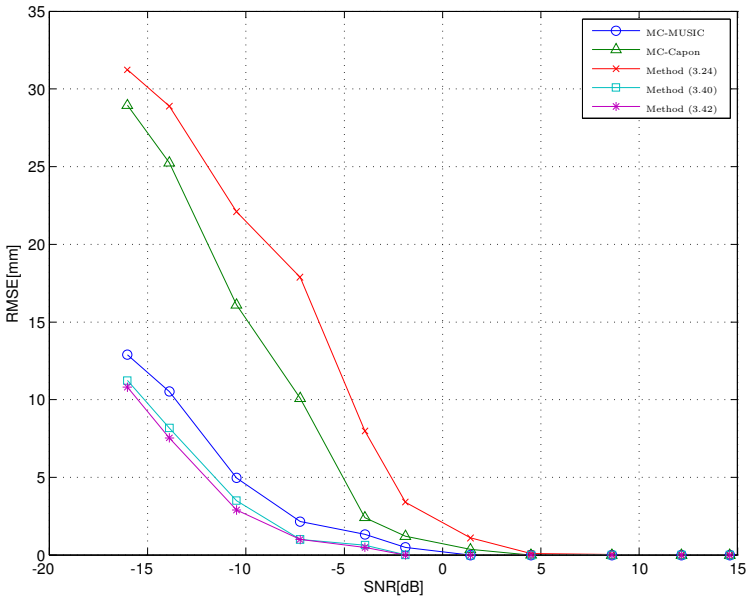

Figure 3.8: The RMSE of location estimates versus SNR, using the ℓ_1 norm minimization methods (3.24) and (3.40), the ℓ_2/ℓ_1 mixed norm minimization method (3.42), the MC-MUSIC and MC-Capon based approaches for reflectivity coefficients of longitudinal and shear waves equal to 1 and 0, respectively.

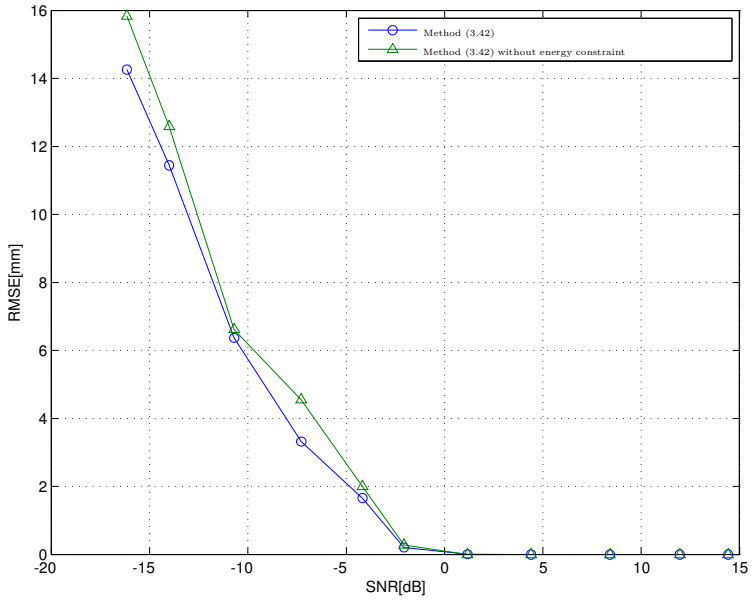

Figure 3.9: The RMSE curves versus SNR for the ℓ_2/ℓ_1 mixed norm minimization approach with and without the energy preserving constraints using (3.42).

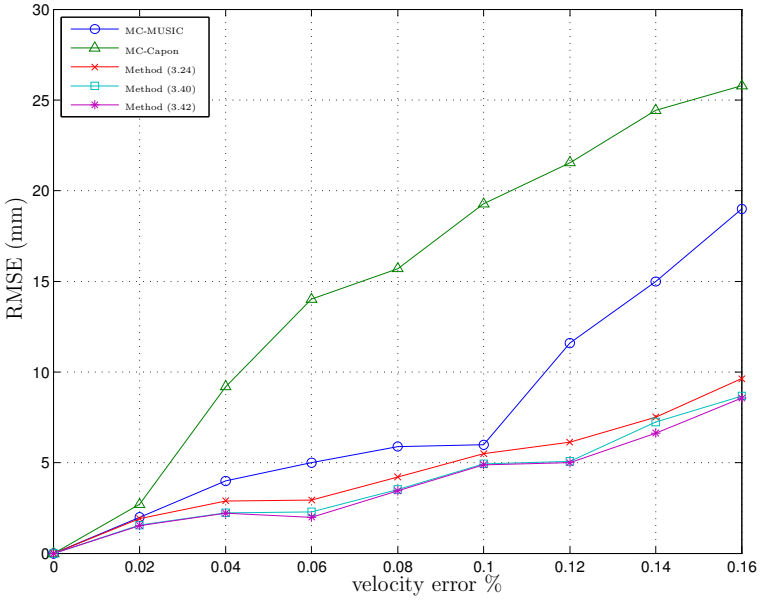

Figure 3.10: The RMSE curves versus the percentage of uncertainty in knowledge of shear wave velocity for different methods.

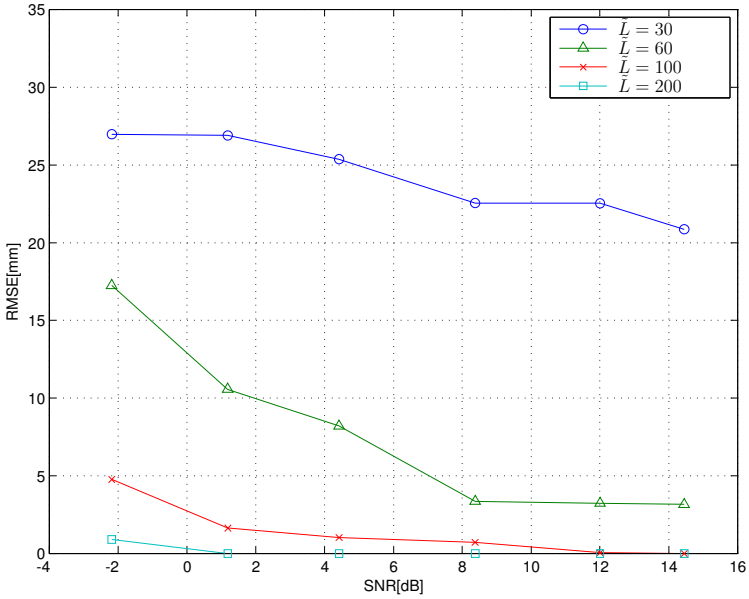

Figure 3.11: The RMSE curves versus SNR for the ℓ_1 norm minimization method (3.40) for different values of $\tilde{L}$.

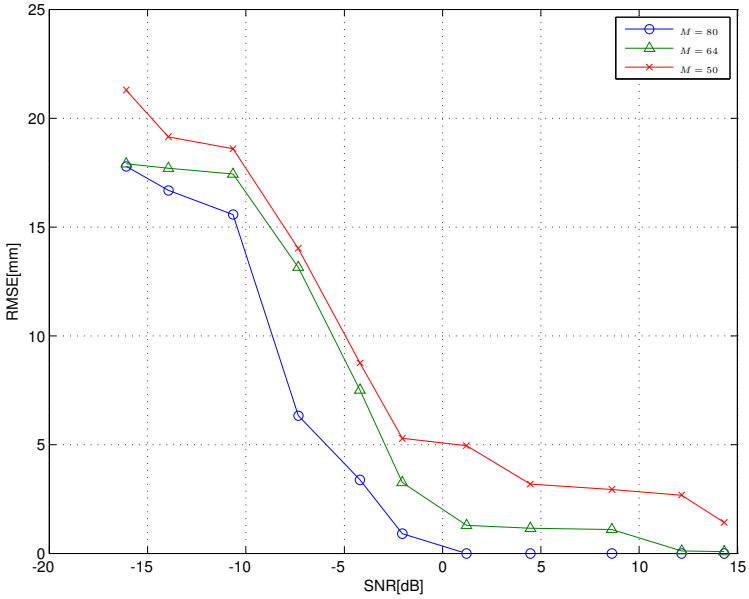

Figure 3.12: The RMSE curves versus SNR for the ℓ_1 norm minimization method (3.40) for different number of transducers and $\tilde{L} = 100$.

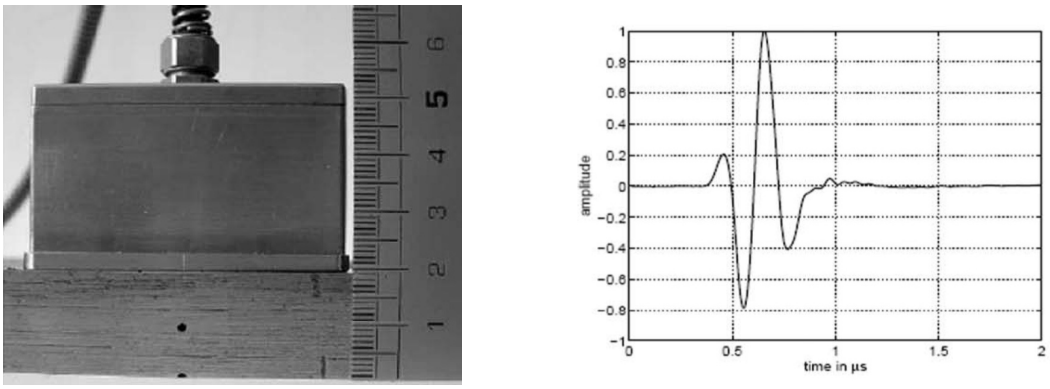

(a) (b)

Figure 3.13: a) Test setup, b) transmitted signal, courtesy of [1].

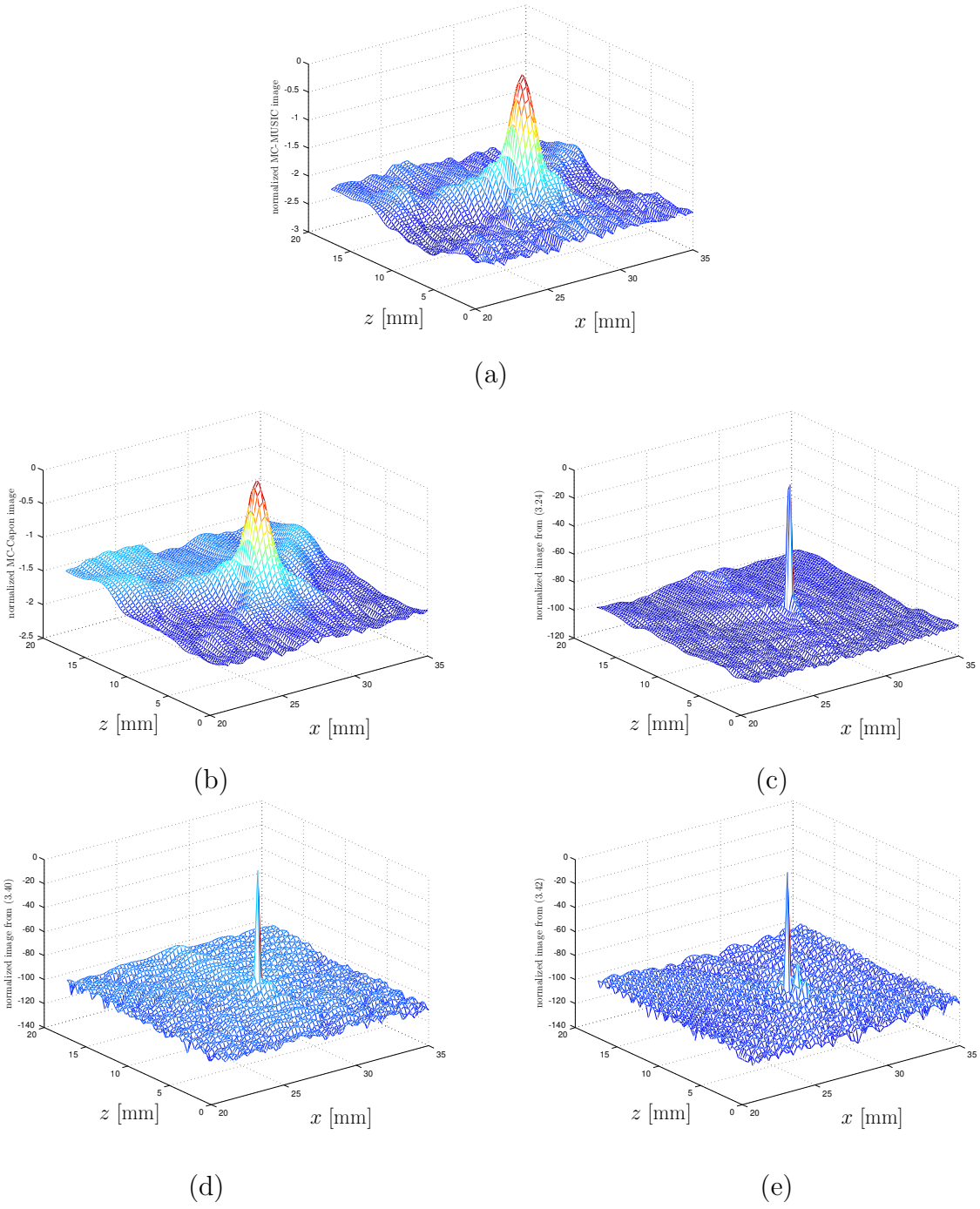

Figure 3.14: The normalized images obtained from data a) the MC-MUSIC based technique given in (3.13), b) the MC-Capon based method given in (3.14), c) the proposed technique in (3.24), d) the proposed technique in (3.40), and e) the proposed technique in (3.42).

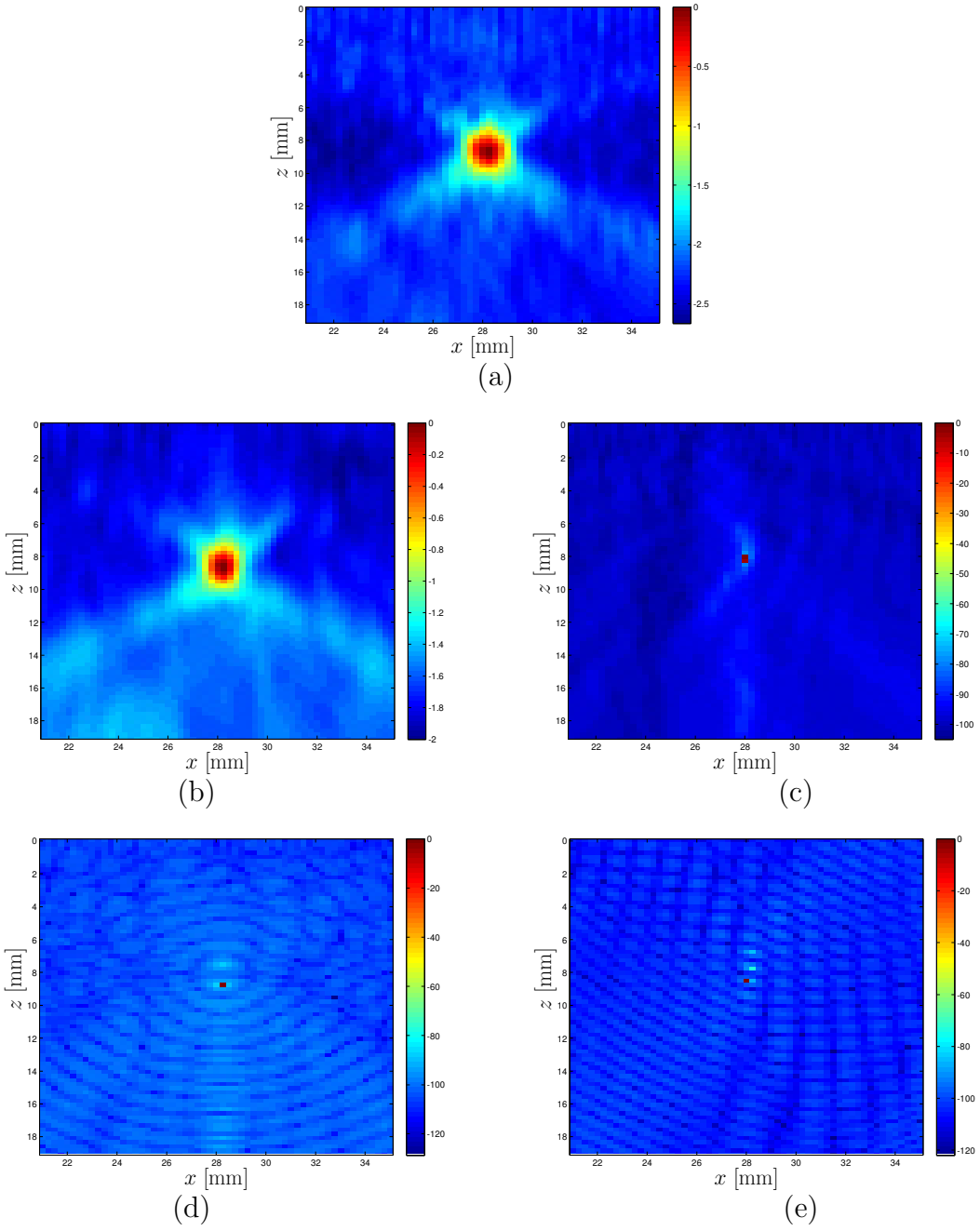

Figure 3.15: The normalized 2-dimensional images obtained from data a) the MC-MUSIC based technique given in (3.13), b) the MC-Capon based method given in (3.14), c) the proposed technique in (3.24), d) the proposed technique in (3.40), and e) the proposed technique in (3.42).

Chapter 4

Sparse Bayesian Learning with Application to Two-Layer Ultrasonic Array Imaging

In this chapter, we develop a sparse signal representation based imaging algorithm which relies on Bayesian inference. We use an array of ultrasonic transducers to inspect the internal structure of a test sample immersed in water. The goal is to find the reflectivity coefficients of the reflectors inside the test sample. We model the array spatial signature using Rayleigh-Sommerfeld diffraction formula. We then assign a Weibull distribution function to the desired reflectivity coefficients. To enforce sparsity, we model the scaling parameter of the Weibull distribution function with inverse Gamma distribution function. We also propose a new technique to estimate the shape parameter of the Weibull distribution function using Mellin transform. We aim to obtain the MAP estimator for the desired reflectivity coefficients. To accomplish this goal, we find the conditional posterior function of the desired reflectivity coefficients. We then use the HMC technique to find the maximum of the conditional posterior function, thereby obtaining the MAP estimate of the reflectivity coefficients

of the reflectors in the ROI. At the end, we use experimental data gathered from a solid test sample immersed in water to show the better performance of the proposed technique compared to the existing algorithms in the literature.

The chapter is organized as follows. In Section 4.1, we describe our data model. We further cast our problem as a sparse signal representation based problem using multiple measurements. In Section 4.2, we discuss the previous results published in the literature. In Section 4.3, we define the conditional posterior distribution function of the reflectivity coefficients of the hypothetical reflectors in the ROI. In Section 4.4, using the conditional posterior distribution function we obtained in Section 4.3, we address the problem of finding the MAP estimate of the reflectivity coefficients of the hypothetical reflectors using the HMC technique. In Section 4.5, we apply the proposed algorithm to the experimental data gathered from a solid test sample immersed in water. We then compare the result of the proposed algorithm with the existing algorithms in the literature and show the superiority of the proposed algorithm. Finally, conclusions are drawn in Section 5.

4.1 Model description

We consider an array of transducers and a test sample both immersed in water. The geometry of the test setup is shown in Fig. 4.1. Each transducer sends a signal toward the test sample and all transducers record the reflected wave. We consider a 2-dimensional imaging problem in horizontal and vertical directions, shown as x and z, respectively. Furthermore, we assume that our transducers are infinitely long in the third direction. Consequently, each transducer generates a cylindrical wave. Thus, the wave intensity received at point $\hat{\mathbf{r}}_f$, on the surface of the test sample, when

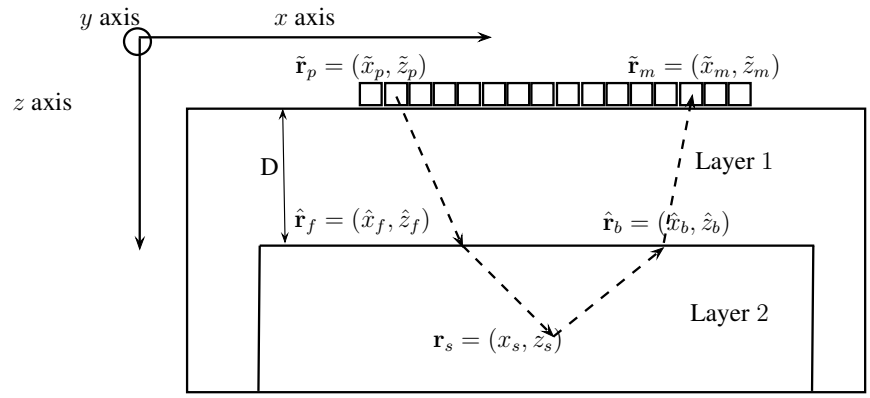

Figure 4.1: The geometry of the array and the test sample.

the p^{th} transducer transmits, is given as

$$g_p(\hat{\mathbf{r}}_f; \omega) = \frac{e^{j\omega\|\tilde{\mathbf{r}}_p - \hat{\mathbf{r}}_f\|/c_1}}{\|\tilde{\mathbf{r}}_p - \hat{\mathbf{r}}_f\|^{0.5}} \tag{4.1}$$

where $\tilde{\mathbf{r}}_p$ is the location of the p^{th} transmitter, $\|\cdot\|$ stands for the Euclidean distance, c_1 is the propagation velocity for the wave in Layer 1 and ω is the angular frequency of the incident wave. The surface of the test sample is modeled as a union of secondary point sources which "illuminate" the ROI. Each secondary source generates a cylindrical wave. According to the Rayleigh-Sommerfeld diffraction formula [94], the wave intensity received at the location of a hypothetical reflector at $\mathbf{r}_l$ inside the solid at the frequency ω is a superposition of all the cylindrical waves generated by the secondary point sources on the interface[1] and is described as

$$\bar{g}_p(\mathbf{r}_l; \omega) = \int_{-\infty}^{+\infty} \frac{T_p(\hat{\mathbf{r}}_f, \mathbf{r}_l)\omega}{j2\pi c_2} g_p(\hat{\mathbf{r}}_f; \omega) \frac{e^{j\omega\|\hat{\mathbf{r}}_f - \mathbf{r}_l\|/c_2}}{\|\hat{\mathbf{r}}_f - \mathbf{r}_l\|^{0.5}} d\hat{x}_f \tag{4.2}$$

where c_2 is the propagation velocity for the wave in the test sample and $T_p(\hat{\mathbf{r}}_f, \mathbf{r}_l)$ is the transmission coefficient for a wave originating from the p^{th} transducer at the point $\hat{\mathbf{r}}_f$ which travels towards the point $\mathbf{r}_l$ inside the test sample and is expressed

[1] We assume that the point reflectors on the interface are infinitely long in the $-y$ direction.

as [94]

$$T_p(\hat{\mathbf{r}}_f, \mathbf{r}_l) = \frac{2c_1 \dfrac{D}{\|\tilde{\mathbf{r}}_p - \hat{\mathbf{r}}_f\|}}{c_1 \dfrac{z_l - D}{\|\hat{\mathbf{r}}_f - \mathbf{r}_l\|} + c_2 \dfrac{D}{\|\tilde{\mathbf{r}}_p - \hat{\mathbf{r}}_f\|}} \tag{4.3}$$

where D is the distance between the array and the surface of the test sample. Furthermore, we can also use the Huygens principle to model each hypothetical reflector as a secondary source. Therefore, each hypothetical reflector, inside the test sample located at $\mathbf{r}_l$, generates a cylindrical wave. Consequently, the wave intensity received at the location of a point on the interface located at $\hat{\mathbf{r}}_b$, at frequency ω, is given as

$$\hat{g}_p(\hat{\mathbf{r}}_b; \omega) = \rho_l \bar{g}_p(\mathbf{r}_l; \omega) \frac{e^{j\omega \|\mathbf{r}_l - \hat{\mathbf{r}}_b\|/c_2}}{\|\mathbf{r}_l - \hat{\mathbf{r}}_b\|^{0.5}} \tag{4.4}$$

where ρ_l is the reflectivity coefficient of the reflector located at $\mathbf{r}_l$. Finally, according to the Rayleigh-Sommerfeld diffraction formula [94], the wave received at the location of the m^{th} receiver, is a superposition of all the cylindrical waves generated by the secondary point sources on the interface, at frequency ω, and is described as

$$\tilde{g}_p(\tilde{\mathbf{r}}_m; \omega) = \int_{-\infty}^{+\infty} \frac{\bar{T}_p(\tilde{\mathbf{r}}_m, \hat{\mathbf{r}}_b, \mathbf{r}_l)\omega}{j2\pi c_1} \hat{g}_p(\hat{\mathbf{r}}_b; \omega) \frac{e^{j\omega \|\hat{\mathbf{r}}_b - \tilde{\mathbf{r}}_m\|/c_1}}{\|\hat{\mathbf{r}}_b - \tilde{\mathbf{r}}_m\|^{0.5}} d\hat{x}_b \triangleq \rho_l a_{pm}(\mathbf{r}_l; \omega) \tag{4.5}$$

where $\tilde{\mathbf{r}}_m$ is the location of the m^{th} receiver and $\bar{T}_p(\tilde{\mathbf{r}}_m, \hat{\mathbf{r}}_b, \mathbf{r}_l)$ is the transmission coefficient for a wave originating from a point reflector located at $\mathbf{r}_l$ inside the test sample which travels towards the m^{th} receiver and is expressed as

$$\bar{T}_p(\tilde{\mathbf{r}}_m, \hat{\mathbf{r}}_b, \mathbf{r}_l) = \frac{2c_1 \dfrac{D}{\|\tilde{\mathbf{r}}_m - \hat{\mathbf{r}}_b\|}}{c_2 \dfrac{z_s - D}{\|\hat{\mathbf{r}}_b - \mathbf{r}_l\|} + c_1 \dfrac{D}{\|\tilde{\mathbf{r}}_m - \hat{\mathbf{r}}_b\|}} \tag{4.6}$$

and $a_{pm}(\mathbf{r}_l;\omega)$ is defined as

$$a_{pm}(\mathbf{r}_l;\omega) \triangleq \left(\int_{-\infty}^{+\infty} \frac{-T_p(\hat{\mathbf{r}}_f,\mathbf{r}_l)\bar{T}_p(\tilde{\mathbf{r}}_m,\hat{\mathbf{r}}_b,\mathbf{r}_l)\omega^2}{4\pi^2 c_1 c_2}\times \frac{e^{j\omega\|\tilde{\mathbf{r}}_p-\hat{\mathbf{r}}_f\|/c_1}}{\|\tilde{\mathbf{r}}_p-\hat{\mathbf{r}}_f\|^{0.5}} \times \frac{e^{j\omega\|\hat{\mathbf{r}}_f-\mathbf{r}_l\|/c_2}}{\|\hat{\mathbf{r}}_f-\mathbf{r}_l\|^{0.5}} d\hat{x}_f\right) \times \left(\int_{-\infty}^{+\infty} \frac{e^{j\omega\|\mathbf{r}_l-\hat{\mathbf{r}}_b\|/c_2}}{\|\mathbf{r}_l-\hat{\mathbf{r}}_b\|^{0.5}} \times \frac{e^{j\omega\|\hat{\mathbf{r}}_b-\tilde{\mathbf{r}}_m\|/c_1}}{\|\hat{\mathbf{r}}_b-\tilde{\mathbf{r}}_m\|^{0.5}} d\hat{x}_b\right). \tag{4.7}$$

We define matrix $\mathbf{A}_p(\omega) \in \mathbb{C}^{M\times L}$ as $\mathbf{A}_p(\omega) \triangleq [\mathbf{a}_p(\mathbf{r}_1;\omega),\ \mathbf{a}_p(\mathbf{r}_2;\omega),\cdots,\mathbf{a}_p(\mathbf{r}_L;\omega)]$, where the vector $\mathbf{a}_p(\mathbf{r}_l;\omega) \in \mathbb{C}^{M\times 1}$ is given as

$$\mathbf{a}_p(\mathbf{r}_l;\omega) = [a_{p1}(\mathbf{r}_l;\omega),\ a_{p2}(\mathbf{r}_l;\omega),\cdots,a_{pM}(\mathbf{r}_l;\omega)]^T. \tag{4.8}$$

In (4.8), $a_{pm}(\mathbf{r}_l;\omega)$ at frequency ω and for the reflector located at $\mathbf{r}_l$ when the p^{th} transducer transmits and the r^{th} transducer receives the wave is given in (4.7) and L is the number of the true reflectors inside the test sample. Consequently, the vector of the signals received by the array, in the presence of the receiver noise, when the p^{th} transducer transmits, is given as

$$\mathbf{y}_p(\omega) = \mathbf{A}_p(\omega)\boldsymbol{\rho} + \mathbf{w}_p(\omega) \tag{4.9}$$

where the vector $\mathbf{y}(\omega) \in \mathbb{C}^{M\times 1}$ is described as $\mathbf{y}_p(\omega) = [y_{p1}(\omega),\ y_{p2}(\omega),\cdots,y_{pM}(\omega)]^T$ in which $y_{pm}(\omega) \in \mathbb{C}$ is the signal received by the m^{th} receiver at the frequency ω when the p^{th} transducer transmits. The l^{th} element of the vector $\boldsymbol{\rho} \in \mathbb{R}^{L\times 1}$ is the reflectivity coefficient of the reflector located at $\mathbf{r}_l$ inside the test sample. The vector $\mathbf{w}_p(\omega) \in \mathbb{C}^{M\times 1}$ is the noise vector and its m^{th} element is the noise for the m^{th} receiver when the p^{th} transducer transmits.

To cast our problem as a sparse signal recovery problem, at each frequency bin, we define $\boldsymbol{\Phi}_p(\omega) \in \mathbb{C}^{M\times N}$ as the dictionary matrix where N represents the number of the potential reflectors. We divide the ROI into $n_x \times n_z = N$ pixels. Each pixel represents

a potential reflector. Fig. 3.2 shows this grid, with n_x pixels in the horizontal direction and n_z pixels in the vertical direction.

The matrix $\mathbf{\Phi}_p(\omega) \in \mathbb{C}^{M\times N}$ is defined as

$$\mathbf{\Phi}_p(\omega) \triangleq [\mathbf{a}_p(\check{\mathbf{r}}_1;\omega)\ \mathbf{a}_p(\check{\mathbf{r}}_2;\omega)\ \cdots\ \mathbf{a}_p(\check{\mathbf{r}}_N;\omega)]. \tag{4.10}$$

In (4.10), $\check{\mathbf{r}}_l$ is the location of the l^{th} potential reflector, $\mathbf{a}_p(\check{\mathbf{r}}_l;\omega) \in \mathbb{C}^{M\times 1}$ is the array steering vector for the lth potential reflector at $\check{\mathbf{r}}_l$ (corresponding to the $(i,j)^{\text{th}}$ pixel in the ROI where $i = \lfloor \frac{l-1}{n_x} \rfloor + 1$ and $j = l - (i-1)n_x$) and it is given in (4.8). Using the dictionary defined in (4.10), the model presented in (4.9) can be rewritten as

$$\mathbf{y}_p(\omega) = \mathbf{\Phi}_p(\omega)\mathbf{s} + \mathbf{w}_p(\omega) \tag{4.11}$$

where the l^{th} element of $\mathbf{s} \in \mathbb{C}^{N\times 1}$ is nonzero if there is a scatterer located at $\check{\mathbf{r}}_l$, corresponding to the $(i,j)^{\text{th}}$ pixel, where $i = \lfloor \frac{l-1}{n_x} \rfloor + 1$ and $j = l - (i-1)n_x$, and it is zero otherwise. Each nonzero element of $\mathbf{s}$ is one of the entries of $\boldsymbol{\rho}$ defined in (4.9). By choosing $N \gg L$ the sparsity of our problem is guaranteed. Our goal is to estimate the vector $\mathbf{s}$ by exploiting its sparse structure.

In order to take the effect of all M measurement vectors into account, we define the vector $\mathbf{y}(\omega) \in \mathbb{C}^{M^2\times 1}$ as

$$\mathbf{y}(\omega) \triangleq [\mathbf{y}_1^T(\omega)\ \mathbf{y}_2^T(\omega)\ \cdots\ \mathbf{y}_M^T(\omega)]^T \tag{4.12}$$

where $\mathbf{y}_p(\omega) \in \mathbb{C}^{M\times 1}$, for $p \in \{1, 2, \cdots, M\}$, is given as in (4.9). We also define a dictionary matrix $\mathbf{\Phi}(\omega) \in \mathbb{C}^{M^2\times N}$ as

$$\mathbf{\Phi}(\omega) = [\mathbf{\Phi}_1^T(\omega)\ \mathbf{\Phi}_2^T(\omega)\ \cdots\ \mathbf{\Phi}_M^T(\omega)]^T \tag{4.13}$$

where each $\mathbf{\Phi}_p(\omega)$, for $p \in \{1, 2, \cdots, M\}$, is given in (4.10). Based on (4.12) and (4.13), the data model for the multiple measurement vector $\mathbf{y}(\omega)$ is given as

$$\mathbf{y}(\omega) = \mathbf{\Phi}(\omega)\mathbf{s} + \mathbf{w}(\omega). \tag{4.14}$$

The noise vector $\mathbf{w}(\omega) \in \mathbb{C}^{M^2 \times 1}$ is defined as $\mathbf{w}(\omega) = [\mathbf{w}_1^T(\omega)\ \mathbf{w}_2^T(\omega)\ \cdots\ \mathbf{w}_M^T(\omega)]^T$. In the next section we address the previous algorithms that have been used either for ultrasonic image reconstruction or for sparse signal recovery.

4.2 Previous Work

In this section we present the works done in the literature based on the data model given in (4.14).

4.2.1 The DAS Beamformer

The image provided by the DAS beamformer, i.e., the estimate of the reflectivity coefficients for a potential reflector located at $\mathbf{r}$, is denoted as $\mathcal{I}_{\text{DAS}}(\mathbf{r};\omega)$ and is given as

$$\mathcal{I}_{\text{DAS}}(\mathbf{r};\omega) = \left| \sum_{p=1}^{M} \sum_{\omega \in \mathbf{\Omega}} \mathbf{a}_p^\dagger(\mathbf{r};\omega)\mathbf{y}_p(\omega) \right|^2 \tag{4.15}$$

where $\mathbf{y}_p(\omega)$ and $\mathbf{a}_p(\mathbf{r};\omega)$ are given as in (4.9) and (4.8), respectively.

4.2.2 MUSIC Based Imaging

The image provided by the MUSIC method is given as [19]

$$\mathcal{I}_{\text{MUSIC}}(\mathbf{r};\omega) = \sum_{\omega \in \mathbf{\Omega}} \frac{\mathbf{a}_p^\dagger(\mathbf{r};\omega)\mathbf{a}_p(\mathbf{r};\omega)}{\mathbf{a}_p^\dagger(\mathbf{r};\omega)\mathbf{E}_n(\omega)\mathbf{E}_n^\dagger(\omega)\mathbf{a}_p(\mathbf{r};\omega)}. \tag{4.16}$$

The L highest peaks of these function give us the location of the L reflectors.

4.2.3 Capon Based Imaging

The Capon image at frequency ω is given as

$$\mathcal{I}_{\text{Capon}}(\mathbf{r};\omega) = \sum_{\omega \in \mathbf{\Omega}} \frac{\mathbf{a}_p^\dagger(\mathbf{r};\omega)\mathbf{a}_p(\mathbf{r};\omega)}{\mathbf{a}_p^\dagger(\mathbf{r};\omega)\hat{\mathbf{R}}_{\text{DL}}^{-1}(\omega)\mathbf{a}_p(\mathbf{r};\omega)}. \tag{4.17}$$

The location of the L highest peaks of the image in (4.17) are introduced as the locations of the L reflectors.

4.2.4 ℓ_1-norm Minimization Based Technique

The ℓ_1-norm optimization problem for (4.14) is expressed as

$$\begin{aligned} \min_{\mathbf{s}} \quad & \|\mathbf{s}\|_1 \\ \text{subject to} \quad & \|\mathbf{y}(\omega) - \mathbf{\Phi}(\omega)\mathbf{s}\|_2 \leq \beta_m \\ & \mathbf{s} \succeq 0, \quad \mathbf{s} \in \mathbb{R}_+^{N\times 1}. \end{aligned} \tag{4.18}$$

4.2.5 Orthogonal Greedy Algorithm

The OGA [27, 32] for the data model given in (4.14) is described as

$$i_k = \arg \max_{1\leq i\leq N} | < \mathbf{r}^{(k-1)}, \Phi^{(i)}(\omega) > | \tag{4.19}$$

where $\Phi^{(i)}(\omega)$ is the i^{th} column of the matrix $\mathbf{\Phi}(\omega)$. The algorithm stops when the ℓ_2-norm of error term falls below a predetermined threshold ξ_g, i.e., $\|\mathbf{y}(\omega) - \hat{\mathbf{y}}^{(k)}(\omega)\|_2 \leq \xi_g$. In signal processing the algorithm given in (4.19) is in fact called OMP.

4.2.6 The FOCUSS Method

The FOCUSS method for the data model given in (4.14), is expressed as

$$\begin{aligned} \min_{\mathbf{s}} \quad & \sum_{i=1}^{N} |s_i|^p \\ \text{subject to} \quad & \|\mathbf{y}(\omega) - \mathbf{\Phi}(\omega)\mathbf{s}\|_2 \leq \beta_f \\ & \mathbf{s} \succeq 0, \quad \mathbf{s} \in \mathbb{R}_+^{N\times 1}. \end{aligned} \tag{4.20}$$

We then use the expectation maximization (EM) algorithm to solve (4.20). To set the stage we first rewrite (4.20) as

$$\min_{\mathbf{s}} \quad \left\{ \|\mathbf{y}(\omega) - \mathbf{\Phi}(\omega)\mathbf{s}\|_2 + \lambda_f \sum_{i=1}^{N} |s_i|^p \right\}, \ \mathbf{s} \in \mathbb{R}_+^{N\times 1} \tag{4.21}$$

which is another equivalent form of (4.20) in which λ_f is a parameter to be tuned. Each generalized Gaussian prior is then expressed as a set of latent variables $\boldsymbol{\gamma} = [\gamma_1, \gamma_2, \cdots, \gamma_N]^T$ which are treated as hidden data. We have given the pseudo-code for the implementation of the FOCUSS method using EM in Algorithm 2 where $\boldsymbol{\Gamma} = \text{diag}(\boldsymbol{\gamma})$. The stopping criterion is based on $\frac{\|\boldsymbol{\gamma} - \boldsymbol{\gamma}_{old}\|_2}{\|\boldsymbol{\gamma}\|_2}$, where $\boldsymbol{\gamma}_{old}$ is the value for $\boldsymbol{\gamma}$ in the last iteration. The algorithm stops when $\frac{\|\boldsymbol{\gamma} - \boldsymbol{\gamma}_{old}\|_2}{\|\boldsymbol{\gamma}\|_2} < \xi_f$.

Algorithm 2 Implementation of the FOCUSS method using EM

*Initialization

Set $\boldsymbol{\gamma} = \mathbf{1}_{N\times 1}$

Set $\boldsymbol{\gamma}_{old} = \mathbf{0}_{N\times 1}$

while $\frac{\|\boldsymbol{\gamma} - \boldsymbol{\gamma}_{old}\|_2}{\|\boldsymbol{\gamma}\|_2} < \xi_f$ **do**

$\boldsymbol{\gamma}_{old} = \boldsymbol{\gamma}$

$\gamma_i = |\hat{s}_i|^{2-p}, \quad i \in \{1, 2, \cdots, N\}.$

$\hat{\mathbf{s}} = \boldsymbol{\Gamma}\boldsymbol{\Phi}(\omega)^\dagger \left(\lambda_f \mathbf{I} + \boldsymbol{\Phi}(\omega)\boldsymbol{\Gamma}\boldsymbol{\Phi}(\omega)^\dagger\right)^{-1} \mathbf{y},$

end while

4.3 Proposed Algorithm

We now present our imaging algorithm (i.e., our algorithm to estimate $\mathbf{s}$) based on Bayesian philosophy. Indeed, our goal is to estimate the vector $\mathbf{s}$, which upon reshaping, yields the image of the ROI. To accomplish this goal, we model the posterior distribution function for $\mathbf{s}$. Once we have the posterior distribution function for $\mathbf{s}$, we then find a realization of $\mathbf{s}$ which maximizes this posterior distribution. Indeed, we are looking for the MAP estimator of $\mathbf{s}$. The l^{th} nonzero element of this realization of $\mathbf{s}$ is the reflectivity coefficient for a reflector located at $\check{\mathbf{r}}_l$.

Our prior information about $\mathbf{s}$ comes from the fact that $\mathbf{s}$ is sparse. Furthermore, from (4.14) we see that the vector $\mathbf{s}$ is real and positive. To enforce sparsity, we model each reflectivity coefficients as a Weibull random variable with a scale parameter which obeys the inverse Gamma distribution. As we will show later, such distribution

for the scale parameter enforces sparsity. Hence, the positivity of the vector $\mathbf{s}$ and ability to build a sparse model are our reason to assign a Weibull distribution function to the vector $\mathbf{s}$. In fact this is one way to enforce sparsity which we have come up with.

We assume that the noise given in (4.14) is Gaussian. Therefore, the likelihood function is also Gaussian. Having the likelihood and the prior distribution function for $\mathbf{s}$, we obtain the posterior function for $\mathbf{s}$. The details are given below.

4.3.1 Prior Distribution for σ^2

Assuming that the elements of $\mathbf{w}(\omega) \in \mathbb{C}^{M^2\times 1}$ are independent identically distributed (i.i.d.) random variables with a Gaussian distribution function, we have

$$\mathbf{w}(\omega)|_{\sigma^2} \sim \mathcal{N}(0, \sigma^2\mathbf{I}) \tag{4.22}$$

where σ^2 is the variance of the noise and $\mathbf{I} \in \mathbb{R}^{M^2\times M^2}$ is the identity matrix. We further assume that the variance of the noise, i.e., σ^2, is a random variable and that the prior distribution for σ^2 is assumed to be inverse Gamma function, i.e., [63, 64]

$$\begin{aligned} p(\sigma^2) &= \frac{d^c}{\Gamma(c)}\sigma^{2(-c-1)}e^{-\frac{d}{\sigma^2}} \\ &= \mathcal{IG}(c,d) \end{aligned} \tag{4.23}$$

where $\Gamma(\cdot)$ is the Gamma function[2] and $\mathcal{IG}(c,d)$ stands for the inverse Gamma distribution[3] function with parameters c and d. We also assume that the i^{th} element of the vector $\mathbf{s}$ conforms to a Weibull distribution, with parameters α and β_i, that is given as

$$p_\alpha(s_i|\beta_i) = \frac{\alpha}{\beta_i}s_i^{\alpha-1}e^{-\frac{s_i^\alpha}{\beta_i}}, \quad s_i \geq 0 \tag{4.24}$$

---

[2] $\Gamma(\varsigma) = \int_0^{+\infty} \xi^{\varsigma-1}e^{-\xi}d\xi.$

[3] $f(x;\mathfrak{a},\mathfrak{b}) = \frac{\mathfrak{b}^{\mathfrak{a}}}{\Gamma(\mathfrak{a})}x^{(-\mathfrak{a}-1)}e^{-\frac{\mathfrak{b}}{x}}.$

where by $p_\alpha(\cdot|\cdot)$, we mean a conditional pdf parameterized by α. The scalar α is called the *shape* parameter and β_i is referred to as the *scaling* parameter. Since $\{s_i\}_{i=0}^N$ are the reflectivity coefficients of the potential reflectors in the ROI, therefore, they are nonnegative real numbers. In fact, $s_i \geq 0$, for $i \in \{1, 2, \cdots, N\}$.

4.3.2 Prior Distribution of s

Using the i.i.d. assumption for the elements of $\mathbf{s}$, the prior conditional distribution function for the vector $\mathbf{s}$ is given as

$$p_\alpha(\mathbf{s}|\boldsymbol{\beta}) = \prod_{i=1}^{N} \frac{\alpha}{\beta_i} s_i^{\alpha-1} e^{-\frac{s_i^\alpha}{\beta_i}} \tag{4.25}$$

where we define $\boldsymbol{\beta} \triangleq [\beta_1 \ \beta_2 \ \cdots \ \beta_N]^T$.

To enforce sparsity, $\boldsymbol{\beta}$ is considered as a random vector with inverse Gamma distribution function with parameters a and b, that is

$$p(\boldsymbol{\beta}) = \prod_{i=1}^{N} \frac{b^a}{\Gamma(a)} \beta_i^{-a-1} e^{\frac{-b}{\beta_i}}. \tag{4.26}$$

The reason for using inverse Gamma distribution function for $\boldsymbol{\beta}$ is that this distribution is conjugate to Weibull distribution function. In fact, using (4.26), the prior distribution function in (4.25) can be written as

$$\begin{aligned} p_\alpha(\mathbf{s}) &= \int_{-\infty}^{+\infty} p(\mathbf{s}|\boldsymbol{\beta}) p(\boldsymbol{\beta}) d\boldsymbol{\beta} \\ &= \prod_{i=1}^{N} \frac{\Gamma(a+1)}{\Gamma(a)} (s_i^\alpha + b)^{a-1} s_i^{\alpha-1} \alpha b^a. \end{aligned} \tag{4.27}$$

Choosing small values for both a and b, we can write $(b + s_i^\alpha)^{a-1} s_i^{\alpha-1} \alpha \simeq \frac{\alpha}{s_i}$, implying that those values of s_i which are zero, will have a relatively higher probability to occur. Consequently, such a prior function will make sparse vectors most probable than the non-sparse vectors. Therefore, this choice for the distribution function of $\boldsymbol{\beta}$ is a good way of enforcing sparsity.

Indeed, we have assumed a Weibull distribution function for each individual element of $\mathbf{s}$. Therefore, if the scaling parameter of the i^{th} element, i.e., β_i, is zero that element will be zero. Here, sparsity of $\mathbf{s}$ is ensured by the sparsity of $\boldsymbol{\beta}$. For those elements of $\mathbf{s}$ that are representing the amplitude of the reflectors, the scale parameter of these elements should be nonzero. Moreover, these nonzero scaling parameters may not be equal. In fact, β_i represents the scaling parameter for s_i and $\{s_i\}_{i=1}^N$ are different and independent of each other. Thus, we consider different scaling parameters for different elements of $\mathbf{s}$ and this is the reason for considering a distinct scaling parameter for each element of $\mathbf{s}$. Regarding the shape parameter α, however, we have assumed the same parameter for all the elements. Since we do not have any prior information about α, we estimate this parameter. The following lemma allows us to estimate α based on the second-kind cumulant of the elements of $\mathbf{s}$:

Lemma 1: Let the vector $\mathbf{s}$ with i.i.d. elements have the Weibull distribution given as in (4.25). Then the parameter α can be described as

$$\alpha = \sqrt{\frac{\pi^2}{6\kappa_2}} \tag{4.28}$$

where κ_2 is the 2^{nd}order second-kind cumulant of $\mathbf{s}$ which is given as

$$\kappa_2 = E(\ln(s_i) - E(\ln(s_i)))^2. \tag{4.29}$$

Proof: See Appendix 4.7.1.

Since $\mathbf{s}$ is a vector of i.i.d. random variables, therefore it is ergodic. Hence, any moment of $\mathbf{s}$ can be consistently estimated as the corresponding sample moment. More specifically an estimation of (4.29) is given as

$$\hat{\kappa}_2 = \frac{1}{N-1}\sum_{i=1}^{N}(\ln(s_i) - \hat{\kappa}_1)^2 \tag{4.30}$$

where $\hat{\kappa}_1$ is expressed as

$$\hat{\kappa}_1 = \frac{1}{N}\sum_{i=1}^{N}\ln(s_i). \tag{4.31}$$

Consequently, using (4.30) and (4.31), an estimate of α is given as

$$\hat{\alpha} = \sqrt{\frac{\pi^2}{6\hat{\kappa}_2}}. \tag{4.32}$$

From now on, for simplicity of notation, we use α instead of $\hat{\alpha}$.

4.3.3 Joint Posterior Distribution Function

Having estimated α as in (4.32), the joint posterior distribution function for $(\mathbf{s}, \boldsymbol{\beta}, \sigma^2)$ is expressed as

$$p_\alpha(\mathbf{s}, \boldsymbol{\beta}, \sigma^2|\mathbf{y}(\omega)) = \frac{p(\mathbf{y}(\omega)|\mathbf{s}, \sigma^2)\; p_\alpha(\mathbf{s}|\boldsymbol{\beta})\; p(\boldsymbol{\beta})\; p(\sigma^2)}{p(\mathbf{y}(\omega))}. \tag{4.33}$$

Here, $p(\mathbf{y}(\omega)|\mathbf{s}, \sigma^2)$ is the likelihood function which is described as

$$p(\mathbf{y}(\omega)|\mathbf{s}, \sigma^2) = \frac{1}{(2\pi\sigma^2)^{M^2/2}} e^{-\dfrac{\|\mathbf{y}(\omega) - \boldsymbol{\Phi}(\omega)\tilde{\mathbf{s}}\|_2^2}{2\sigma^2}}. \tag{4.34}$$

Substituting (4.25), (4.26) and (4.34) into (4.33), we obtain the joint posterior pdf for $\mathbf{s}$, $\boldsymbol{\beta}$ and σ^2 as

$$\begin{aligned} p_\alpha(\mathbf{s}, \boldsymbol{\beta}, \sigma^2|\mathbf{y}(\omega)) = \; & \frac{1}{p(\mathbf{y}(\omega))} \frac{1}{(2\pi\sigma^2)^{M^2/2}} e^{-\dfrac{\|\mathbf{y}(\omega) - \boldsymbol{\Phi}(\omega)\mathbf{s}\|_2^2}{2\sigma^2}} \times \\ & \left(\prod_{j=1}^{N} \frac{\alpha}{\beta_i} s_i^{\alpha-1} e^{-\frac{s_i^\alpha}{\beta_i}} \right) \times \\ & \left(\prod_{i=1}^{N} \frac{b^a}{\Gamma(a)} \beta_i^{-a-1} e^{-\frac{b}{\beta_i}} \right) \times \frac{d^c}{\Gamma(c)} \sigma^{2(-c-1)} e^{-\frac{d}{\sigma^2}}. \end{aligned} \tag{4.35}$$

We resort to MAP approach to find the MAP estimate for $\mathbf{s}$, $\boldsymbol{\beta}$ and σ^2. To this end, we have to solve the following optimization problem:

$$\max_{\mathbf{s}} \{ \max_{\boldsymbol{\beta}, \sigma^2} \; p_\alpha(\mathbf{s}, \boldsymbol{\beta}, \sigma^2|\mathbf{y}(\omega)) \}. \tag{4.36}$$

To solve (4.36), we rewrite the joint posterior distribution function $p_\alpha(\mathbf{s}, \boldsymbol{\beta}, \sigma^2|\mathbf{y}(\omega))$, given in (4.35), as

$$p_\alpha(\mathbf{s}, \boldsymbol{\beta}, \sigma^2|\mathbf{y}(\omega)) = p_\alpha(\boldsymbol{\beta}|\mathbf{s}, \sigma^2, \mathbf{y}(\omega)) p_\alpha(\mathbf{s}, \sigma^2|\mathbf{y}(\omega)). \tag{4.37}$$

Since given $\mathbf{s}$, the vector $\boldsymbol{\beta}$ is independent of $\mathbf{y}(\omega)$ and σ^2, therefore, the first term on the right hand side of (4.37) can be written as $p_\alpha(\boldsymbol{\beta}|\mathbf{s},\sigma^2,\mathbf{y}(\omega)) = p_\alpha(\boldsymbol{\beta}|\mathbf{s})$. Consequently, we can rewrite (4.37) as

$$p_\alpha(\mathbf{s},\boldsymbol{\beta},\sigma^2|\mathbf{y}(\omega)) = p_\alpha(\boldsymbol{\beta}|\mathbf{s}) \times p_\alpha(\mathbf{s},\sigma^2|\mathbf{y}(\omega)). \tag{4.38}$$

In (4.38), the term $p_\alpha(\boldsymbol{\beta}|\mathbf{s})$ is independent of σ^2 and the term $p_\alpha(\mathbf{s},\sigma^2|\mathbf{y}(\omega))$ is independent of $\boldsymbol{\beta}$. Therefore, using (4.38), the optimization problem given in (4.36) is modified as

$$\max_{\mathbf{s}} \left(\{\max_{\boldsymbol{\beta}} \; p_\alpha(\boldsymbol{\beta}|\mathbf{s})\} \times \{\max_{\sigma^2} \; p_\alpha(\mathbf{s},\sigma^2|\mathbf{y}(\omega))\} \right). \tag{4.39}$$

To solve (4.39), we start with $\{\max_{\boldsymbol{\beta}} \; p_\alpha(\boldsymbol{\beta}|\mathbf{s})\}$. The function $p_\alpha(\boldsymbol{\beta}|\mathbf{s})$ is expressed as

$$\begin{aligned} p_\alpha(\boldsymbol{\beta}|\mathbf{s}) &= p_\alpha(\mathbf{s}|\boldsymbol{\beta})p(\boldsymbol{\beta}) \\ &= \prod_{i=1}^{N} \frac{\alpha}{\beta_i} s_i^{\alpha-1} e^{-\frac{s_i^\alpha}{\beta_i}} \times \beta_i^{-a-1} e^{\frac{-b}{\beta_i}} \\ &\propto \prod_{i=1}^{N} \mathcal{IG}(a+\frac{1}{\alpha}, s_i^\alpha + b) \end{aligned} \tag{4.40}$$

which is an inverse Gamma distribution function. Since the maximum of an inverse Gamma function with parameters $\mathfrak{a}$ and $\mathfrak{b}$ is $\dfrac{\mathfrak{b}}{\mathfrak{a}+\mathfrak{1}}$, the maximum of $p_\alpha(\boldsymbol{\beta}|\mathbf{s})$ with respect to $\boldsymbol{\beta}$, which is the MAP estimator for $\boldsymbol{\beta}$, for given $\mathbf{s}$, is expressed as[4]

$$\beta_i = \frac{s_i^\alpha + b}{a + 1 + 1/\alpha}. \tag{4.41}$$

The other maximization in (4.39) is $\{\max_{\sigma^2} \; p_\alpha(\mathbf{s},\sigma^2|\mathbf{y}(\omega))\}$. The function $p_\alpha(\mathbf{s},\sigma^2|\mathbf{y}(\omega))$ is described as

$$p_\alpha(\mathbf{s},\sigma^2|\mathbf{y}(\omega)) = p_\alpha(\sigma^2|\mathbf{s},\mathbf{y}(\omega))p_\alpha(\mathbf{s}|\mathbf{y}(\omega)). \tag{4.42}$$

Based on (4.42), for given $\mathbf{s}$, the only term that depends on σ^2 is $p_\alpha(\sigma^2|\mathbf{s},\mathbf{y}(\omega))$. Therefore, the MAP estimator for σ^2 is expressed as

$$\hat{\sigma^2} = \arg\max_{\sigma^2} \; p_\alpha(\sigma^2|\mathbf{s},\mathbf{y}(\omega)). \tag{4.43}$$

[4]From now on, with a slight abuse of notation, we use β_i instead of $\hat{\beta}_i$ for simplicity.

The conditional distribution $p_\alpha(\sigma^2|\mathbf{s}, \mathbf{y}(\omega))$ is described as

$$\begin{aligned} p_\alpha(\sigma^2|\mathbf{s}, \mathbf{y}(\omega)) &= \frac{p_\alpha(\mathbf{y}(\omega)|\mathbf{s}, \sigma^2)p_\alpha(\sigma^2|\mathbf{s})}{p_\alpha(\mathbf{y}(\omega)|\mathbf{s})} \\ &= \frac{p_\alpha(\mathbf{y}(\omega)|\mathbf{s}, \sigma^2)p(\sigma^2)}{p_\alpha(\mathbf{y}(\omega)|\mathbf{s})} \end{aligned} \tag{4.44}$$

where we have used the assumption that $\mathbf{s}$ and σ^2 are statistically independent. From (4.44), we see that the denominator is independent of σ^2. Therefore, to obtain the MAP estimate of σ^2, we maximize the following expression with respect to σ^2

$$\begin{aligned} p_\alpha(\sigma^2|\mathbf{s}, \mathbf{y}(\omega)) &\propto p_\alpha(\mathbf{y}(\omega)|\mathbf{s}, \sigma^2)p(\sigma^2) \\ &= \frac{1}{(2\pi\sigma^2)^{M^2/2}} e^{-\frac{\|\mathbf{y}(\omega) - \mathbf{\Phi}(\omega)\mathbf{s}\|_2^2}{2\sigma^2}} \frac{d^c}{\Gamma(c)} \sigma^{2(-c-1)} e^{-\frac{d}{\sigma^2}} \\ &\propto \mathcal{IG}(c + M^2/2, \frac{\|\mathbf{y}(\omega) - \mathbf{\Phi}(\omega)\mathbf{s}\|_2^2 + 2d}{2}). \end{aligned} \tag{4.45}$$

By maximizing (4.45) with respect to σ^2, we find the MAP estimator for σ^2, given $\mathbf{s}$, and the result is given as[5]

$$\sigma^2 = \frac{d + \frac{\|\mathbf{y}(\omega) - \mathbf{\Phi}(\omega)\mathbf{s}\|_2^2}{2}}{(c + M^2/2)}. \tag{4.46}$$

Having obtained the MAP estimator of $\boldsymbol{\beta}$ and σ^2, given in (4.41) and (4.46) respectively, we are left with maximization over $\mathbf{s}$ in (4.39). To solve this last maximization, we rewrite the objective function in the initial optimization problem, given in (4.36), as

$$p_\alpha(\mathbf{s}, \boldsymbol{\beta}, \sigma^2|\mathbf{y}(\omega)) = p_\alpha(\mathbf{s}|\boldsymbol{\beta}, \mathbf{y}(\omega), \sigma^2)p_\alpha(\boldsymbol{\beta}, \sigma^2|\mathbf{y}(\omega)). \tag{4.47}$$

The only term which depends on $\mathbf{s}$ in (4.47) is $p_\alpha(\mathbf{s}|\boldsymbol{\beta}, \mathbf{y}(\omega), \sigma^2)$. Therefore, the MAP estimator for $\mathbf{s}$ is expressed as

$$\hat{\mathbf{s}} = \arg\max_{\mathbf{s}} \; p_\alpha(\mathbf{s}|\mathbf{y}(\omega), \boldsymbol{\beta}, \sigma^2). \tag{4.48}$$

[5]From now on, with a slight abuse of notation, we use σ^2 instead of $\hat{\sigma^2}$ for simplicity.

The conditional distribution $p_\alpha(\mathbf{s}|\mathbf{y}(\omega), \boldsymbol{\beta}, \sigma^2)$ in (4.48) can be written as

$$p_\alpha(\mathbf{s}|\mathbf{y}(\omega), \boldsymbol{\beta}, \sigma^2) = \frac{p_\alpha(\mathbf{y}(\omega)|\mathbf{s}, \boldsymbol{\beta}, \sigma^2) p_\alpha(\mathbf{s}|\boldsymbol{\beta}, \sigma^2)}{p_\alpha(\mathbf{y}(\omega)|\boldsymbol{\beta}, \sigma^2)}. \tag{4.49}$$

The denominator in (4.49) does not depend on $\mathbf{s}$. Therefore, we can maximize the following expression

$$p_\alpha(\mathbf{s}|\mathbf{y}(\omega), \boldsymbol{\beta}, \sigma^2) \propto p_\alpha(\mathbf{y}(\omega)|\mathbf{s}, \sigma^2) p_\alpha(\mathbf{s}|\boldsymbol{\beta}, \sigma^2). \tag{4.50}$$

Using the expression given in (4.34) for the likelihood function and (4.25) for the prior distribution function of $\mathbf{s}$, the conditional posterior function given in (4.50) can be described as

$$p_\alpha(\mathbf{s}|\mathbf{y}(\omega), \boldsymbol{\beta}, \sigma^2) \propto \frac{1}{(2\pi\sigma^2)^{M^2/2}} e^{-\frac{\|\mathbf{y}(\omega) - \boldsymbol{\Phi}(\omega)\mathbf{s}\|_2^2}{2\sigma^2}} \times \prod_{i=1}^{N} \frac{\alpha}{\beta_i} s_i^{\alpha-1} e^{-\frac{s_i^\alpha}{\beta_i}}. \tag{4.51}$$

Using (4.41) and (4.46), for estimates of $\boldsymbol{\beta}$ and σ^2 respectively, in (4.51), we obtain

$$\begin{aligned} p_\alpha(\mathbf{s}|\mathbf{y}(\omega), \boldsymbol{\beta}, \sigma^2) \propto & \frac{e^{-\frac{\|\mathbf{y}(\omega) - \boldsymbol{\Phi}(\omega)\mathbf{s}\|_2^2}{2(d + \|\mathbf{y}(\omega) - \boldsymbol{\Phi}(\omega)\mathbf{s}\|_2^2/2)/(c+1+M^2/2)}}}{(2\pi(2d + \|\mathbf{y}(\omega) - \boldsymbol{\Phi}(\omega)\mathbf{s}\|_2^2)/(c+1+M^2/2))^{M^2/2}} \\ & \times \prod_{i=1}^{N} \frac{\alpha s_i^{\alpha-1} e^{-\frac{s_i^\alpha}{(s_i^\alpha + b)/(a+1+1/\alpha)}}}{(s_i^\alpha + b)/(a+1+1/\alpha)}. \end{aligned} \tag{4.52}$$

Therefore, our aim is to maximize the conditional distribution function $p_\alpha(\mathbf{s}|\mathbf{y}(\omega), \boldsymbol{\beta}, \sigma^2)$ given in (4.52) with respect to $\mathbf{s}$. However, $p_\alpha(\mathbf{s}|\mathbf{y}(\omega), \boldsymbol{\beta}, \sigma^2)$ is not concave. Therefore, any gradient based technique may trap in a local maximum. Thus, our aim is not to find the maximum of $p_\alpha(\mathbf{s}|\mathbf{y}(\omega), \boldsymbol{\beta}, \sigma^2)$ directly. Instead, we consider the conditional posterior function $p_\alpha(\mathbf{s}|\mathbf{y}(\omega), \boldsymbol{\beta}, \sigma^2)$ as a pdf. Then we try to find different realizations of $\mathbf{s}$ based on this pdf. The MAP estimator can then be approximated by evaluating the target distribution, i.e, $p_\alpha(\mathbf{s}|\mathbf{y}(\omega), \boldsymbol{\beta}, \sigma^2)$ given in (4.52), with the generated $\mathbf{s}$. The $\mathbf{s}$ which provides the highest score will be the desired result.

Among the well known techniques for finding realizations of a complicated distribution functions such as the pdf in (4.52), we can name MCMC method and Gibs sampler [48, 49]. However, since $p_\alpha(\mathbf{s}|\mathbf{y}(\omega), \boldsymbol{\beta}, \sigma^2)$ has local maxima, generating random-walk in MCMC method, which is the main part of this technique, is pron to error. Moreover, because of the curse of dimensionality, both MCMC method and Gibs sampler turn out to be computationally inefficient [48–50]. We overcome these difficulties by utilizing the HMC technique. The HMC technique is a combination of Hamiltonian Monte Carlo and MCMC method [48–50].

In the next section, we address the implementation of the HMC technique.

4.4 Hybrid Monte Carlo Implementation

To implement the HMC method [48–50], we define an auxiliary vector $\mathbf{u} \in \mathbb{C}^{N\times 1}$ independent of $\mathbf{s}$. Then, we define the following function

$$K(\mathbf{u}) = \frac{1}{2}\mathbf{u}^T\mathbf{u}. \tag{4.53}$$

A common choice for the pdf of $\mathbf{u}$ is a Gaussian distribution with zero mean and unit variance. Using the analogy from physics, we obtain the Hamiltonian which is expressed as

$$\mathcal{H}(\mathbf{s}, \mathbf{u}) = U(\mathbf{s}) + K(\mathbf{u}) \tag{4.54}$$

where $U(\mathbf{s})$ is defined as

$$U(\mathbf{s}) \triangleq -\ln(p_\alpha(\mathbf{s}|\mathbf{y}(\omega), \boldsymbol{\beta}, \sigma^2)). \tag{4.55}$$

Using the expression given in (4.52) for $p_\alpha(\mathbf{s}|\mathbf{y}(\omega), \boldsymbol{\beta}, \sigma^2)$ in (4.55), function $U(\mathbf{s})$ is expressed as

$$\begin{aligned} U(\mathbf{s}) = & \frac{\|\mathbf{y}(\omega) - \boldsymbol{\Phi}(\omega)\mathbf{s}\|_2^2}{(2d + \|\mathbf{y}(\omega) - \boldsymbol{\Phi}(\omega)\mathbf{s}\|_2^2)/(c + 1 + M^2/2)} \\ & + \frac{M^2}{2} \ln(2\pi(2d + \|\mathbf{y}(\omega) - \boldsymbol{\Phi}(\omega)\mathbf{s}\|_2^2)/(c + 1 + M^2/2)) \\ & - N \ln(\alpha) - (\alpha - 1) \sum_{i=1}^{N} s_i + \sum_{i=1}^{N} \frac{s_i^\alpha}{(s_i^\alpha + b)/(a + 1 + 1/\alpha)} \\ & + \sum_{i=1}^{N} \ln\left(\frac{s_i^\alpha + b}{a + 1 + 1/\alpha}\right). \end{aligned} \tag{4.56}$$

By borrowing analogy from physics, $U(\mathbf{s})$ plays the role of the potential energy and $K(\mathbf{u})$ plays the role of the kinetic energy. In fact, $\mathbf{u}$ is an auxiliary variable which by analogy from classical mechanic plays the role of the momentum of a point particle and subsequently $\mathbf{s}$ describes the location of this point particle. However, estimating $\mathbf{u}$ is not the goal of the HMC method, but $\mathbf{u}$ is being updated in the HMC method along side $\mathbf{s}$ and this helps with the estimation of $\mathbf{s}$ which is the desired vector.

To implement the HMC we utilize the so called leapfrog equations described as [48–50]

$$\begin{aligned} \mathfrak{u} &= \mathbf{u}_{j-1} - \tfrac{\epsilon}{2} \nabla U(\mathbf{s}) \mid_{\mathbf{s}=\mathbf{s}_{j-1}} \\ \mathbf{s}_j &= \mathbf{s}_{j-1} + \epsilon \mathfrak{u} \\ \mathbf{u}_j &= \mathfrak{u} - \tfrac{\epsilon}{2} \nabla U(\mathbf{s}) \mid_{\mathbf{s}=\mathbf{s}_j} \end{aligned} \tag{4.57}$$

where the vector $\mathfrak{u} \in \mathbb{C}^{N \times 1}$ is an auxiliary variable and $\nabla U(\mathbf{s})$ is the gradient of $U(\mathbf{s})$ that we calculate later. To explain (4.57), let $(\mathbf{s}^{(t-1)}, \mathbf{u}^{(t-1)})$ be the state of the Hamiltonian at the $t-1$ step. Then we set $(\mathbf{s}_0, \mathbf{u}_0) = (\mathbf{s}^{(t-1)}, \mathbf{u}^{(t-1)})$ and run (4.57) for $\tilde{L}$ times. At the end we obtain $(\mathbf{s}_{\tilde{L}}, \mathbf{u}_{\tilde{L}})$ and we have to decide wether we should accept this new value, meaning $(\mathbf{s}^{(t)}, \mathbf{u}^{(t)}) = (\mathbf{s}_{\tilde{L}}, \mathbf{u}_{\tilde{L}})$, or remain at the previous value, meaning $(\mathbf{s}^{(t)}, \mathbf{u}^{(t)}) = (\mathbf{s}^{(t-1)}, \mathbf{u}^{(t-1)})$. The decision making procedure is based on the

Metropolis-Hastings technique in which we calculate the following parameter

$$\lambda = \min\{1, \frac{e^{\mathcal{H}(\mathbf{s}^{(t-1)}, \mathbf{u}^{(t-1)})}}{e^{\mathcal{H}(\mathbf{s}_{\tilde{L}}, \mathbf{u}_{\tilde{L}})}}\} \tag{4.58}$$

then with probability λ, we accept the new values.

We have described our proposed method in Algorithm 3. Each column of the matrix $\mathbf{X} \in \mathbb{R}^{N\times T}$ stores an estimate of $\mathbf{s}$ at each iteration. The number of the columns of the matrix $\mathbf{X}$, i.e., T, is in fact the number of different realizations that we generate for $\mathbf{s}$. At the end, the MAP estimate for $\mathbf{s}$ is a column of the matrix $\mathbf{X}$ with highest score.

For the implementation of (4.57) we need the gradient of $U(\mathbf{s})$. The gradient of $U(\mathbf{s})$, given in (4.56), is described as

$$\begin{aligned}\nabla U(\mathbf{s}) = \; & 4d(c+1+M^2/2)\frac{\mathbf{\Phi}(\omega)^\dagger(\mathbf{y}(\omega)-\mathbf{\Phi}(\omega)\mathbf{s})}{\left(2d+\|\mathbf{y}(\omega)-\mathbf{\Phi}(\omega)\mathbf{s}\|_2^2\right)^2} \\ & -M^2\frac{\mathbf{\Phi}(\omega)^\dagger(\mathbf{y}(\omega)-\mathbf{\Phi}(\omega)\mathbf{s})}{2d+\|\mathbf{y}(\omega)-\mathbf{\Phi}(\omega)\mathbf{s}\|_2^2} + \boldsymbol{\vartheta}.\end{aligned} \tag{4.59}$$

In (4.59), the i^{th} element of the vector $\boldsymbol{\vartheta} \in \mathbb{C}^{N\times 1}$ is given as

$$\begin{aligned}\vartheta_i = \; & -N\frac{d\alpha/ds_i}{\alpha} - (\alpha-1) - (d\alpha/ds_i)\sum_{i=1}^{N} s_i \\ & + \frac{\frac{-d\alpha/ds_i}{\alpha^2}}{1+b/s_i^\alpha} + \frac{b(a+1+1/\alpha)ds_i^\alpha/ds_i}{\left(b+s_i^\alpha\right)^2} \\ & + \frac{ds_i^\alpha/ds_i}{s_i^\alpha+b} - \frac{\frac{-d\alpha/ds_i}{\alpha^2}}{a+1+1/\alpha}\end{aligned} \tag{4.60}$$

where ds_i^α/ds_i is given as

$$\frac{ds_i^\alpha}{ds_i} = \left(\frac{d\alpha}{ds_i}\ln s_i + \frac{\alpha}{s_i}\right)s_i^\alpha \tag{4.61}$$

To calculate $d\alpha/ds_i$, we rewrite the expression for α given in (4.32) as

$$\hat{\alpha} = \sqrt{\frac{\pi^2(N-1)}{6\sum_{i=1}^{N}[\ln(s_i) - \frac{1}{N}\sum_{i=1}^{N}\ln(s_i)]^2}} \tag{4.62}$$

where we have used the expressions (4.30) and (4.31) in (4.32). Using (4.62), $d\alpha/ds_i$ is given as

$$\begin{aligned} d\alpha/ds_i = \; & -\sqrt{\frac{\pi^2(\tilde{N}-1)}{6}}\left(\sum_{i=1}^{N}\left(\ln(s_i)-\frac{1}{N}\sum_{i=1}^{N}\ln(s_i)\right)^2\right)^{\frac{-3}{2}} \\ & \times\left(\sum_{i=1}^{N}\left(\ln(s_i)-\frac{1}{N}\sum_{i=1}^{N}\ln(s_i)\right)\right) \\ & \times\left(\sum_{i=1}^{N}\left(\frac{1}{s_i}-\frac{1}{N}\sum_{i=1}^{N}\frac{1}{s_i}\right)\right). \end{aligned} \tag{4.63}$$

Algorithm 3 Proposed Method

*Initialization

Generate an initial value for $\mathbf{s}^{(0)} \sim \mathcal{N}(\mathbf{0}_{N\times 1}, \mathbf{I}_{N\times N})$

Generate an initial value for $\mathbf{u}^{(0)} \sim \mathcal{N}(\mathbf{0}_{N\times 1}, \mathbf{I}_{N\times N})$

for $i = 1$ to T **do**

$(\mathbf{s}_0, \mathbf{u}_0) = (\mathbf{s}^{(i-1)}, \mathbf{u}^{(i-1)})$

Estimation of α based on (4.32)

for $j = 2$ to $\tilde{L}$ **do**

$\mathfrak{u} = \mathbf{u}_{j-1} - \frac{\epsilon}{2}\nabla U(\mathbf{s}) \mid_{\mathbf{s}=\mathbf{s}_{j-1}}$

$\mathbf{s}_j = \mathbf{s}_{j-1} + \epsilon\mathfrak{u}$

$\mathbf{u}_j = \mathfrak{u} - \frac{\epsilon}{2}\nabla U(\mathbf{s}) \mid_{\mathbf{s}=\mathbf{s}_j}$

end for

$(\hat{\mathbf{s}}, \hat{\mathbf{u}}) = (\mathbf{s}_{\tilde{L}}, \mathbf{u}_{\tilde{L}})$

Metropolis-Hastings decision making criteria

$u \sim \mathcal{U}[0,1]$

$\lambda = min\{1, \frac{e^{\mathcal{H}(\mathbf{s}^{(i-1)}, \mathbf{u}^{(i-1)})}}{e^{\mathcal{H}(\hat{\mathbf{s}}, \hat{\mathbf{u}})}}\}$

if $u < min(1, \lambda)$ **then**

$\mathbf{s}^{(i)} = \hat{\mathbf{s}}$, $\mathbf{u}^{(i)} = \hat{\mathbf{u}}$

else

$\mathbf{s}^{(i)} = \mathbf{s}^{(i-1)}$, generate $\mathbf{u}^{(i)} \sim \mathcal{N}(\mathbf{0}_{N\times 1}, \mathbf{I}_{N\times N})$

end if

$\mathbf{X}(:, i) = \mathbf{s}^{(i)}$

end for

$\hat{\mathbf{s}}$ is a column of the matrix $\mathbf{X}$ with highest score.

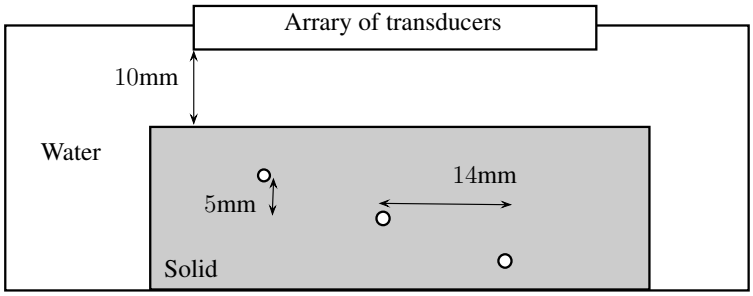

Figure 4.2: Test setup geometry.

4.5 Experimental results

In this section we apply the proposed technique described in Algorithm 3, along with the DAS beamformer given in (4.15), the MUSIC method described by (4.16), the Capon technique using (4.17), the ℓ_1-norm minimization based technique given in (4.18), the OMP based on (4.19) and the FOCUSS technique based on Algorithm 2 to the experimental data gathered from a specimen immersed in water. Then we generate the corresponding images and discuss the results.

The test setup has been shown in Fig. 4.2. A solid test sample with three holes has been immersed in water. The depth of the water above the test sample is 10 mm. The horizontal and vertical distances between the holes are 14 mm and 5 mm, respectively. The distance of the first hole inside the test sample from the surface of the test sample is 8 mm. The specifications for the array have been summarized in Table 4.1.

We use FFT to map our data into frequency domain. The width of each frequency bin is 83.34 KHz. The energy of the probing signal has occupied 60 bins from 2.5 MHz to 7.5 MHz. Therefore, the frequency bins out of this range belong to noise.

To check that our assumptions about the receiver noise are correct we estimate the pdf of the noise. To do that, we use the output of FFT at frequency 20 MHz. Fig. 4.3-

Table 4.1: Array parameters specification.

Array parameters	Value
Element type	rectangular
Number of elements	64
Element Pitch	0.6 mm
Element width	0.53 mm
Element length	0.012 m
Center Frequency	5 MHz
Sampling frequency	100 MHz
Bandwith	5MHz
Speed of wave in water	1482 m/s
Speed of wave in solid	6400 m/s

(a) shows the estimated pdf of the real part of the noise. To generate Fig. 4.3-(a), we have taken the real part of the signal, received at each receiver, as an independent realization of the real part of the noise. In fact, since at frequency 20 MHz the signal, received at each receiver, contains only the energy of the noise, therefore, we have indeed obtained the real part of the noise at each receiver. Furthermore, since all the receivers are the same, we can take the real part of the noise at each receiver as an independent realization. Consequently, we have 64 different realizations of the real part of the noise that upon averaging them we obtain Fig. 4.3-(a). As can be seen from Fig. 4.3-(a), Gaussian pdf fits the real part of the noise perfectly.

Moreover, Fig. 4.3-(b) shows the estimated pdf for the variance of the noise along with the inverse Gamma pdf based on the noise specifications. To obtain Fig. 4.3-(b), we have calculated the variance of the signal, received at each receiver, at frequency 20 MHz. Since at frequency 20 MHz the signal contains only the energy of the noise, therefore, we have indeed calculated the variance of the noise at each receiver. Furthermore, since all the receivers are the same, we can take the calculated variance at each receiver as an independent realization of the variance of the noise. Therefore, we have 64 different realizations of the noise which upon averaging them we obtain Fig. 4.3-(b).

Fig. 4.3-(b) shows clearly that the inverse Gamma distribution function models the variance of the noise precisely. Therefore, from Fig. 4.3-(a) and Fig. 4.3-(b) we realize that our assumptions about the distribution function of the noise and its variance are valid.

To obtain the image of the test sample, we set the size of ROI to $n_x = 100$ and $n_z = 100$. Therefore, the size of the vector $\mathbf{s}$ is $N = n_x \times n_z = 10000$. The length of the measurement vector, i.e., $\mathbf{y}(\omega)$, is $M^2 = 4096$. Hence one of the conditions that we need for sparse signal recovery which is $N > M^2$ is satisfied.

For our proposed technique based on Algorithm 3, the parameters a and b for

(4.26) have been set to 10^{-8}. The parameters c and d for (4.23) have been set to 10^{-4}. We have set $\tilde{L}$ and ϵ to 100 and 6.5×10^{-4}, respectively. The value for T has been set 150. The parameters $\tilde{L}$ and ϵ are obtained by cross validation. We use the frequency bin corresponding to the center frequency of the probing signal which is 5 MHz.

The 2-dimensional image based on Algorithm 3 has been shown in Fig. 4.4-(a). The estimated value for the shape parameter, α, is 1.8761.

Fig. 4.4-(b) shows the result of applying the OMP technique given in (4.19). The frequency bin corresponding to the center frequency of the probing signal, which is 5 MHz has been used. The parameter ξ_g has been set to 10^{-4}. From Fig. 4.4-(b) we see clearly that the OMP fails to reconstruct the whole three targets. The value for mutual incoherence is $\mu = 0.99$. Therefore, using the fact that $L = 3$, we find that $\mu < \frac{1}{2L-1}$ does not hold true. Hence there is no guarantee that OMP recovers exactly the true support of $\mathbf{s}$ and Fig. 4.4-(b) shows this clearly.

The image based on ℓ_1-norm minimization problem given in (4.18), for $p = 1$, has been shown in Fig. 4.4-(c), in which we have used the frequency bin corresponding to the center frequency of the probing signal, which is 5 MHz, and we have set $\beta_m = 1.58$. We have used the CVX software package to implement (4.18). The CVX software package casts the ℓ_1-norm minimization problem as a linear programming and the cost of implementation is $O(N^3)$.

For the FOCUSS method we use Algorithm 2. In Fig. 4.4-(d) we have shown the result of the implementation of the FOCUSS method for $p = 0.001$. We have used the energy of the signal corresponding to the center frequency which is 5 MHz.

For the MAP estimation based on Laplacian prior we have used the FOCUSS method for $p = 1$ at $f = 5$ MHz and the result has been shown in Fig. 4.5-(a). As we mentioned before the FOCUSS technique for $p = 1$ reduces to the MAP estimator based on Laplacian prior.

For the DAS beamformer (4.15), the MUSIC method (4.16) and the Capon technique (4.17), the total number of 60 bins are used which covers the whole 5 MHz bandwidth of our probing signal from 2.5 MHz to 7.5 MHz. Figs. 4.5-(b)-(c)-(d) show the 2-dimensional images for the MUSIC method, the Capon technique and the DAS beamformer, respectively. The size of the signal subspace for the MUSIC technique has been set to 3 and for the Capon technique we have set κ to 2000.

The poor results for both the MUSIC technique and the Capon method is partly due to relatively low number of snapshots as only 64 snapshots are not sufficient to obtain a good estimate of the covariance matrix given in (3.11). As to the Capon method, the other issue is the parameter κ. Since the Capon technique is sensitive to κ and since there is only a rule of thumb for choosing κ, which says κ should be 10 to 12 dB above the noise level, therefore the performance of the Capon method changes by κ and the value 2000 is the best value that we have been able to choose for κ to yield the image in Figs. 4.5-(c).

In Fig. 4.6, we show the root mean squared error (RMSE) curves versus SNR for all the methods. To achieve Fig. 4.6, we have used the same experimental data that we have used so far. We have added noise to the data. In each step a Monte Carlo with 50 runs has been performed. From Fig. 4.6, it is clear that our proposed algorithm based on Algorithm 3 has better performance. Since the OMP has failed to recover the whole number of reflectors therefore, we have excluded it from RMSE analysis.

We have already discussed the superiority of the sparse signal recovery based techniques over the DAS beamformer, the MUSIC method and the Capon technique in [95].

In regard to the OMP method we clearly see that the correlation between the columns of the matrix $\mathbf{\Phi}(\omega)$, given in (4.13), hinders this method from recovering all the reflectors.

As to the FOCUSS method for $p = 0.001$ as we mentioned before there is no guarantee for the FOCUSS technique to converge. In addition, as it is clear from Fig. 4.6 we have smaller RMSE for the proposed method compared to the FOCUSS method for $p = 0.001$. Furthermore, the intensity of the reconstructed reflectors in Fig. 4.4-(a) is higher than that of Fig. 4.4-(d).

Based on Fig. 4.6 the result of the ℓ_1-norm minimization based approach has higher RMSE than that of the proposed technique. Besides, in order for the result of the ℓ_1-norm minimization based method to be the sparsest solution, conditions $M^2 > (2L + 1)$ and $M^2 = O(L \text{ logN})$ should be satisfied. These conditions are extremely restrictive and hard to impose in practical situations [26–30]. On the other hand, for the proposed technique based on Algorithm 3 we do not need to impose any condition.

In the case of the FOCUSS algorithm for $p = 1$ which reduces to the MAP estimator using Laplacian prior, we see that the intensity of the reconstructed reflectors using the proposed method given in Fig. 4.4-(a) are higher compared to Fig. 4.5-(a). Moreover, like the ℓ_1-norm minimization based technique the result of the MAP estimator using Laplacian prior will not converge to the sparsest solution unless conditions $M^2 > (2L + 1)$ and $M^2 = O(L \text{ logN})$ are satisfied.

4.6 Conclusions

In this chapter, we developed a sparse signal representation based imaging algorithm which relies on Bayesian inference. We used an array of ultrasonic transducers to inspect the internal structure of a test sample immersed in water. We modeled the array spatial signature using Rayleigh-Sommerfeld diffraction formula. A Weibull distribution function was assigned to the reflectivity coefficients of the potential reflectors. We also developed a new method based on Mellin transform to estimate

the shape parameter of Weibull distribution function. To draw samples from the posterior function of the desired reflectivity coefficients we used the HMC technique. At the end, we used experimental data gathered from a solid test sample immersed in water to show the better performance of the proposed technique compared to the existing algorithms in the literature.

4.7 Appendix

4.7.1 Proof of Lemma 1

We estimate the parameter α for the Weibull distribution given in (4.24). The Mellin transform for a given function $f(t)$ is defined as [47]

$$\phi(\lambda) = \int_0^{+\infty} f(t) t^{\lambda-1} dt. \tag{4.64}$$

Moreover, the second-kind second-characteristic function is defined as [87]

$$\psi(\lambda) = \ln(\phi(\lambda)) \tag{4.65}$$

where $\ln(\cdot)$ stands for Napierian logarithm. Furthermore, the ν^{th}order second-kind cumulant, denoted as k_ν, can be obtained as [87]

$$\kappa_\nu = \left. \frac{d^\nu \psi(\lambda)}{d\lambda^\nu} \right|_{\lambda=1}. \tag{4.66}$$

Replacing $f(t)$ in (4.64) with $p(\mathbf{s}|\boldsymbol{\beta}, \alpha)$, we obtain

$$\phi(\lambda) = \int_0^{+\infty} \frac{\alpha}{\beta_i} s_i^{(\alpha-1)} e^{-\frac{s_i^\alpha}{\beta_i}} s_i^{\lambda-1} ds_i. \tag{4.67}$$

Defining $q \triangleq \frac{s_i^\alpha}{\beta_i}$, we can write (4.67) as

$$\phi(\lambda) = \beta_i^{\frac{\lambda-1}{\alpha}} \int_0^{+\infty} e^{-q} q^{\frac{\lambda-1}{\alpha}} dq. \tag{4.68}$$

Based on the definition of Gamma function, i.e., $\Gamma(\varsigma) = \int_0^{+\infty} \xi^{\varsigma-1} e^{-\xi} d\xi$, we can write (4.68) as

$$\phi(\lambda) = \beta_i^{\frac{\lambda-1}{\alpha}} \Gamma(\frac{\lambda-1}{\alpha} + 1). \tag{4.69}$$

Consequently, the second-kind second-characteristic function, defined in (4.65), is given as

$$\psi(\lambda) = \frac{\lambda-1}{\alpha} \ln(\beta_i) + \ln(\Gamma(\frac{\lambda-1}{\alpha} + 1)). \tag{4.70}$$

Using (4.66), the 1$^{\text{st}}$order and 2$^{\text{nd}}$order second-kind cumulants [87] for the i^{th} element of $\mathbf{s}$ are described as

$$\kappa_1 = \frac{d\psi(\lambda)}{d\lambda} \Big|_{\lambda=1} = \frac{1}{\alpha} \ln(\beta_i) + \frac{d}{d\lambda} \ln(\Gamma(\frac{\lambda-1}{\alpha} + 1)) \Big|_{\lambda=1} \tag{4.71}$$

$$\kappa_2 = \frac{d^2\psi(\lambda)}{d\lambda^2} \Big|_{\lambda=1} = \frac{d^2}{d\lambda^2} \ln(\Gamma(\frac{\lambda-1}{\alpha} + 1)) \Big|_{\lambda=1}. \tag{4.72}$$

In order to calculate $\frac{d}{d\lambda} \ln(\Gamma(\frac{\lambda-1}{\alpha} + 1)) \Big|_{\lambda=1}$, we use one of the useful definitions for Gamma function in differential form which is given as [96]

$$\Gamma(\xi + 1) = \lim_{n\to\infty} \frac{n!}{(\xi+1)(\xi+2)\cdots(\xi+n)} n^{\xi}. \tag{4.73}$$

Taking logarithm from both sides of (4.73) yields

$$\ln(\Gamma(\xi + 1)) = \lim_{n\to\infty} [\ln(n!) + \xi\ \ln(n) - \ln(\xi+1) - \ln(\xi+2) - \cdots - \ln(\xi+n)] \tag{4.74}$$

Then differentiating (4.74) with respect to ξ, yields

$$\frac{d \ln(\Gamma(\xi+1))}{d\xi} = \lim_{n\to\infty} \left(\ln(n) - \frac{1}{(\xi+1)} - \frac{1}{(\xi+2)} - \cdots - \frac{1}{(\xi+n)} \right). \tag{4.75}$$

We can rewrite (4.75) as

$$\frac{d \ln(\Gamma(\xi+1))}{d\xi} = \lim_{n\to\infty} \left(\ln(n) - \sum_{m=1}^{n} \frac{1}{(\xi+m)} \right). \tag{4.76}$$

We know that [96]

$$\lim_{n\to\infty}\left(\ln(n)-\sum_{m=1}^{n}\frac{1}{m}\right)=-\gamma \tag{4.77}$$

where $\gamma = 0.57721566940$ is Euler-Mascheroni constant [96]. Therefore, we can rewrite (4.76) as

$$\frac{d\ln(\Gamma(\xi+1))}{d\xi}=-\gamma+\sum_{m=1}^{\infty}\frac{\xi}{m(\xi+m)}. \tag{4.78}$$

Differentiating (4.78) with respect to ξ, we obtain that

$$\frac{d^2\ln(\Gamma(\xi+1))}{d\xi^2}=\sum_{m=1}^{\infty}\frac{1}{(\xi+m)^2}. \tag{4.79}$$

Then, using the definition given (4.71), the 2^{th}order second-kind cumulant is expressed as

$$\kappa_2=\frac{d^2}{d\lambda^2}\ln(\Gamma(\frac{\lambda-1}{\alpha}+1))\Big|_{\lambda=1}=\frac{1}{\alpha^2}\sum_{m=1}^{\infty}\frac{1}{m^2} \tag{4.80}$$

where we have used $\xi=\frac{\lambda-1}{\alpha}$ in (4.79), and consequently $\lambda=1$ corresponds to $\xi=0$. Furthermore, we have $\zeta(2)=\sum_{m=1}^{\infty}\frac{1}{m^2}=\frac{\pi^2}{6}$, where $\zeta(\cdot)$ is the Riemann zeta function [96], hence based on (4.80), the estimate of α is given as

$$\alpha=\sqrt{\frac{\pi^2}{6\kappa_2}} \tag{4.81}$$

where κ_2 is obtained as

$$\kappa_2=E(\ln(s_i)-E(\ln(s_i)))^2. \tag{4.82}$$

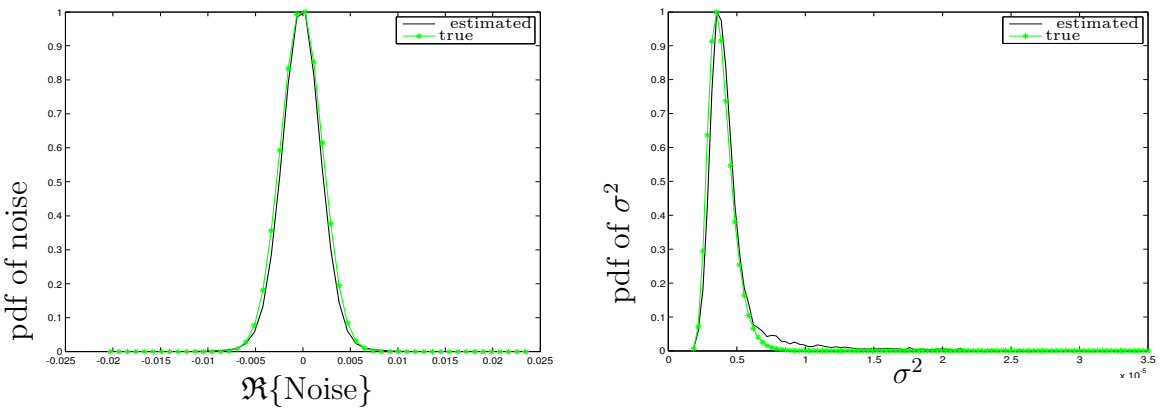

Figure 4.3: a) The estimated and the Gaussian pdf for the real part of the noise, b) the estimated and the inverse Gamma pdf for the noise variance.

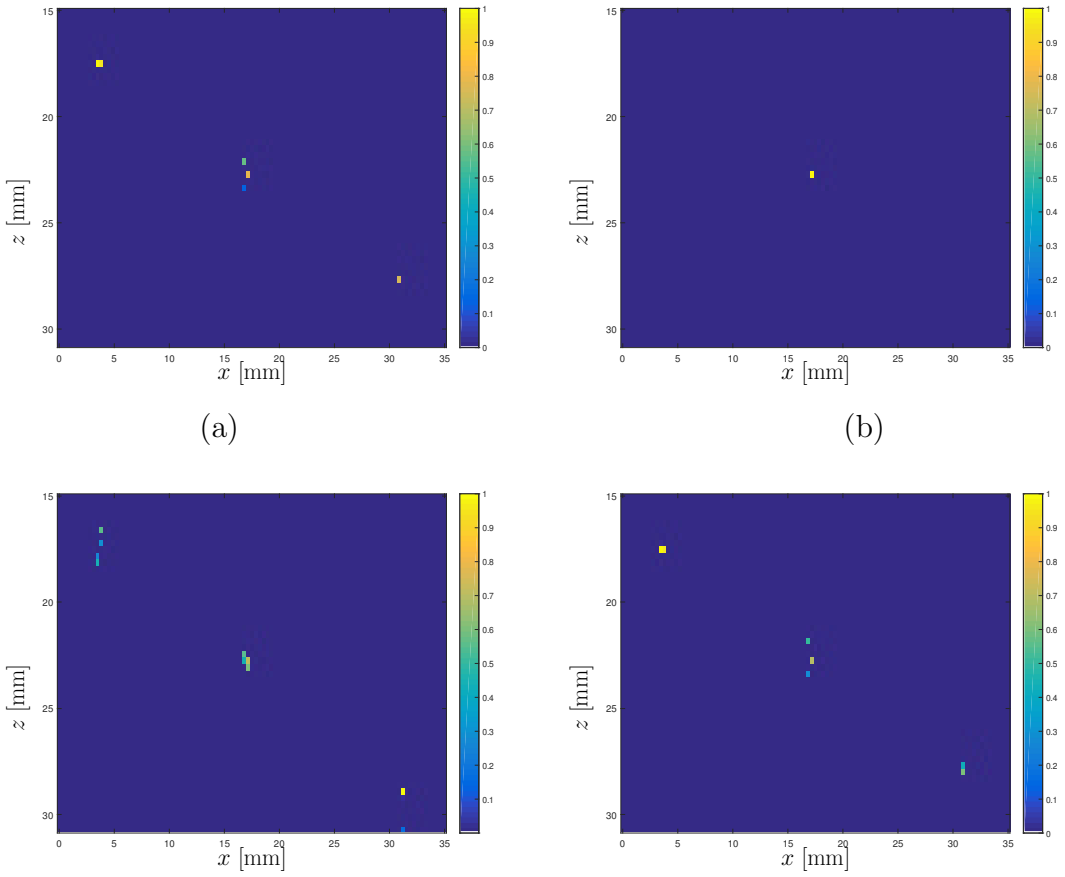

Figure 4.4: Normalized image in 2D for a) the proposed method based on Algorithm 3 at $f = 5$ MHz, b) the OMP based on (4.19) with $\xi_g = 10^{-4}$ at $f = 5$ MHz , c) the ℓ_1-norm minimization based approach using (4.18), d) the FOCUSS method based on Algorithm 2 at $f = 5$ MHz with $\epsilon_f = 10^{-4}$ and $p = 0.001$, $\lambda = 0.0014$, $N_f = 16$.

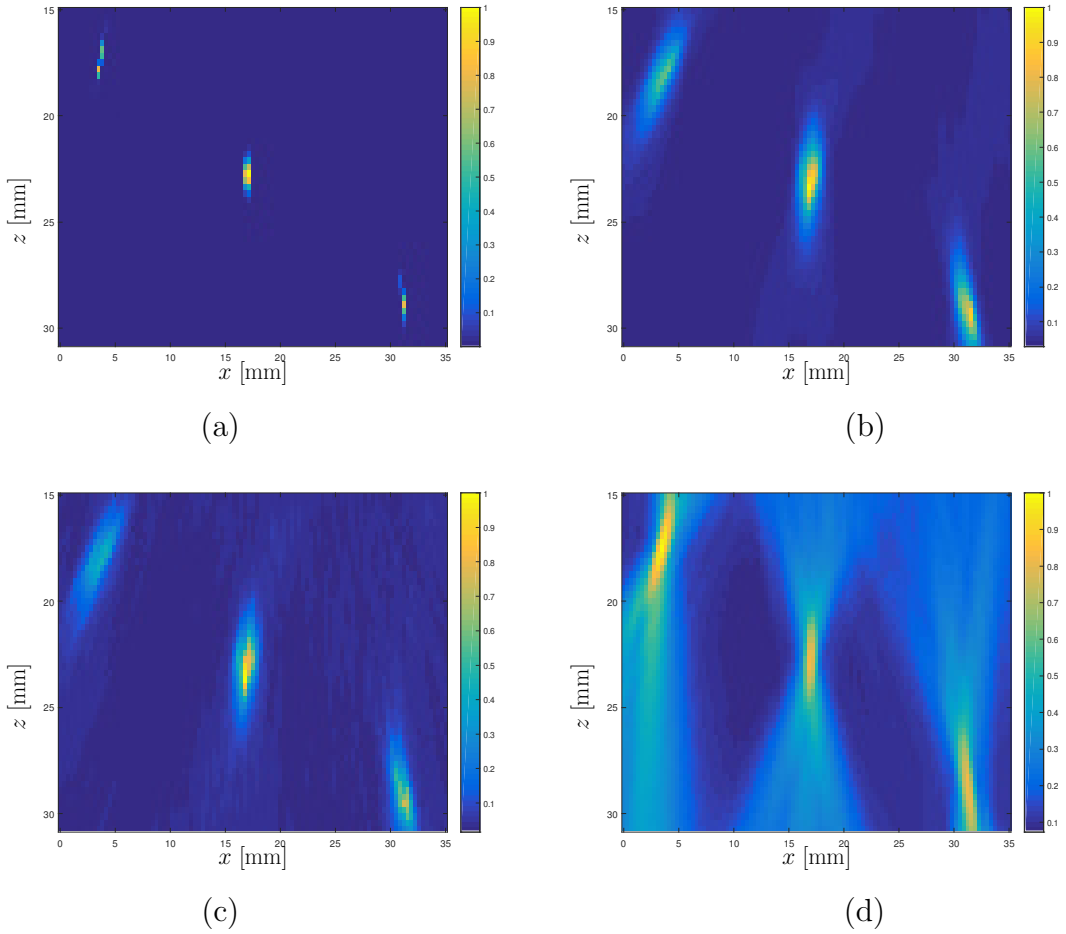

Figure 4.5: Normalized image in 2D for a) the FOCUSS method based on Algorithm 2 at $f = 5$ MHz with $\epsilon_f = 10^{-4}$ and $p = 1$, $\lambda = 5$, $N_f = 42$, b) the MUSIC based image using (4.16) with $L = 3$ and using the whole bandwidth from 2.5 MHz to 7.5 MHz, c) the Capon based image using (4.17) with $\kappa = 2000$ and using the whole bandwidth from 2.5 MHz to 7.5 MHz, d) the DAS based image using (4.15) and utilizing the whole bandwidth from 2.5 MHz to 7.5 MHz.

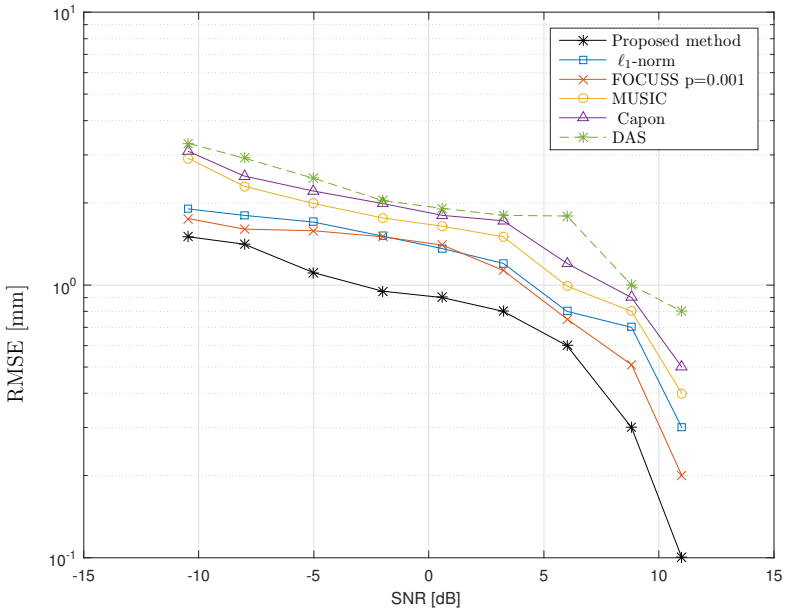

Figure 4.6: The RMSE vs SNR based on 50 Monte-Carlo runs.

Chapter 5

Conclusions and Future Work

5.1 Conclusions

In this study we addressed the problem of ultrasonic array imaging for both one and two layer scenarios.

In the case of one layer ultrasonic imaging, we used sparse signal representation based approach to develop several imaging techniques which take mode conversion into account. The proposed methods have higher resolution and lower sidelobe levels in comparison with the state-of-the-art techniques, such as MUSIC and Capon based methods. Our sparse signal representation based techniques are robust to correlated targets and they can generate a high resolution image using only one snapshot. Moreover, the sparse signal representation based techniques that we presented in this study, only utilize the energy of the probing signal corresponding to one frequency bin. We have shown the performance superiority of our sparse signal representation based methods over the existing methods using both simulated and experimental data.

We then developed a sparse signal representation based imaging algorithm which relies on Bayesian inference. A Weibull distribution function was assigned to the

reflectivity coefficients of the potential reflectors. We have shown that by taking the scale parameter of the Weibull distribution function as a hyper parameter, that has inverse Gamma distribution function, we can develop a sparse signal representation based method using Bayesian inference. Such a technique provide us with more flexibility and less restrictions compared to the previous sparse signal representation based methods. Not only using Bayesian philosophy for sparse signal reconstruction is a new subject which is almost a decade old, but also using Weibull distribution function to generate such a model is totally new and has been done for the first time in this dissertation.

We also developed a new method based on Mellin transform to estimate the shape parameter of Weibull distribution function. Regardless of shape parameter estimation, the technique that we have developed based on Mellin transform is new and very rich in nature. This a first time that the shape parameter of the Weibull distribution function is estimated using the Mellin transform.

The conditional posterior distribution function of the desired reflectivity coefficients that we calculated, turned out to be non-concave function. To maximize it we used the HMC technique. In fact instead of addressing the problem of finding the maximum of the conditional posterior distribution function, we changed the problem to sampling the conditional distribution function. At the end, we used the sample with the highest score as the MAP estimator. This way of finding the maximum of a given function can also be taken as a novel idea.

At the end, we used experimental data gathered from a solid test sample immersed in water to show the better performance of the proposed technique compared to the algorithms developed in the previous works.

5.2 Future Work

As a future work it might be a good idea and a novel technique to combine the Rayleigh-Sommerfeld diffraction formula with a sparse signal recovery based approach to reconstruct the image. Indeed, in the present work we treated the diffraction phenomenon and the sparse signal recovery based technique separately.

However, if we model the diffraction phenomenon as a random process and try to assign a distribution function to this random phenomenon, it is then possible to treat the over-determined matrix as a random matrix. Therefore, we can treat the over-determined matrix exactly as the other unknown random parameters such as the variance of the noise of the model.

Although the probing signal in all the experimental examples that we presented in this work was a wide-band signal, however, the proposed sparse signal recovery based techniques only utilized the energy of the signal corresponding to one frequency bin. Hence, as future work one can present a method that uses the energy of all the frequency bins in a unique way to obtain better performance.

In this study, the propagation velocity of the wave in both layers are taken as known parameters. However, one step toward future work can be the idea of taking the propagation velocity of the wave as unknown and develop an algorithm that can estimate these velocities within itself.

Moreover, the location of the surface of the test sample, i.e., the second layer, was assumed to be known in the present work. Although it is not hard to estimate the location of the surface of the test sample by looking at the strongest reflections that we obtain during data gathering but still it is a good idea to try to remove the dependency of the proposed method from the location of the surface.

Furthermore, in the realm of Bayesian philosophy developing a sparse signal representation based technique is not unique. One clue for the future work is to come

up with a different way of enforcing sparsity.

Bibliography

[1] N. Portzgen, D. Gisolf, and D. Verschuur, "Wave equation-based imaging of mode converted waves in ultrasonic NDI, with suppressed leakage from non-mode converted waves," *IEEE Transactions on Ultrasonics, Ferroelectrics, and Frequency Control*, vol. 55, pp. 1768–1780, August 2008.

[2] Wikipedia, "Nondestructive testing — wikipedia, the free encyclopedia," 2015, online; accessed 20-December-2015. [Online]. Available: \url{https://en.wikipedia.org/w/index.php?title=Nondestructive_testing\&oldid=695177939}

[3] *The e-Journal of Nondestructive Testing and Ultrasonics*, vol. 5, no. 9, September 2000.

[4] "ASNT nondestructive testing handbook: Ultrasonic testing," *American Society for Nondestructive Testing, American Society for Metals*, vol. 7, 1991.

[5] B. Drinkwater and P. Wilcox, "Ultrasonic arrays for non-destructive evaluation: A review," *NDT & E International*, vol. 39, no. 7, pp. 525–541, 2006.

[6] P. Wilcox, C. Holmes, and B. Drinkwater, "Advanced reflector characterization with ultrasonic phased arrays in NDE applications," *IEEE Trans. Ultrason., Ferroelectr., Freq. Control*, vol. 54, no. 8, pp. 1541 –1550, 2007.

[7] C. Holmes, B. W. Drinkwater, and P. D. Wilcox, "Post-processing of the full matrix of ultrasonic transmitreceive array data for non-destructive evaluation," *NDT & E International*, vol. 38, no. 8, pp. 701 – 711, 2005.

[8] S. Mahaut, O. Roy, C. Beroni, and B. Rotter, "Development of phased array techniques to improve characterization of defect located in a component of complex geometry." *Ultrasonics*, vol. 40, no. 1-8, pp. 165–169, 2002.

[9] P. D. Wilcox, "Omni-directional guided wave transducer arrays for the rapid inspection of large areas of plate structures." *IEEE Trans. Ultrason., Ferroelectr., Freq. Control*, vol. 50, no. 6, pp. 699–709, 2003.

[10] T. Stepinski and F. Lingvall, "Synthetic aperture focusing techniques for ultrasonic imaging of solid objects," *Proc. The 8th European Conference on Synthetic Aperture Radar (EUSAR)*, pp. 1– 4, Jun 2010.

[11] P. D. Wilcox, "Defect detection using ultrasonic arrays: The multi-mode total focusing method," *NDT & E International*, vol. 43, no. 2, pp. 123– 133, 2010.

[12] R. Levine and J. Michaels, "Block-sparse reconstruction and imaging for lamb wave structural health monitoring," *IEEE Transactions on Ultrasonics, Ferroelectrics, and Frequency Control*, vol. 61, pp. 1006–1015, June 2014.

[13] A. Golato, S. Santhanam, F. Ahmad, and M. G. Amin, "Multimodal sparse reconstruction in lamb wave-based structural health monitoring," *Proc. SPIE 9109, Compressive Sensing III, 91090P*, May 2014.

[14] R. M. Levine, J. E. Michaels, and S. J. Lee, "Guided wave localization of damage via sparse reconstruction," *AIP Conf. Proc*, vol. 1430, pp. 647–654, July 2011.

[15] M. H. Skjelvareid and Y. Birkelund, "Ultrasound imaging using multilayer synthetic aperture focusing," *Proceedings of the ASME*, vol. 5, no. PVP2010-25338, pp. 379–387, 2010.

[16] F. Foroozan and S. Shahbazpanahi, "MUSIC-based array imaging in multi-modal ultrasonic non-destructive testing," *Sensor Array and Multichannel Signal Processing Workshop (SAM), 2012 IEEE 7th*, pp. 529–532, 2012.

[17] R. Schmidt, "Multiple emitter location and signal parameter estimation," *IEEE Transactions on Antennas and Propagation*, vol. 34, no. 3, pp. 276–280, 1986.

[18] P. Stoica and N. Arye, "Music, maximum likelihood, and cramer-rao bound," *IEEE Transactions on Acoustics, Speech and Signal Processing*, vol. 37, no. 5, pp. 720–741, 1989.

[19] P. Stoica and R. L. Moses, *Spectral Analysis of Signals*. Upper Saddle River, NJ: Prentice-Hal, 2005.

[20] J. Capon, "High-resolution frequency-wavenumber spectrum analysis," *Proceedings of the IEEE*, vol. 57, no. 8, pp. 1408–1418, 1969.

[21] D. M. Malioutov, "A sparse signal reconstruciton perspective for source localization with sensor arrays," Ph.D. dissertation, Mass. Inst. Technol., Cambridge, MA, 2003.

[22] W. Schneider, "The common depth point stack," *Proceedings of the IEEE*, vol. 72, no. 10, pp. 1238–1254, 1984.

[23] N. Moallemi and S. ShahbazPanahi, "A new model for array spatial signature for two-layer imaging with applications to nondestructive testing using ultrasonic arrays," *IEEE Transactions on Signal Processing*, vol. 63, pp. 2464–2475, May 2015.

[24] M. Grant and S. Boyd, "CVX: Matlab software for disciplined convex programming, version 2.1," *http:// cvxr.com/ cvx*, Mar 2014.

[25] S. Boyd and L. Vandenberghe, *Convex Optimization*. Cambridge: Cambridge University Press, 2004.

[26] E. J. Candes, M. B. Wakin, and S. P. Boyd, "Enhancing sparsity by reweighted ℓ_1 minimization," *ArXiv e-prints*, Nov 2007.

[27] M. Elad and A. Bruckstein, "A generalized uncertainty principle and sparse representation in pairs of bases," *IEEE Transactions on Information Theory*, vol. 48, no. 9, pp. 2558–2567, Sep 2002.

[28] D. P. Wipf, "Bayesian methods for finding sparse representations," Ph.D. dissertation, UC San Diego, 2006.

[29] E. J. Candes, J. Romberg, and T. Tao, "Stable signal recovery from incomplete and inaccurate measurements," *Comm. Pure Appl. Math.*, vol. 59, Issue 8, pp. 1207–1223, August 2006.

[30] D. Donoho, "Compressed sensing," *IEEE Transactions on Information Theory*, vol. 52, pp. 1289–1306, April 2006.

[31] R. DeVore and V. Temlyakov, "Some remarks on greedy algorithms," *Advances in Computational Mathematics*, vol. 5, no. 1, pp. 173–187, 1996.

[32] C. Daniel and F. S. Wood, *Fitting Equations to Data: Computer Analysis of Multifactor Data*. John Wiley, 1999.

[33] S. Mallat and Z. Zhang, "Matching pursuits with time-frequency dictionaries," *IEEE Transactions on Signal Processing*, vol. 41, no. 12, pp. 3397–3415, Dec. 1993.

[34] T. T. Cai and L. Wang, "Orthogonal matching pursuit for sparse signal recovery with noise," *IEEE Transactions on Information Theory*, vol. 57, no. 7, July 2011.

[35] S. Babacan, R. Molina, and A. Katsaggelos, "Bayesian compressive sensing using Laplace priors," *IEEE Transactions on Image Processing*, vol. 19, no. 1, pp. 53–63, Jan 2010.

[36] D. J. MacKay, "Bayesian interpolation," *Neural Computation*, vol. 4, pp. 415–447, 1991.

[37] M. E. Tipping, "Sparse Bayesian learning and the relevance vector machine," *J. Mach. Learn. Res.*, vol. 1, pp. 211–244, Sep. 2001. [Online]. Available: http://dx.doi.org/10.1162/15324430152748236

[38] S. Ji, Y. Xue, and L. Carin, "Bayesian compressive sensing," *IEEE Transactions on Signal Processing*, vol. 56, no. 6, pp. 2346–2356, June 2008.

[39] J. Ziniel and P. Schniter, "Efficient high-dimensional inference in the multiple measurement vector problem," *CoRR*, vol. abs/1111.5272, 2011. [Online]. Available: http://arxiv.org/abs/1111.5272

[40] L. Yu, H. Sun, J. P. Barbot, and G. Zheng, "Bayesian compressive sensing for cluster structured sparse signals," *Signal Process.*, vol. 92, no. 1, pp. 259–269, Jan. 2012. [Online]. Available: http://dx.doi.org/10.1016/j.sigpro.2011.07.015

[41] S. S. Chen, D. L. Donoho, and M. A. Saunders, "Atomic decomposition by basis pursuit," *SIAM J. Scientific Computing*, vol. 20, no. 1, pp. 33–61, 1998.

[42] F. W. J., "Penalized regressions the bridge versus the lasso," *Journal of Computational and Graphical Statistics*, vol. 7, no. 3, pp. 397–416, 1998.

[43] J. O. Berger, *Statistical Decision Theory and Bayesian Analysis*. Springer, 1993.

[44] B. Amizic, S. Derin Babacan, R. Molina, and A. Katsaggelos, "Sparse Bayesian blind image deconvolution with parameter estimation," *Signal Processing Conference, 2010 18th European*, pp. 626–630, Aug 2010.

[45] N. Dobigeon, A. Hero, and J.-Y. Tourneret, "Hierarchical Bayesian sparse image reconstruction with application to MRFM," *IEEE Transactions on Image Processing*, vol. 18, no. 9, pp. 2059–2070, Sept 2009.

[46] Wikipedia, "Weibull distribution — wikipedia, the free encyclopedia," 2016, [Online; accessed 3-March-2016]. [Online]. Available: https://en.wikipedia.org/w/index.php?title=Weibull_distribution&oldid=702385937

[47] I. N. Sneddon, *Elements of Partial Differential Equations*. Dover Publications, 2006.

[48] D. Barber, *Bayesian Reasoning and Machine Learning*. Cambridge University Press, 2012.

[49] C. M. Bishop, *Pattern Recognition and Machine Learning (Information Science and Statistics)*. Secaucus, NJ, USA: Springer-Verlag New York, Inc., 2006.

[50] R. M. Neal, "MCMC using Hamiltonian dynamics," *Handbook of Markov Chain Monte Carlo*, vol. 54, pp. 113–162, 2010.

[51] P. Stoica, Z. Wang, and J. Li, "Robust Capon beamforming," *IEEE Signal Processing Letters*, vol. 10, no. 6, pp. 172 – 175, 2003.

[52] Z. Wang, J. Li, and R. Wu, "Time-delay- and time-reversal-based robust capon beamformers for ultrasound imaging," *IEEE Transactions on Medical Imaging*, vol. 24, pp. 1308 –1322, oct 2005.

[53] M. Cetin and W. Karl, "Feature-enhanced synthetic aperture radar image formation based on nonquadratic regularization," *IEEE Transactions on Image Processing*, vol. 10, no. 4, pp. 623–631, 2001.

[54] P. Charbonnier, L. Blanc-Feraud, G. Aubert, and M. Barlaud, "Deterministic edge-preserving regularization in computed imaging," *IEEE Transactions on Image Processing*, vol. 6, no. 2, pp. 298–311, 1997.

[55] B. Jeffs, "Sparse inverse solution methods for signal and image processing applications," *IEEE International Conference on Acoustics, Speech and Signal Processing*, vol. 3, pp. 1885–1888 vol.3, 1998.

[56] J.-J. Fuchs, "Linear programming in spectral estimation. application to array processing," *IEEE International Conference on Acoustics, Speech, and Signal Processing, ICASSP-96*, vol. 6, pp. 3161–3164 vol. 6, 1996.

[57] D. Malioutov, M. Cetin, and A. Willsky, "A sparse signal reconstruction perspective for source localization with sensor arrays," *IEEE Transactions on Signal Processing*, vol. 53, no. 8, pp. 3010–3022, 2005.

[58] N. Wagner, Y. Eldar, and Z. Friedman, "Compressed beamforming in ultrasound imaging," *IEEE Transactions on Signal Processing*, vol. 60, no. 9, pp. 4643–4657, Sept 2012.

[59] X. Xu, X. Wei, and Z. Ye, "DOA estimation based on sparse signal recovery utilizing weighted l_1 -norm penalty," *IEEE Signal Processing Letters*, vol. 19, no. 3, pp. 155–158, March 2012.

[60] M. Hyder and K. Mahata, "Direction-of-arrival estimation using a mixed $\ell_{2,0}$ norm approximation," *IEEE Transactions on Signal Processing*, vol. 58, no. 9, pp. 4646–4655, Sept 2010.

[61] S. Cotter, B. Rao, K. Engan, and K. Kreutz-Delgado, "Sparse solutions to linear inverse problems with multiple measurement vectors," *IEEE Transactions on Signal Processing*, vol. 53, no. 7, pp. 2477–2488, July 2005.

[62] Y. Eldar and M. Mishali, "Robust recovery of signals from a structured union of subspaces," *IEEE Transactions on Information Theory*, vol. 55, no. 11, pp. 5302–5316, Nov 2009.

[63] N. Zhao, A. Basarab, D. Kouame, and J. Tourneret, "Joint segmentation and deconvolution of ultrasound images using a hierarchical Bayesian model based on generalized Gaussian priors," *CoRR*, vol. abs/1412.2813, 2014. [Online]. Available: http://arxiv.org/abs/1412.2813

[64] N. Dobigeon, A. Basarab, D. Kouame, and J.-Y. Tourneret, "Regularized Bayesian compressed sensing in ultrasound imaging," *Signal Processing Conference (EUSIPCO), 2012 Proceedings of the 20th European*, pp. 2600–2604, Aug 2012.

[65] J. Zhang, B. W. Drinkwater, and P. D. Wilcox, "The use of scattering matrix to model multi-modal array inspection with the TFM," *AIP Conference Proceedings*, vol. 1096, no. 1, pp. 888–895, 2009.

[66] M. Engholm and T. Stepinski, "Adaptive beamforming for array imaging of plate structures using lamb waves," *IEEE Transactions on Ultrason., Ferroelectr., Freq. Control*, vol. 57, no. 12, pp. 2712 –2724, 2010.

[67] H. Cox, R. Zeskind, and M. Owen, "Robust adaptive beamforming," *IEEE Transactions on Acoustics, Speech, and Signal Processing*, vol. 35, pp. 1365 – 1376, Oct. 1987.

[68] B. Carlson, "Covariance matrix estimation errors and diagonal loading in adaptive arrays," *IEEE Transactions on Aerospace and Electronic Systems*, vol. 24, no. 4, pp. 397–401, Jul 1988.

[69] S. Vorobyov, A. Gershman, and Z.-Q. Luo, "Robust adaptive beamforming using worst-case performance optimization: a solution to the signal mismatch problem," *IEEE Transactions on Signal Processing.*, vol. 51, pp. 313 – 324, Feb 2003.

[70] S. ShahbazPanahi, A. Gershman, Z.-Q. Luo, and K. M. Wong, "Robust adaptive beamforming for general-rank signal models," *IEEE Transactions on Signal Processing*, vol. 51, no. 9, pp. 2257–2269, Sept 2003.

[71] J. Li and P. Stoica, Eds., *Robust Adaptive Beamforming*. Wiley-Interscience, 2006.

[72] H. L. van Trees, *Optimum array processing*, ser. Detection, estimation and modulation theory. Wiley-Interscience, 2002, vol. 4.

[73] R. Coifman, Y. Meyer, S. Quake, and M. Wickerhauser, "Signal processing and compression with wavelet packets," *Wavelets and Their Applications*, vol. 442, pp. 363–379, 1994.

[74] R. Coifman and M. Wickerhauser, "Entropy-based algorithms for best basis selection," *IEEE Transactions on Information Theory*, vol. 38, no. 2, pp. 713–718, March 1992.

[75] D. Donoho and X. Huo, "Uncertainty principles and ideal atomic decomposition," *IEEE Transactions on Information Theory*, vol. 47, no. 7, pp. 2845–2862, Nov 2001.

[76] D. L. Donoho and M. Elad, "Optimally sparse representation in general (non-orthogonal) dictionaries via minimization," *PROC. NATL ACAD. SCI. USA 100 2197202*, 2002.

[77] D. L. Donoho, "For most large underdetermined systems of linear equations the minimal ℓ_1-norm solution is also the sparsest solution," *Comm. Pure Appl. Math*, p. 797829, 2006.

[78] D. L. Donoho and J. Tanner, "Neighborliness of randomly-projected simplices in high dimensions," *Proc. Natl. Acad. Sci. USA*, pp. 9452–9457, 2005.

[79] S. Foucart and H. Rauhut, *A Mathematical Introduction to Compressive Sensing*. Birkhuser, 2013.

[80] J. Tropp and A. Gilbert, "Signal recovery from random measurements via orthogonal matching pursuit," *IEEE Transactions on Information Theory*, vol. 53, no. 12, pp. 4655–4666, Dec 2007.

[81] Y. C. Pati, R. Rezaiifar, Y. C. P. R. Rezaiifar, and P. S. Krishnaprasad, "Orthogonal matching pursuit: Recursive function approximation with applications to wavelet decomposition," *Proceedings of the 27 th Annual Asilomar Conference on Signals, Systems, and Computers*, pp. 40–44, 1993.

[82] W. Dai and O. Milenkovic, "Subspace pursuit for compressive sensing signal reconstruction," *IEEE Transactions on Information Theory*, vol. 55, no. 5, pp. 2230–2249, May 2009.

[83] S. Qaisar, R. Bilal, W. Iqbal, M. Naureen, and S. Lee, "Compressive sensing: From theory to applications, a survey," *Communications and Networks, Journal of*, vol. 15, no. 5, pp. 443–456, Oct 2013.

[84] T. Eltoft, T. Kim, and T.-W. Lee, "On the multivariate Laplace distribution," *Signal Processing Letters, IEEE*, vol. 13, no. 5, pp. 300–303, May 2006.

[85] H. Jeffreys, *Theory of Probability*. Oxford University Press., 1939.

[86] A. Lee, F. Caron, A. Doucet, and C. Holmes, "A hierarchical Bayesian framework for constructing sparsity-inducing priors," *arXiv:1009.1914v2*, Sep 2010.

[87] A. Papoulis, *Probability, Random Variables and Stochastic Processes*. McGraw-Hill, 2002.

[88] C. Holmes, B. W. Drinkwater, and P. D. Wilcox, "Post-processing of the full matrix of ultrasonic transmit-receive array data for non-destructive evaluation," *Nondestr. Test Eval. Int.*, vol. 38, pp. 701 – 711, Dec. 2005.

[89] P. Wilcox, C. Holmes, and B. Drinkwater, "Advanced reflector characterization with ultrasonic phased arrays in NDE applications," *IEEE Trans. Ultrasonics, Ferroelectrics., and Freq. Contr.*, vol. 54, pp. 1541–1550, Aug. 2007.

[90] E. Candes, J. Romberg, and T. Tao, "Robust uncertainty principles: exact signal reconstruction from highly incomplete frequency information," *IEEE Transactions on Information Theory*, vol. 52, no. 2, pp. 489–509, Feb 2006.

[91] V. Cevher, M. F. Duarte, and R. G. Baraniuk, "Distributed target localization via spatial sparsity," *in Porc. The 16th EuropeanSignal Processing Conference*, pp. 25–29, Aug 2008.

[92] V. Cevher, P. Boufounos, R. Baraniuk, A. Gilbert, and M. Strauss, "Near-optimal Bayesian localization via incoherence and sparsity," *Information Processing in Sensor Networks, 2009. IPSN 2009. International Conference on*, pp. 205–216, April 2009.

[93] Y. Eldar, P. Kuppinger, and H. Bolcskei, "Block-sparse signals: Uncertainty relations and efficient recovery," *IEEE Transactions on Signal Processing*, vol. 58, no. 6, pp. 3042–3054, June 2010.

[94] J. W. Goodman, *Introduction to Fourier Optics*. McGraw-Hill, 1996.

[95] S. Hamidi and S. ShahbazPanahi, "Sparse signal recovery based imaging in the presence of mode conversion with application to non-destructive testing," *IEEE Transactions on Signal Processing*, vol. 64, no. 5, pp. 1352–1364, March 2016.

[96] G. B. Arfken and H. J. Weber, *Mathematical Methods for Physicists*. Academic Press, 2012.